

AD A119422

AFRPL-TR-82-051



AN INVESTIGATION OF EXPERIMENTAL TECHNIQUES  
FOR OBTAINING PARTICULATE BEHAVIOR IN  
METALLIZED SOLID PROPELLANT COMBUSTION

Authors: S. G. Karagounis V. D. Diloreto  
T. R. Gillespie II E. Dubrov  
P. J. Hickey D. W. Netzer

DEPARTMENT OF AERONAUTICS  
NAVAL POSTGRADUATE SCHOOL  
MONTEREY, CALIFORNIA 93940

JULY 1982

Final Report for the period February 1980 through December 1981

APPROVED FOR PUBLIC RELEASE; DISTRIBUTION UNLIMITED

The AFRPL Technical Services Office has reviewed this report,  
and it is releasable to the National Technical Information  
Service, where it will be available to the general public,  
including foreign nationals.

DTIC FILE COPY

Prepared for  
AIR FORCE ROCKET PROPULSION LABORATORY  
DIRECTOR OF SCIENCE AND TECHNOLOGY  
AIR FORCE SYSTEMS COMMAND  
EDWARDS AFB, CALIFORNIA 93523

DTIC  
SELECTED  
SEP 21 1982

82 09 20 162 A

## NOTICE

Publication of this report does not constitute approval or disapproval of the ideas or findings. It is published in the interest of scientific and technical information exchange.

## FOREWORD

This report was submitted by the Department of Aeronautics, Naval Post-graduate School, Monterey, California, 93940, under MIPR Numbers FO4611 - 80 - X - 0032, FO4611 - 81 - X - 0003, FO4611 - 81 - X - 0066, and FO4611 - 81 - X - 0008 with the Air Force Rocket Propulsion Laboratory, Edwards AFB, California 93523.

This report summarizes the development and initial applications of high speed motion pictures, electron microscopy of post-fire residues, measurements of scattered laser power spectra and optical holography to obtain data on the effects of propellant properties and motor operating conditions on the behavior of metallized particulates within the grain port and nozzle of solid propellant rocket motors.

This technical report is approved for release and distribution in accordance with the distribution statement on the cover and on the DD Form 1473.

  
\_\_\_\_\_  
KEVIN K. NACK, 1LT, USAF  
PROJECT MANAGER

  
\_\_\_\_\_  
WAYNE E. ROE  
CHIEF, COMBUSTION TECH. BRANCH

FOR THE DIRECTOR

  
\_\_\_\_\_  
EDWARD E. STEIN  
DEPUTY CHIEF, PROPULSION ANALYSIS DIVISION

UNCLASSIFIED

SECURITY CLASSIFICATION OF THIS PAGE (When Data Entered)

REPORT DOCUMENTATION PAGE		READ INSTRUCTIONS BEFORE COMPLETING FORM
1. REPORT NUMBER AFRPL-TR-82- 51	2. GOVT ACCESSION NO. AD-A19422	3. RECIPIENT'S CATALOG NUMBER
4. TITLE (and Subtitle) AN INVESTIGATION OF EXPERIMENTAL TECHNIQUES FOR OBTAINING PARTICULATE BEHAVIOR IN METALLIZED SOLID PROPELLANT COMBUSTION		5. TYPE OF REPORT & PERIOD COVERED FINAL Feb 1980 - Dec 1981
		6. PERFORMING ORG. REPORT NUMBER
7. AUTHOR(s) S. G. Karagounis, V. D. Diloreto, T. R. Gillespie II, E. Dubrov, P. J. Hickey, D. W. Netzer		8. CONTRACT OR GRANT NUMBER(s) F04611-80-X-0032, F04611-82- F04611-81-X-0003, X-0008 F04611-81-X-0066
9. PERFORMING ORGANIZATION NAME AND ADDRESS Department of Aeronautics Naval Postgraduate School Monterey, California 93940		10. PROGRAM ELEMENT, PROJECT, TASK AREA & WORK UNIT NUMBERS
11. CONTROLLING OFFICE NAME AND ADDRESS Air Force Rocket Propulsion Laboratory/DYC Edwards AFB, California 93523		12. REPORT DATE JULY 1982
		13. NUMBER OF PAGES 151
14. MONITORING AGENCY NAME & ADDRESS (if different from Controlling Office)		15. SECURITY CLASS. (of this report) UNCLASSIFIED
		15a. DECLASSIFICATION/DOWNGRADING SCHEDULE
16. DISTRIBUTION STATEMENT (of this Report) APPROVED FOR PUBLIC RELEASE; DISTRIBUTION UNLIMITED		
17. DISTRIBUTION STATEMENT (of the abstract entered in Block 20, if different from Report) APPROVED FOR PUBLIC RELEASE; DISTRIBUTION UNLIMITED		
18. SUPPLEMENTARY NOTES		
19. KEY WORDS (Continue on reverse side if necessary and identify by block number) Solid Propellants Particulates Optical Methods		
20. ABSTRACT (Continue on reverse side if necessary and identify by block number) The goal of this initial investigation was to develop and compare experimental techniques that could be used for obtaining quantitative data on the effects of propellant properties, operating pressure and nozzle geometry on the behavior of metallized particulates within the grain port and nozzle of solid propellant rocket motors. The techniques employed were high speed motion pictures of strand burners and slab burners in a cross-flow environment, SEM analysis of post-fire residue (strand, slab, and motor), determination of $D_{32}$ at the exit of an exhaust nozzle using measurements of scattered laser power spectra, and holo-		

DD FORM 1 JAN 73 1473

EDITION OF 1 NOV 65 IS OBSOLETE  
S/N 0102-014-6601

UNCLASSIFIED  
SECURITY CLASSIFICATION OF THIS PAGE (When Data Entered)

CONFIDENTIAL

Cont II

Micrometer

UNCLASSIFIED

SECURITY CLASSIFICATION OF THIS PAGE (When Data Entered)

28. Abstract - grams of burning propellant strands and slabs in a cross-flow environment. All techniques were successfully developed and employed to obtain particulate size data from a series of specially formulated propellants. The motion picture and holographic techniques were successfully demonstrated for operating pressures of 34 and 68 atm. and with up to 15% aluminum. Shortness in resolution was obtained in the high speed motion pictures with a 1.12X magnification (and very small depth of field) and eleven in resolution was obtained in the holograms. Measurements of  $D_p$  at the nozzle exit plane of a small end-burning motor were in close agreement with size analysis of collected exhaust particulates.

Approved for	<input checked="" type="checkbox"/>
Special	<input type="checkbox"/>
Available to	
Dist	Special

DTIC  
COPY  
INSPECTED

UNCLASSIFIED

SECURITY CLASSIFICATION OF THIS PAGE (When Data Entered)

## TABLE OF CONTENTS

Abstract-----	1
List of Tables-----	11
List of Figures-----	111
I. INTRODUCTION -----	1
II. METHOD OF INVESTIGATION -----	7
III. EXPERIMENTAL APPARATUS AND PROCEDURES -----	8
A. COMBUSTION BOMB -----	8
1. Apparatus -----	8
2. Procedures and System Calibration -----	9
B. DIFFRACTIVELY SCATTERED LIGHT MEASUREMENTS -----	12
1. Background -----	12
2. Apparatus -----	13
3. Experimental Procedures and System Calibration -----	13
C. MOTION PICTURE AND HOLOGRAPHIC MEASUREMENTS IN TWO-DIMENSIONAL MOTOR -----	18
1. Background -----	18
2. Two-dimensional Slab Motor -----	18
3. Pulsed Ruby Laser -----	19
4. Holocamera -----	20
5. Reconstruction Apparatus -----	21
6. Motion Pictures -----	22
7. Experimental Procedures -----	22
IV. RESULTS AND DISCUSSION -----	27
A. COMBUSTION BOMB INVESTIGATION - MOTION PICTURES AND PARTICLE COLLECTION -----	27
1. Postfire Particle Size Analysis -----	27
2. High Speed Motion Picture Analysis -----	29
3. Summary of Results -----	32

B. DIFFRACTIVELY SCATTERED LIGHT MEASUREMENTS	34
C. HOLOGRAPHIC INVESTIGATION	36
1. Strand Burners	36
2. 2-D Slab Motor	37
V. CONCLUSIONS	39
REFERENCES	41

## ABSTRACT

The goal of this initial investigation was to develop and compare experimental techniques that could be used for obtaining quantitative data on the effects of propellant properties, operating pressure and nozzle geometry on the behavior of metallized particulates within the grain port and nozzle of solid propellant rocket motors. The techniques employed were high speed motion pictures of strand burners and slab burners in a cross-flow environment, SEM analysis of post-fire residue (strand, slab, and motor), determination of  $D_{32}$  at the exit of an exhaust nozzle using measurements of scattered laser power spectra, and holograms of burning propellant strands and slabs in a cross-flow environment.

All techniques were successfully developed and employed to obtain particulate size data from a series of specially formulated propellants.

The motion picture and holographic techniques were successfully demonstrated for operating pressures of 34 and 68 atm. and with up to 15% aluminum. Fourteen  $\mu\text{m}$  resolution was obtained in the high speed motion pictures with a 1.12X magnification (and very small depth of field) and eleven  $\mu\text{m}$  resolution was obtained in the holograms.

Measurements of  $D_{32}$  at the nozzle exit plane of a small end-burning motor were in close agreement with size analysis of collected exhaust particulates.

LIST OF TABLES

Table	Page
I. Propellant Compositions -----	45
II. Particle Collection Test Conditions -----	46
III. High Speed Motion Picture Test Conditions -----	47
IV. Resolution Target Test Conditions -----	49
V. Burning Rate Exponents -----	50
VI. Volume-Surface Mean Diameter ( $D_{32}$ ) Measurement Results -----	51

## LIST OF FIGURES

Figure	Page
1. Schematic of Combustion Bomb -----	52
2. Schematic of Combustion Bomb Modification -----	53
3. Schematic of Experimental Apparatus-Combustion Bomb -----	54
4. Photograph of Experimental Apparatus-Combustion Bomb -----	55
5. Propellant Strand Dimensions -----	56
6. Photographs of 1951 USAF Resolution Target	
(a) Initial Study, (b) Modified combustion bomb -----	57
7. Schematic Diagram of Diffractively Scattered Light Apparatus -----	58
8. Nondimensionalized Illumination Profiles [ $I(\theta)$ versus $\bar{\theta}$ ] -----	59
9. Photodiode Output Voltage versus Distance from Centerline for Glass Beads -----	60
10. Light Scattering Geometry -----	61
11. Photodiode Output Voltage versus Distance from Centerline for $Al_2O_3$ Particles -----	62
12. Motor Line Drawing, Side View -----	63
13. Motor Line Drawing, Window Side View -----	64
14. Plexiglas Spacer Arrangement -----	65
15. High Speed Motion Picture Apparatus -----	66
16. Photograph of 2-D Motor with Control Box and Holocamera -----	67
17. Photograph of 2-D Motor Components -----	67
18. Photographs of RPL Ruby Laser Components -----	68
19. Lens Assisted Holographic System -----	69
20. Holographic Reconstruction Apparatus -----	70
21. Hologram of 1951 USAF Resolution Target -----	71
22. Photograph of Reconstructed Hologram of 0-80 Screw Used for Particle Sizing -----	72

23. Photomicrographs of Postfire Residue	
(1445240480, WGS-5A, $P_c = 34$ atm)	73
24. Photomicrographs of Postfire Residue	
(1445180480, WGS-5A, $P_c = 68$ atm)	76
25. Photomicrographs of Postfire Residue	
(1030030580, WGS-6A, $P_c = 34$ atm)	79
26. Photomicrographs of Postfire Residue	
(1600170480, WGS-6A, $P_c = 68$ atm)	82
27. Photomicrographs of Postfire Residue	
(1215030580, WGS-7A, $P_c = 34$ atm)	85
28. Photomicrographs of Postfire Residue	
(1400240480, WGS-7A, $P_c = 68$ atm)	88
29. Photomicrographs of Postfire Residue	
(1100030580, WGS-7, $P_c = 34$ atm)	91
30. Photomicrographs of Postfire Residue	
(1500210480, WGS-7, $P_c = 68$ atm)	94
31. Photomicrographs of Postfire Residue	
(1230110580, NWC-1, $P_c = 34$ atm)	97
32. Photomicrographs of Postfire Residue	
(1500100580, NWC-1, $P_c = 68$ atm)	100
33. Photomicrographs of Postfire Residue	
(1200110580, NWC-2, $P_c = 34$ atm)	103
34. Photomicrographs of Postfire Residue	
(1615100580, NWC-2, $P_c = 68$ atm)	106
35. Particle Size Distribution	
(1445240480, WBS-5A, $P_c = 34$ atm)	109

36. Particle Size Distribution		
(1445180480, WGS-5A, $P_c = 68$ atm)	-----	109
37. Particle Size Distribution		
(1030030580, WGS-6A, $P_c = 34$ atm)	-----	110
38. Particle Size Distribution		
(1600170480, WGS-6A, $P_c = 68$ atm)	-----	110
39. Particle Size Distribution		
(1215030580, WGS-7A, $P_c = 34$ atm)	-----	111
40. Particle Size Distribution		
(1400240480, WGS-7A, $P_c = 68$ atm)	-----	111
41. Particle Size Distribution		
(1100030580, WGS-7, $P_c = 34$ atm)	-----	112
42. Particle Size Distribution		
(1500210480, WGS-7, $P_c = 68$ atm)	-----	112
43. Particle Size Distribution		
(1230110580, NWC-1, $P_c = 34$ atm)	-----	113
44. Particle Size Distribution		
(1500100580, NWC-1, $P_c = 68$ atm)	-----	113
45. Particle Size Distribution		
(1200110580, NWC-2, $P_c = 34$ atm)	-----	114
46. Particle Size Distribution		
(1615100580, NWC-2, $P_c = 68$ atm)	-----	114
47. Comparison of 40 and 220 Particle Sample		
Distributions (14452400480, WGS-5A, $P_c = 34$ atm)	-----	115
48. Comparison of 40 and 220 Particle Sample		
Distributions (1030030580, WGS-6A, $P_c = 34$ atm)	-----	116
49. Initial Aluminum Particle Diameter Versus Mean Postfire		
Particle Diameter	-----	117

50. High Speed Motion Picture Frame (1415250580, WGS-5A, 34 atm) -----	118
51. High Speed Motion Picture Frame (1100250580, WGS-5A, 68 atm) -----	118
52. Burning Particle Diameter Versus Initial Aluminum Particle Diameter -----	119
53. Burning Particle Diameter Versus Mean Postfire Particle Diameter -----	120
54. Postfire Particle Size Distribution, WGS-6A Propellant -----	121
55. Burning Particle Average Velocity Versus Burning Particle Diameter for Propellant WGS-5A -----	122
56. Burning Particle Average Velocity Versus Burning Particle Diameter for Propellant WGS-6A -----	122
57. Burning Particle Average Velocity Versus Burning Particle Diameter for Propellant WGS-7A -----	123
58. Burning Rate Versus Initial Aluminum Diameter -----	124
59. Photodiode Output-Voltage Profiles Versus Distance from Optical Centerline (actual runs) -----	125
60. SEM Photomicrographs of Rocket Exhaust Particles (clean) -----	126
61. SEM Photomicrographs of Rocket Exhaust Particles (as-collected) -----	127
62. Size Distribution of Clean Exhaust Particles from Propellant NWC-1, Burned at 13 atm -----	128
63. Size Distribution of (As-Collected) Exhaust Particles from Propellant NWC-1, Burned at 13 atm -----	129
64. WGS-5A Propellant Burned at 34 atm -----	130
65. WGS-5A Propellant Burned at 68 atm -----	131
66. WGS-6A Propellant Burned at 34 atm -----	132
67. WGS-6A Propellant Burned at 68 atm -----	133

68.	WGS-7A Propellant Burned at 34 atm -----	134
69.	WGS-7A Propellant Burned at 68 atm -----	135
70.	N-7 Propellant Holograms 50 $\mu$ sec Pulse -----	136
71.	WGS-7 Propellant Burned at 68 atm -----	137
72.	Photograph of Reconstructed Hologram, WGS-6A Propellant in 2-D Slab Motor -----	138
73.	Motion Pucture Frame of WGS-7A Propellant in 2-D Slab Motor -----	139

## I. INTRODUCTION

For many years solid propellants have been employed for missile propulsion. Practically all tactical and many strategic missiles use solid propellants. Historically, there have been two primary types of solid rocket propellants; composite and double-base (or homogeneous). Composite propellants normally consist of a mechanical mixture of oxidizer particles (ammonium perchlorate (AP), etc.) imbedded in a fuel/binder (polybutadiene-acrylic-acid (PBAA), PBAN, CTPB, etc.). Double-base propellants normally consist of mixtures of monopropellant molecules, i.e., nitrocellulose and nitroglycerine. They are "mixed" on the molecular scale. In recent years composite-modified double-base (CMDB) propellants have been developed also.

Many solid propellants also contain metal additives in quantities up to 25% by weight. These metal fuels increase the energy content and also provide an acoustic damping mechanism for combustion pressure oscillations within the propellant port. The most common metal additive is aluminum, in a fine powder form. The metal particles are mixed in the propellant before curing. When these small (1 - 50  $\mu\text{m}$ ) particles reach the burning surface, various phenomena have been observed to occur for strands burned under conditions of zero cross-flow velocity<sup>1,2,3</sup>. Some particles immediately leave the surface while others agglomerate on the surface before leaving. Post-fire particle diameters have been observed smaller than 0.10  $\mu\text{m}$  whereas particles within the port of burning propellant grains have been recorded with diameters greater than 1200  $\mu\text{m}$ . The behavior of the metal particles is a function of propellant composition, operating environment (pressure, etc.) and the nozzle design and throat size. The particles often burn slowly within the fuel port when compared to mean gas transient times. If these particles are not consumed before leaving the nozzle, low combustion efficiency and delivered

specific impulse results<sup>4,5,6,7,8</sup>. The two-phase flow losses which result from the thermal and velocity lag of the particles can result in large losses in delivered impulse (2 - 10%)<sup>7</sup>. In addition, unburned aluminum can also cause performance losses (1% Isp loss/10% unburned Al<sup>7</sup>). Apparently, the high shear forces in the nozzle created by the particles lagging the high velocity gas flow cause the larger particles to break up into smaller particles. This behavior is known to occur for liquid droplets and is correlated through the dimensionless parameter, Weber number. The Weber number is the ratio of inertial to surface tension forces. Minimization of these two-phase flow losses is required if theoretically high performing solid propellants are to produce high delivered performance. This minimization of losses must be achieved while meeting the requirements for particle damping.

Current performance prediction methods<sup>9,10</sup> as well as steady and unsteady burning rate models are hindered from a lack of adequate experimental (qualitative and quantitative) data. For better models to be developed, detailed particle generation, burning, and breakup data are required as a function propellant composition, operating environment and design configuration.

To obtain a better understanding of the effects of design variables and propellant properties on two-phase flow losses requires a careful study of the particle behavior within the reacting flow environment. Strand data can yield valuable data, but data are badly needed from tests which more realistically match the motor environment. Several options are available. Simple exhaust opacity measurements coupled with performance measurements (thrust, C\*) can yield qualitative behavior. More refined optical techniques based upon the mechanisms of Mie scattering theory can be used for obtaining mean particle sizes and concentrations<sup>11-15</sup>. These data can be used to relate smoke and plume characteristics to motor operating conditions and propellant

properties. Analysis of particle sizes in grain residues and/or collected exhaust<sup>3</sup> can provide quantitative data. However, the use of quenching and out-of-motor residue analysis must be made with caution since the data may not realistically reproduce in-motor characteristics. High speed photography can also provide valuable data. High quality motion pictures have been obtained without cross-flow velocities in both standard gravity<sup>1-3</sup> and acceleration environments<sup>16,17</sup>. Caveny, et al<sup>18,19</sup> have obtained motion pictures of aluminized solid propellants burning in a more realistic cross-flow environment. They employed a two-dimensional, windowed rocket motor with an aluminized propellant sandwiched between non-aluminized propellant to limit the number density of particles. Their studies have shown the importance of cross-flow velocity within the propellant port, agglomerate breakup, and the effect that nozzle contour may have on the latter.

Another possible technique for studying two-phase flow losses is holography. Briones and Wuerker<sup>20,21</sup> have applied this technique to the combustion of solid propellant strands in zero-crossflow environments. Their work has demonstrated the ability to obtain three-dimensional information with resolution down to approximately 2-10  $\mu\text{m}$ . Short laser pulse widths (<10 nanoseconds) and lens assisted holograms were necessary in order to obtain these holographic capabilities.

Coupling of the experimental techniques of Caveny, et al<sup>18,19</sup> with the holographic techniques of Briones and Wuerker<sup>20,21</sup> should provide an excellent experimental technique for obtaining an increased understanding of the effects of propellant properties, operating environment, and hardware design on particle behavior and combustion zone characteristics within solid rocket motors.

The overall goal of this investigation is to obtain quantitative data

that can be used to relate propellant composition and operating environment to the behavior of solids (Al, Al<sub>2</sub>O<sub>3</sub>) within the grain port and exhaust nozzle. The initial effort at the Naval Postgraduate School (NPS) has been directed at developing and comparing experimental techniques for obtaining detailed experimental data on the effects of initial aluminum size and operating pressure on the particulate characteristics within the gas phase. Four experimental techniques have been used:

a. High speed cinematography for the observation of strand burners within a combustion bomb and a 2-D slab motor under different operating pressures.

b. Post-fire residue collection and examination with a scanning electron microscope (SEM).

c. Scattered laser power spectra measurements to determine the mean diameter and concentration of particles as they exit the exhaust nozzle.

d. Holographic observation of the combustion process of burning propellant strands and of burning propellant slabs in a cross-flow environment, using a 2-D, windowed motor.

The data obtained with varying initial Al size and operating pressure can be used to validate some of the basic assumptions employed in current combustion/performance prediction models. In applying all four of the above techniques, relative advantages and disadvantages of each technique (resolution, etc.) for obtaining these data need to be determined.

There are some known advantages and disadvantages for each of the above techniques. By using high speed motion-pictures of burning strands, the entire duration of the burning process can be recorded to provide data concerning the time-varying characteristics. In addition, the combustion pressure can be independently varied using a combustion bomb and the collection of post-fire residue is readily made. These tests are relatively easily conducted and

inexpensive. Taking high speed motion pictures of strand burners is a good technique for comparing burning surface details for different propellants, as well as for observing the macro-structure of the luminous flames<sup>22</sup>.

There is one major disadvantage of using propellant strands; the different burning environment in comparison with the actual one in a rocket motor. Thus, (a) there is no cross-flow over the burning surface and (b) burning agglomerates are quenched in the cold inert gas used to pressurize the bomb. In addition, the heat transfer to the burning surface and the related burning rate have been found to depend upon the dimensions of the propellant strand and those of the combustion bomb. The size of the flame envelope around the burning particles is also a function of pressure and propellant composition. The latter often prevents actual particle sizes from being obtained from the motion pictures. Intense back-lighting or laser illumination with narrow pass filtering can help improve the latter.

Other disadvantages of high speed cinematography include the image resolutions due to the optics employed and the film used, as well as due to the smoke and/or a high number-concentration of particles above the burning surface. In addition, the depth of field is limited if any appreciable magnification is employed.

Measuring the scattered laser power spectra from an aerosol is a well known method for obtaining the mean particle size and particle concentration without interfering with the flow. Application of the technique has had only limited success in practical combustion environments. A disadvantage of this method is that it can be used to determine only the mean diameter and not the size distribution of the particles. One major advantage is that the technique is not significantly hindered by high velocity environments.

The main advantages of the holographic methods are (a) resolution to less

than 10  $\mu\text{m}$  with the particle-surrounding flames eliminated by the use of narrow pass filters and (b) unique depth of field. Utilization of a two-dimensional slab motor with this method also provides a realistic combustion environment. In the disadvantages of this technique one would include that it yields data from just one or two instants of the combustion history. A major current disadvantage also lies in the time required for reduction of the data available in the hologram.

## II. METHOD OF INVESTIGATION

In this investigation three propellant burning configurations and four experimental techniques were employed to study the particulate behavior resulting from the combustion of seven metallized composite propellants (Table I).

Strands were burned in a combustion bomb at 34 and 68 atm using high speed motion pictures for observation. Post-fire particle collection/scanning electron microscopic (SEM) examination were also made.

A small end-burning motor using propellant NWC-1 was used in conjunction with measurements of scattered laser power spectra to determine the mean particle size ( $D_{32}$ ) at the nozzle exhaust plane. Exhaust collection/SEM examination was also conducted.

A windowed two-dimensional motor was used with the AFRPL ruby laser and holocamera to obtain holograms of burning propellants. Strand burners were used at 34 and 68 atm. A WGS-6A propellant slab was also burned at approximately 27 atm to demonstrate system capability for obtaining holograms in a cross-flow environment.

In each experimental method, system calibration/resolution limitations were determined in non-reacting flow environments before hot firings were conducted.

### III. EXPERIMENTAL APPARATUS AND PROCEDURES

#### A. COMBUSTION BOMB

##### 1. Apparatus

The nitrogen purged combustion bomb used had a core volume of approximately  $560 \text{ cm}^3$  and an internal diameter of 5cm. In its initial configuration it incorporated three optical quality, 2.54 cm diameter windows for lighting and photographic observation. After the initial investigation, the combustion bomb was modified to allow for the placement of the objective lens of the camera closer to the propellant strand by means of extension tubes. The thickness of the bomb wall was reduced to 2.54 cm in the area of the window facing the camera. The existing optical quality glass window of 2.54 cm thickness was replaced with one of 1.27 cm thickness and 1.91 cm diameter. The modification reduced the maximum allowable working pressure to 100 atm. A schematic of the original combustion bomb is shown in Fig. 1. Bomb modifications are shown in Fig. 2.

Motion pictures were obtained using a Hycam model K2004E-115 at a rate of 4000 - 5000 pps. An Elgeet 77mm/f1.9 lens was used with a 4.1 cm long extension tube. The system resulted in a 0.7x magnification with a depth of field at  $f/4$  of about 4mm. Movie film types included 7724 4x negative (ASA 400), 7222 2x negative (ASA 250), 7250 Ektachrome (ASA 250), 7239 Ektachrome (ASA 160) and 7267 Kodachrome (ASA 25). 7250, 7267 and 7239 all resulted in acceptable film quality. When the combustion bomb was modified, several new extension tubes were fabricated for the Hycam camera in order to increase the magnification on the film plane. The f1:9 lens was used on the end of the extension tube. The camera mounts were also improved by incorporation of expansion screws between the frame and mounting table.

The longer (7 cm) extension tube which was finally used on the camera, along with the combustion bomb modification and the camera mounts improvement, led to a 1.12x magnification on the film (versus the original 0.7x).

An SLM-1200 projector and a 650 watt focused flood light were used to provide side lighting and back lighting as required. A schematic of the apparatus is shown in Fig. 3 and a photograph in Fig. 4.

Small propellant strands (10mm high, 7mm wide, 2mm thick) were ignited with a nichrome wire.

## 2. Procedures and System Calibration

Six propellants were selected for testing. The propellant formulations are listed in Table I. The first four propellants listed (WGS-5A,6A,7A,7) were specially formulated and provided by the Aerojet Solid Propulsion Company. They represent a family of the same composition by weight where the only variable was the size of the spherical aluminum particles. Three propellants were provided by the Naval Weapons Center. Two (NWC-1,2) contained only a small amount of  $Al_2O_3$  particles as a metal additive. Propellant N-7 contained 15% aluminum. All propellants except N-7 contained 12% HTPB.

Propellant strands were cut to a size that would fill the field of view of the high speed camera. The strands were cemented to stainless steel pedestals which fit into the propellant sample mounting post in the combustion bomb. Schematics of the propellant strands are given in Figure 5. The tops of the strands were cut horizontally during the initial phase of testing. Subsequently, the tops were cut at a 45° angle to permit better observation of the burning surface.

Propellant strands were burned in a nitrogen environment within the combustion bomb. Four tests were conducted with each propellant: (1) particle collection at 34 atm, (2) particle collection at 68 atm, (3) high speed

motion pictures at 34 atm, and (4) high speed motion pictures at 68 atm.

Tables II and III summarize the test conditions for the particle collection and the high speed motion pictures respectively.

It was found that the nitrogen purge required for motion picture studies significantly affected the post-fire particle size distribution. All particle collection tests were therefore conducted in a nitrogen environment without purge. The propellant strands in the latter tests were burned inside a (4.5 cm diameter, 2.5 cm high) stainless steel tube within the combustion bomb. The residue collected from the tube wall was ultrasonically cleaned in ethanol, dried in a heated vacuum evaporator, and then mounted on pedestals for SEM examination using a very thin layer of epoxy. The samples were then gold coated (100 to 200 Angstroms thick) in a Denton Vacuum Evaporator with a DSM-5 sputter module. Particle size analysis was done on an Hitachi S-450 scanning electron microscope with magnifications from 50x to 2000x.

A series of photomicrographs were taken with the SEM of each of the samples. Each series consisted of the following: (a) one large scale view at 90° incidence to present an overview of particle size distribution and the surface density of particles on the sample holder, (b) two small scale oblique views at 15° incidence to show the manner in which the particles were imbedded in the epoxy layer, and (c) two small scale views at 90° incidence corresponding respectively to the same local areas that were photographed in the oblique views. The latter two views were utilized to count particles and measure particle diameters.

To ascertain the resolution capability of the high speed motion pictures, the USAF 1951 resolution target was utilized. Fig. 8 presents two frames taken from the motion picture films: (a) using the original bomb and extension tube and (b) using the modified bomb, longer lens extension tube, and improved

camera stabilization. The presented photographs do not allow the system resolution to be determined. The films viewed on a screen are much clearer, resulting in resolutions of approximately  $70 \mu\text{m}$  (2/6) in Fig. 8(a) and  $14 \mu\text{m}$  (5/2) in Fig. 8(b). Various film types were tested. For most film types, the resolution target was photographed twice: (1) through the window of the combustion bomb, and (2) with the window removed. Table V lists the resolution target test conditions.

## B. DIFFRACTIVELY SCATTERED LIGHT MEASUREMENTS

### 1. Background

Based on a theory by Gumprecht and Sliepeevich<sup>23</sup>, describing the scattering properties of a poly-dispersion, an investigation of the light scattering technique was conducted by Chin, Sliepeevich and Tribus<sup>24</sup>. A more generalized theory on the same subject was later discussed by Dobbins, Crocco, and Glassman<sup>25</sup>, though applicable only to certain types of droplet size distributions. After the introduction of the "upper-limit distribution function" (ULDF) by Mugels and Evans<sup>26</sup>, Roberts and Webb<sup>27</sup> concluded that the volume - surface mean diameter  $D_{32}$  of a polydispersion may be determined from the intensity of diffractively scattered light from spherical particles without any knowledge of the general distribution type. Dobbins and Jiznagian<sup>28,29</sup> also concluded that the mean scattering cross section of particles depends primarily on the mean diameter  $D_{32}$ , regardless of the size distribution function, when the refractive index is near unity. Also, Hodkinson<sup>30</sup> showed that the ratio of scattered light intensities at two forward angles is relatively insensitive to particle refractive index and concentration, and that this ratio yields a measure of the volume-surface diameter  $D_{32}$ .

Based on the above background a method was developed for estimating the volume-surface mean diameter  $D_{32}$  of a polydispersion of particles by means of diffractively scattered light intensities. This method has been used by A. S. Nejad, et al<sup>31</sup> for measurement of the mean droplet diameter resulting from atomization of a transverse liquid jet in a supersonic air stream as well as by others for particles of different nature. Powell, et al<sup>32</sup> used this technique combined with light transmission measurements for the simultaneous estimation of mean diameter, refractive index and volume concentration of aerosols.

## 2. Apparatus

A schematic diagram of the experimental apparatus is shown in Fig. 7. The optical equipment was mounted on a optical bench with one degree of freedom (vertical). An 8mw helium-neon laser was used as the light source. A spatial filter/beam expander located directly in front of the light source produced a uniform light beam with a one centimeter diameter. A plano-convex lens (5cm in diameter with a focal length of 500mm) was used as the condensing lens to focus the unscattered light beam on the aperture of the photosensor. The photosensor assembly had two degrees of freedom (vertical and horizontal) and consisted of a photo-diode with a  $5.1\text{mm}^2$  active area, its operating circuit, a narrow pass filter, and a small aperture (pinhole). The total length of the detector housing tube was 25.4cm and its diameter was 7.62cm. The aperture plate was located 23cm in front of the photodiode, so that the density of the light reaching the sensor would be well below the maximum allowed. A 0.153mm pinhole was used for calibration runs. For the actual runs, a 0.560mm pinhole was employed because the beam radius was reduced to 1.09mm.

## 3. Experimental Procedures and System Calibration

An attempt to develop a "well behaved" apparatus set-up in an open test-cell of the Combustion Laboratory only proved the sensitivity of the technique to external noise sources (atmospheric particles, etc.). This required the whole apparatus to be enclosed in a reasonably dust and light free environment.

The accuracy of the Diffractively Scattered Light Method (DSL) for obtaining the mean diameter of particles was then investigated. A comparison was made between experimentally obtained non-dimensionalized intensity ( $I(\theta)$ ) versus non-dimensional angle ( $\bar{\theta}$ ) profiles and the "universal" theoretical profile presented in Figure 8. Various profiles were obtained using glass beads of different sizes. Translation of the detector was done manually by

means of a micrometer. The glass beads were suspended in distilled water contained in a home-made, plexiglas (6.4cm x 7.6cm x 6.4cm) container. A magnetic stirrer was used to assure a constant density of glass beads in suspension. The same stirrer was used for the light-scattering measurements of plain water for the same reasons, since the water could not be taken as without any foreign particles in it. Thus, the intensity profiles for plain water, as well as for 53-64 $\mu$ m, 37-44 $\mu$ m and 1-37 $\mu$ m glass beads were determined. The measurements would start at a relatively large (for the given size of particles) distance from the centerline and continue until an abrupt increase of the output voltage would be noticed. An abrupt increase would not result from the intensity of forward scattered light, but rather from transmitted light. The DSL intensity at the centerline was found by extrapolating the "near-centerline" profile. Experience showed that the last reliable measured voltage would be at a distance from the centerline of 2.5 to 3 times the pinhole diameter. The measured voltages in each case were plotted against the distance from the centerline as shown in Fig. 9. Then  $I(\theta)$  versus  $\bar{\theta}$  curves were constructed for each case by calculating the pairs of values from the definitions:

$$I(\theta) = \frac{I_{\theta,p} - I_{\theta,o}}{I_{cl,p} - I_{cl,o}} = \frac{V_{\theta,p} - V_{\theta,o}}{V_{cl,p} - V_{cl,o}} \quad (1)$$

where,  $I_{cl}$  or  $V_{cl}$  are the extrapolated light intensity and related voltage at the centerline, and  $I_{\theta}$  and  $V_{\theta}$  are the light intensity and voltage at an angle  $\theta$  (Fig. 10).  $o$  and  $p$  symbolize "no particles" and "with particles", respectively.

Also

$$\bar{\theta} = \frac{\pi D_{32}}{\lambda} \theta \quad (2)$$

In equation (2)  $D_{32}$  for the spherical particles was taken to be the mean diameter determined from SEM photomicrographs.  $I(\theta)$  versus  $\bar{\theta}$  curves are plotted for each bead sample and compared to the theoretical profile in Fig. 8.

It was found that (1) large deviations from the universal curve occurred at  $\bar{\theta}$  larger than 3 to 4 and (2) the agreement with the universal curve was dependent on the sample mean diameter with deviations increasing as  $\bar{D}$  decreased.

Both of these limitations could be related to the far from ideal conditions in the test area, namely; to the influence of the Plexiglas walls of the container on the scattered light and the multiple reflections on the walls. The ratio of the non-diffractively scattered light (noise) to the diffracted one was increasing with increasing  $\theta$ , as expected.

The much larger discrepancy for the 1-37  $\mu\text{m}$  sample was also largely related to the fact that the inaccuracy of the DSL technique increases as the ratio  $\frac{\bar{D}}{D_{\infty}}$  decreases, where  $D_{\infty}$  is the largest diameter expected in the sample<sup>25</sup>.

By the same procedure (Fig. 11) the  $I(\theta)$  versus  $\theta$  curve for a sample of  $\text{Al}_2\text{O}_3$  powder with mean diameter 91  $\mu\text{m}$  was constructed (Fig. 8). Two different aluminum oxide particle number densities were used with transmittances  $\frac{E}{E_0} = 0.34$  and  $\frac{E}{E_0} = 0.17$ . The second transmittance was below the suggested limit of 0.223, but it was chosen for comparison purposes. A very close agreement with the universal profile was noticed at  $\bar{\theta} < 2$ . It should be noted that for this sample the maximum diameter present was  $D_{\infty} = 140 \mu\text{m}$ .

Three basic conclusions were drawn from the above calibration experiments:

(1) The diffractively scattered light technique works reasonable well using a photodiode instead of a photomultiplier tube as used by previous investigators.

(2) The accuracy of the data obtained was very good at small  $\bar{\theta}$  and high  $\frac{\bar{D}}{D_{\infty}}$ . As mentioned earlier, small  $\bar{\theta}$  were necessary to neutralize the effects of the container walls. The problem was compounded for particles with smaller mean diameters, since accurate measures are required at larger scattering angles.

(3) The deviation from the universal curve increased with decreasing  $\frac{\bar{D}}{D_m}$ . This was especially noticeable in the 1-37  $\mu\text{m}$  sample curve where  $\frac{\bar{D}}{D_m} = 0.378$  and the spectrum of the diameter sizes was broader.

For the motor firings an end burning grain (3.0cm diameter x 2.5cm long) of NWC-1 propellant was burned (1.0% by weight of 8  $\mu\text{m}$  diameter  $\text{Al}_2\text{O}_3$ ). The nozzle throat diameter was 2.8mm. The combustion pressure was recorded on a Visicorder oscillograph along with the photodiode output voltage. The latter was also recorded on an oscilloscope with provision for taking pictures of the trace. A home-made translation mechanism was used for the photosensor to scan the intensity profile of the scattered light. A linear potentiometer was also employed to determine the distance traveled by the sensor.

The translation mechanism had a travel distance of 4.9cm and was energized remotely by means of an electric solenoid. The motor firing was also done remotely. An aluminum tube surrounding the exhaust jet was used to restrict the exhaust particles, protect the optics, and also to allow collection of particles for microscopic examination.

The actual runs of the DSL experiments started with calibration of the recording equipment. The focal point of the laser beam after the condensing lens was placed at a distance of 3mm from the pinhole centerline. This offset distance was chosen as a compromise between the Visicorder input voltage limits and the necessity for the recording of low voltage values corresponding to intensities far from the pinhole, (i.e., for getting a reasonable sensitivity).

When the electric solenoid was energized the pinhole and the sensor scanned the scattered light intensity for a horizontal distance of 4.9cm.

A "cold" run was done first, with no particles in the scene volume and the "zero scattering" profile was recorded. Then the motor was fired. When the pressure in the combustion chamber reached a constant value (13 atm), the

solenoid was activated. The constant-pressure burning lasted for 7 seconds and the scanning commenced at about 2 seconds after constant pressure was reached. The DSL intensity was again recorded versus time and travel distance of the pinhole.

Residue of the exhaust particles was collected from the aluminum tube. Some of it was cleaned by means of acetone and an ultrasonic vibrator, and then dried in a vacuum oven. Both "clean" and "as-collected" samples of the residue were examined with an SEM. From these pictures the diameters of the  $\text{Al}_2\text{O}_3$  and other particles were measured.

## C. MOTION PICTURE AND HOLOGRAPHIC MEASUREMENTS IN TWO-DIMENSIONAL MOTOR

### 1. Background

Holography is a technique used for recording of visual information. It is different than classic photography in that both amplitude and phase information are recorded. By means of proper illumination of the developed record (hologram), a three-dimensional image of the original scene can be obtained. Holographic systems have been used since the mid-sixties for recording relatively large volumes of particles in the size range from 3-1000  $\mu\text{m}$  mean diameter<sup>33</sup>. The technique has had limited application to solid propellant combustion<sup>20,21,35</sup>. The use of a pulsed laser as the holographic light source satisfies the requirements for a high degree of spatial and temporal coherence while limiting the exposure time.

In this investigation it was desired to obtain holograms of propellant combustion in both strand (zero cross-flow) and slab (with cross-flow) configurations. The latter required the design and development of a suitable two-dimensional motor which would provide a realistic flow environment while at the same time allowing laser light to be transmitted through the combustion zone with sufficient intensity to expose a holographic plate. In addition, specialized reconstruction methods had to be used in order to permit observation of the smaller particulates.

### 2. Two-Dimensional Slab Motor

The 2-D motor was originally designed to permit opposed slabs of propellant to be burned to pressures of 204 atm. The motor was designed with two 1.27 cm diameter, high-quality glass windows to allow for the recording of the burning. Nitrogen purge was provided from the bottom of the motor for keeping the windows clean. This technique worked well for small strands burned near the center of the motor (i.e., the 2-D motor was used as a conventional purged and windowed combustion bomb in order to obtain holograms of burning strands).

However, the purge system was found to be inadequate when "large" quantities of propellant (slab motors) were burned. The motor was therefore modified by adding (1) window shutters, (2) a small nitrogen purge in the window ports, and (3) a secondary pressurization chamber.

The shutters remained closed with the purge system operating until steady state conditions were reached. At that time, a combustion chamber pressure sensor triggered a solenoid, and via a time delay, released the spring loaded shutters. The rising shutters in turn tripped a microswitch at the end of their travel and fired the laser. Pressure-time plots were provided by a Honeywell Visicorder which also marked the various events as they happened.

Mounted atop the propellant chamber was an additional chamber for the introduction of pressurizing nitrogen. This chamber reduced the tendency of the pressurizing nitrogen to cause recirculation in the combustor, allowing the combustion products to clear the viewing area. A converging nozzle was also used between the two chambers to minimize recirculation effects. This secondary chamber allowed high pressures to be used without large quantities of propellant. A .0.16 cm throat diameter graphite nozzle was secured to the exit of the pressurization chamber. This apparatus is shown in Figures 12, 13 and 14. A photograph of the motor (with high speed camera set-up) is shown in Figure 15. Additional photographs of the original motor are presented in Figures 16 and 17. Plexiglas spacers were used when propellant slabs were burned in order to minimize the motor free volume (Figures 12 and 14). When only one propellant slab was burned another L-shaped (metal) spacer was used in place of the opposed propellant slab (Figure 13).

### 3. Pulsed Ruby Laser

The TRW/AFRPL pulsed ruby laser<sup>36</sup> was used in this investigation for recording the propellant burning on holographic plates. When operated in the

Q-switched mode, the system emits single or double Q-switched pulses of approximately 1 joule total energy and approximately 50 nanosecond duration at 0.6943 microns. The pulse chopper reduces the duration of a single pulse to < 10 nanoseconds. Similarly, the pulse energy is reduced to a maximum of approximately 1/4 joule. The laser and related power supplies are shown in Fig. 18. Both the 50 nanosecond and 10 nanosecond pulses provided sufficient light intensity for recording the burning of small strands. Neither pulse was adequate for the slab motor. For this reason the beam diverging lens within the laser was changed to reduce the final beam diameter from approximately 7.5 cm to 3 cm, resulting in increased power density in the scene beam. This modification permitted holograms to be taken of slab burners using the 50 nanosecond pulse.

#### 4. Holocamera

The lens assisted holographic system used was provided by the U.S. Air Force Rocket Propulsion Laboratory, Edwards, California<sup>37</sup>. The services of Mr. R. A. Briones of R<sub>1</sub>R<sub>2</sub> Company were obtained to provide initial check-out and alignment of the apparatus. The distinguishing feature of this system is the holocamera in which the AFGA-GEVAERT 8E75 HD film plate is mounted on a kinematic plate holder which holds the plate during both recording and reconstruction of the image. A photograph of this system placed around the 2-D slab motor is shown in Figure 19.

Practically all holograms were recorded by using diffuse illumination. This had to be done since the collimated - mode scene beam caused sharp refractive effects. At higher pressures and with highly metallized propellants the refraction by the thermal cells prohibited identification of particles.

Various glass diffusers of different opacity were used for different types

of propellants. The "optimum" (for each propellant - pressure combination) diffuser was determined experimentally. Essentially, as more smoke was produced, a more intense scene beam was required. This required a less opaque diffuser glass. Along with each diffuser a neutral density filter of "matching" transparency was used to reduce the light intensity of the reference beam and bring it to the correct intensity ratio with the scene beam.

Thermal cell effects were minimized with the diffuse light, since the illuminating light was scattered evenly over a wide range of angles and as a result, the thermal cells were averaged<sup>37</sup>. The presence of thermal cells was still observed with highly aluminized propellants but within tolerable limits, not affecting the particulate discrimination. Another problem, however, was introduced by the use of the diffusers. This was the reduced resolution due to speckle effects. These effects were further enhanced due to the fact that a CW He-Ne laser was used for the reconstruction.

#### 5. Reconstruction Apparatus

Image reconstruction was provided by a Spectra-Physics Model 125 He-Ne CW gas laser with an output of 80 milliwatts at .6328 microns. To view a hologram the film plate was rear illuminated by the reconstruction laser and the projected image was viewed with a variable power microscope. This method ensures that aberrations of the scene beam caused by the focusing lenses cancel as the image is projected back through the optical system and better resolution is obtained. Microphotographs of the projected holographic images were made on Kodak Ektrachrome 64, 35mm slide film, using a Canon Model F-1 camera mounted on the microscope. The Canon Model F-1 allows for the use of various ground glass focusing plates. This permits optimum focusing of the image on the film plane for different light intensities from the hologram. The microscope and Kinematic Plate Holder were mounted on an optical bench

to provide stability and to ensure consistency of results for each photograph. This apparatus was placed in a dust-free dark room in order to maximize the obtainable resolution in the reconstructed image.

In most of the reconstruction a revolving mylar disc was used at the reconstructed object location. This was done to suppress speckle during observation and picture taking<sup>37</sup>. A photograph of the reconstruction apparatus is shown in Fig. 20.

#### 6. Motion Pictures

A Red Lake Laboratories Hycam motion picture camera was used to record the high speed motion pictures of the burning propellant. The scene was back lighted by a 1200 watt Selectroslide Model SLM-1200 light source. Kodak 16mm Ektachrome 7239 film was used at f1.9 for all exposures. After developing, these films were used to provide a two dimensional dynamic view of the corresponding holographic representation and preliminary timing data for the initial holograms for each propellant sample. The movies could not be taken simultaneously with the holograms, but they were recorded under the same pressure-time parameters. The system arrangement is shown in Figure 15.

#### 7. Experimental Procedures

The initial investigation was conducted using the 2-D slab motor as a conventional, purged combustion bomb. Propellant strands were located near the center of the motor (in the window viewing area), mounted on a small screw to minimize purge gas recirculation. In this initial investigation the ruby laser was used in its manufactured configuration, (without the increased beam power density discussed above). A major problem in the recording of the strand burning was introduced by the smoke. The strand size has to be limited to a width of 4mm and depth of 1 to 1.5mm. In this way the quantity of the smoke was kept low enough for the scene beam to penetrate. The opacity of the

gases in the scene required that the intensity of the reference beam be reduced by means of neutral-density filters. This was necessary to maintain the necessary intensity ratio (approximately 5:1) of the two beams.

The insufficiency of the available laser power was also apparent when propellants with very small aluminum particles were burned. Thermal cells were introduced in that case and the only way to eliminate them after the use of a diffuser in the scene beam (which further reduced the laser intensity) was to use a pulse with a shorter duration than 50 nsec (i.e., 10 nsec). This resulted in even less available laser power and, therefore, most holograms were taken with a 50 nsec pulse.

After the initial investigation the diverging lens in the Ruby laser was changed, thereby reducing the beam size and consequently, increasing the power density of the beam. Only about one quarter of the original diameter was needed for the scene beam. This reduction in beam size, however, may result in less coherence and resolution capability.

A 0-80 screw was used on the side of each burning strand as a scale reference. The peak-to-peak distance between the screw threads was 317.5  $\mu\text{m}$ .

The next part of the investigation was concerned with developing a method for obtaining holograms of burning propellant in a cross-flow environment. Propellant slabs were rough-cut to approximate size, then hand rubbed to final dimensions. This rubbing also served to smooth any saw marks caused by the rough cut and removed any loose propellant which might have caused debonding of the inhibitor. Initially, quite large opposed propellant slabs (5cm long x 1.3cm web x 0.5cm thick) were used. These large slabs allowed the propellant to provide its own pressurizations; however, the smoke produced proved to be too dense for the laser to penetrate. Eventually, with the addition of a secondary nitrogen pressuration chamber and the

elimination of the opposing slab, a final propellant dimension of approximately 2.9cm x 1.3cm web x 0.06cm thick was employed.

In this configuration, the propellant had to provide only approximately five percent of the desired steady state combustion pressure. The major portion of the chamber pressurization was provided by the nitrogen introduced downstream of the propellant. The sample was epoxy bonded to a propellant support base and inhibited with a very thin coat of General Electric Hi-Temp Gasket (Red RTV), then allowed to cure for twenty-four hours. Other schemes examined to inhibit the propellant were to moisten the surfaces to be inhibited with water to dissolve a portion of the ammonium perchlorate (oxidizer) or to apply a thin coat of epoxy resin to the surface.

The system was prepared for firing by installing the propellant and the window blocks into the motor. The Plexiglas spacers were shimmed as necessary to ensure contact with the propellant and then the steel L-shaped spacer was attached. The ignitor charge was inserted into the gap in the steel L-shaped spacer and then primed with a small amount of black powder (and cellulose based glue dissolved in acetone) deposited on an electric ignition wire. After completing the assembly of the motor, the necessary electrical connections were made, the holocamera was set in place, and the laser was prepared for firing.

A firing sequence consisted of the following:

- (1) Check electrical connections and plug ignition wires into firing circuit
- (2) Charge the laser to its firing voltage
- (3) Start the Visicorder
- (4) Pressurize the motor with nitrogen to about 475 psi for a desired test pressure of 500 psi

- (5) Fire the ignition switch
- (6) Propellant ignites and combustor pressure builds
- (7) Pressure sensor monitors combustor pressure and starts time delay at preset pressure
- (8) Time delay expires and energizes window shutter solenoid
- (9) Solenoid retracts and releases window shutters
- (10) Window shutters open
- (11) Window shutters trip laser fire microswitch, opening holocamera shutter and laser fires.

The sequence of events 3-11 usually took less than 4 seconds to complete.

After the film plate was exposed, it was removed from the plate holder in a dark room and processed as follows:

- (1) Kodak D-19 developer was used as the processing agent. The plate was bathed from 1 to 3 minutes and inspected periodically under a Kodak safelight. When a satisfactory "image" had formed, the plate was removed to a fresh water rinse than placed in the fixer.
- (2) Kodak "Rapid Fix" was used to set the image. Processing time was 5 to 7 minutes.
- (3) After fixing, a 15 minute fresh water wash was conducted followed by 30 seconds in Kodak "Photo Flo" solution, then the plate was hung to dry.

#### 9. System Calibration

The resolution limits of the holographic system were determined by placing a 1951 USAF resolution target in the 2-D motor at the propellant location. The resolution limit obtained was approximately 11  $\mu\text{m}$  (using a diffuse scene beam and the spinning mylar disc).

Unfortunately, the photographic recording of the scene observed through

the microscope destroys some of the resolution. A photograph of the reconstructed resolution target is shown in Figure 21. 5/4 (11  $\mu\text{m}$ ) was readily observed through the microscope. With very careful construction/operation of the rotating mylar disc 6/1 has been obtained (7.8  $\mu\text{m}$ ).

Particle sizing was done by comparison with a 0-80 screw which was placed in the window port during the combustion experiments. Fig. 22 presents a photograph of the reconstructed image of the screw from a combustion experiment (317.5  $\mu\text{m}$  peak-to-peak).

#### IV. RESULTS AND DISCUSSION

##### A. COMBUSTION BOMB INVESTIGATION - MOTION PICTURES AND PARTICLE COLLECTION

###### 1. Postfire Particle Size Analysis

Approximately 13% of the metal cast into the propellant was recovered from the collection tube for particle size analysis. The technique developed for collecting and preparing postfire residue for SEM analysis was found to be satisfactory. Multiple tests and varying amounts of residue mass resulted in essentially the same particle size distribution. SEM photomicrographs of the collected residues are presented in Figures 23 through 34.

Because of the large number of tests conducted, initial particle size distributions were determined using a limited number of particles (40 each). Plots of particle distributions for the test conditions specified in Table II are presented in Figures 35 through 46. The plots indicate a bi-modal particle size distribution. The bi-modality is typical for aluminum combustion products. Experimental data from previous investigations suggest that condensed phase oxidation of aluminum contributes to coarse residue, whereas vapor phase oxidation results in fine residue<sup>38</sup>. Shedding of fine particles by burning agglomerates is another possible mechanism. Due to the bi-modal character of these particle size distributions, two average diameters are presented on each plot. One applies to the fine particle distribution and the other to the coarse particle distribution. For the WGS-7, NWC-1, and NWC-2 propellants with initial metal powder mean diameters of about 8  $\mu\text{m}$ , bimodal particle size distributions were not discerned. For these propellants the average diameter of the entire sample is given in the respective figure.

The number of particles which must be sized from the SEM photographs in order to obtain a statistically valid sample size depends upon a number of conditions: (a) percentage of residue that is collected, (b) how the residue

is collected and washed, (c) how the residue is distributed on the SEM sample holder, and (d) how the particles in the photographs are selected for counting. One thousand particles have been counted by some investigators<sup>38</sup>, but fewer may be used.

To determine how closely the forty particle distributions would compare with distributions for larger numbers of particles, two samples were selected for more detailed analysis. Approximately 220 particles were measured in each of the tests. Comparisons of the 40 particle distributions with the 220 particle distributions are shown in Figures 47 and 48. The computed average diameters of fine and coarse particle distributions between the respective samples was in good agreement, although the larger sample in both cases generated slightly smaller average diameters. These results indicated that the forty particle samples provided at least closely representative size distributions for the total particulate residue.

A plot was constructed of the average initial aluminum particle diameter in the propellant versus the average postfire particle diameter. This data is presented in Figure 49. A reference line with unity slope was superimposed on the data as an aid in size comparison. The data indicated that the mean diameter in the coarse particle distribution of the postfire residue closely matched the initial aluminum size in the cast propellants. The mean diameters in the fine postfire particle distributions were approximately 10  $\mu\text{m}$  but increased slightly with increasing aluminum size. These results appear to indicate that little agglomeration occurred and that many of the aluminum particles which left the surface were rapidly quenched. Preliminary results from tests at the Aerojet Solid Propulsion Company with the same propellants have indicated that no significant agglomeration occurred and that metal combustion proceeded almost to completion (i.e., yields primarily  $\text{Al}_2\text{O}_3$ )<sup>39</sup>.

$\text{Al}_2\text{O}_3$  particles typically have smooth surfaces when compared to quenched aluminum particles. Almost all particles collected in this study were quite smooth, which agrees with the Aerojet results.

## 2. High Speed Motion Picture Analysis

Measurements taken from the high speed motion pictures included resolution, propellant burning rates, the diameters of burning particles ejected from the surface, and the vertical velocities of burning particles.

With 0.7X magnification and thick (2.54 cm) optical windows the smallest particle that could be sharply focused on the film was approximately 70  $\mu\text{m}$ . Subsequent tests with thinner windows (1.27 cm), 1.12X magnification, and improved camera stability improved the resolution to particle sizes of approximately 14  $\mu\text{m}$ . The latter resolution was achieved at the expense of a very limited depth of field.

Figures 50 and 51 are prints of typical frames from high speed motion picture tests 1415250580 (WGS-5A, 34 atm) and 1100250580 (WGS-5A, 68 atm) respectively. A more dense particle distribution in the gas stream and more smoke are apparent in the test at the higher pressure. In addition, Figure 51 is an example of an uneven burning surface caused by the hot ignition wire falling against the side of the propellant during the ignition sequence. Stages in the general behavior of the aluminum can be seen in the photographs. What appeared to be molten aluminum particles/agglomerates were observed on the propellant surface before particle ignition. The particles/agglomerates appeared as regions more brightly illuminated than the surrounding surface area. The vertical movement of the particles began with an apparent ejection from the propellant surface into the gas stream. In some cases this ejection was a rapid "pop-up" and in others it took place much more slowly as if there were some adhesion near the surface. As the particles left the surface,

they ignited, and the diameters of the burning particles became larger than before ignition. Once ignited and separated from the surface, the particles moved with approximately constant velocity in the gas stream and exhibited a typical tail of flame pointing away from the surface. In this investigation, the general behavior of the aluminum was more easily observed for the propellants with initial aluminum particle diameters greater than 50  $\mu\text{m}$  and at a pressure of 34 atm. As initial aluminum particle diameters decreased and pressure increased, individual particles were less readily distinguished from the uniformly bright sheet of flame. Additionally, more smoke was present at 68 atm to obscure the surface.

The apparent diameters of burning particles in the gas stream were 7 to 12 times larger than the diameters of the initial aluminum cast in the propellant and the mean diameters of the postfire residue (Figs. 52 and 53). This raised the question as to the accuracy of the filming and/or postfire particle collection techniques employed. To clarify this, a sample of propellant WGS-6A was sent to NWC for analysis using their windowed combustion and particle collection bombs. These tests were conducted by Thom Boggs, Karl Kraeutle and Don Zurn. The NWC film data confirmed the large observed burning particle diameters and the particle collection bomb data agreed closely with the NPS data (Fig. 54). Thom Boggs has indicated that this "cat-tailing" upon ignition of the aluminum particles is due to the small aluminum concentration. With the small concentration the particles came off the surface without accumulation/agglomeration and the oxidizer rich atmosphere caused the oxide plume to "bloom" to diameters much larger than the actual particle size. This explanation is consistent with both the film and particle collection data.

The average velocities of several burning particles were measured in the region from the surface to 4 mm above the surface. Figures 55, 56 and

and 57 are plots of burning particle average velocity versus burning particle diameter for propellants WGS-5A, WGS-6A and WGS-7A respectively. For the other propellants, velocity data were not obtained due to the inability to distinguish individual particles from the dense, bright flame pattern. The velocity of the particles decreased as the diameter increased, as expected. This was a consistent trend for both particles from an individual propellant and for particles from propellant to propellant. The velocity of an individual burning particle was approximately constant in the gas stream except in some cases in close proximity to the surface where it was noted to be slower. Representative values are shown in Figures 55 and 56.

The burning rates of the propellants were determined by measuring motion picture framing rates and the position of the burning surface for 1 mm increments over a 3 mm length near the center of the propellant strand. This region was selected to allow a steady state burning rate to be developed and to avoid heat transfer effects near the bottom of the propellant strand due to the stainless steel mounting pedestal. Figure 58 is a plot of burning rate versus initial aluminum particle diameter. The burning rates were relatively constant at a given pressure with a very slight increase as initial aluminum particle diameter decreased. The burning rates at 68 atm were 17 to 19% greater than at 34 atm. These burning rates may not agree with burning rates obtained with larger propellant strands or in motors. Propellant strand dimensions can affect the burning rate through varying heat transfer effects and cross-flow velocities. 2-D and 3-D motors with larger propellant grains can also generate different burning rates.

Having determined the burning rates for both pressures tested, the exponent for the burning rate equation ( $r = ap_c^n$ ) was calculated for each propellant. The exponents are listed in Table V.

### 3. Summary of Results

Film resolution capabilities and propellant strand burning characteristics were determined for future comparison with results obtained using 2-D and 3-D propellant configurations with the additional diagnostic techniques of light scattering and holography.

Postfire particle size distributions were bi-modal in character. The mean diameters of the fine postfire particle distributions were approximately 10  $\mu\text{m}$  in all cases, and increased slightly with increasing initial aluminum size. The mean diameters of the coarse postfire particle distributions were approximately the same size as the initial aluminum cast in the propellant, implying that little surface agglomeration and rapid quenching occurred.

The technique developed for collecting and preparing postfire residue for SEM analysis was satisfactory. Spectral analysis of postfire residue to determine composition could possibly provide additional data to correlate with fine and coarse postfire particle size distributions.

A minimum particle size of approximately 14  $\mu\text{m}$  could be sharply focused with the high speed motion pictures using 1.12X magnification.

High pressure ( 68 atm) and small initial aluminum size (less than 50  $\mu\text{m}$ ) limited the utility of high speed motion pictures. High burning rates, number concentration of burning particles on the surface and in the gas stream, and smoke generation, all contribute to this problem. Improvement in this area could possibly be made by using laser light illumination together with narrow pass filters in front of the camera lens.

The apparent diameters of burning particles in the gas stream were 7 to 12 times larger than the diameters of the initial aluminum cast in the propellant and of the mean diameters of the postfire residue. This was apparently due to the unique properties (overoxidized) of the particular propellants

employed.

The velocity of any particular burning particle was nearly constant in the gas stream once it departed the region very near the burning surface.

Smaller particles traveled at higher velocities as expected.

Propellant burning rates were approximately constant at a given pressure with only a slight increase for propellants with smaller initial aluminum size. Burning rates at 68-atm were approximately 17% higher than at 34 atm.

## B. DIFFRACTIVELY SCATTERED LIGHT MEASUREMENTS

The photodiode output voltages obtained with and without the motor firing are shown in Figure 59. SEM photomicrographs of the "cleaned" and "as collected" nozzle exhaust products are presented in Figures 60 and 61 respectively. Particle diameter counts from the two photomicrographs are shown in Figures 62 and 63.

Using Fig. 59, the scattered intensity (voltage) at the centerline was found by extrapolation for the "cold" run (163.9 mV) and the "hot" run (183.1 mV). Then several distances from the pinhole were picked and  $I(\theta)$  was calculated for each one as described earlier. By using the "universal curve" (Fig. 8) the corresponding values of  $\bar{\theta}$  were obtained. The volume-surface mean diameter  $D_{32}$  was calculated from the equation  $\bar{\theta} = \pi D_{32} \theta / \lambda$ . The values obtained are tabulated in Table VI.

The "as-collected" exhaust had only a relatively few  $Al_2O_3$  particles (of circular cross-section) present. The other residue appeared to be from the inhibitor used on the sides of the end burning grain. The  $Al_2O_3$  particles had a mean diameter of 7.4  $\mu m$ , e.g., practically the same as the original particles cast in the propellant. The presence of large amounts of inhibitor residue obviously affected the scattered light intensity profile and the calculations. Future experiments will use internally burning grains to minimize this problem.

The volume-surface mean diameter  $D_{32}$  of the exhaust particles is tabulated in Table VI as a function of the forward scattering angle  $\theta$ . A large deviation is observed at  $\theta = 0.012$  rad, which probably was related to the inaccurate determination of the output voltage at that angle due to the voltage curve being very steep in that region (Fig. 59). Therefore, this value of  $D_{32}$  should be disregarded.

The remaining larger angles resulted in an average  $D_{32}$  of approximately 20  $\mu\text{m}$  with a spread of approximately 1.3  $\mu\text{m}$ , when the "universal curve" was used. Reference 27 suggests that the best choice for determining  $D_{32}$  is the region near  $I(\theta) = 0.08$ , where the standard deviation as calculated from different distributions of droplet size is only slightly greater than 1%. Following this advice  $D_{32} = 19 \mu\text{m}$ . This value was 1.7 times larger than the measured (SEM) mean diameter of the exhaust particles. A small part of this difference may be related to the fact that  $D_{32}$  is about 10% greater than the mean diameter, when the particles are not all the same size spheres. In addition, the ratio of the irregularly shaped exhaust particle surface area to their mean diameter is expected to be larger than for a sphere for which the theory was developed.

However, if the calibration curve for particles of diameters 1-37  $\mu\text{m}$  (Fig. 8) was used instead of the "universal curve", the average  $D_{32}$  was found to be approximately 12  $\mu\text{m}$  (approximately 11  $\mu\text{m}$  with  $I(\theta) = 0.08$ ). Both values were in good agreement with the mean - diameter of the "uncleaned" exhaust particles (11.5  $\mu\text{m}$ ).

The accuracy of the initial results was limited by both the motor configuration (end-burning grain with excessive inhibitor in exhaust products) and the method used for obtaining the scattered light profiles (a translating photodiode). However, the technique appears to work reasonably well and should provide a good means for obtaining data on the effects of propellant properties, motor operating characteristics and nozzle geometry on the particle diameter changes that occur across the exhaust nozzle. In order to improve the obtainable results, future testing will use an internally burning grain and linear arrays of photodiodes (vs. one in translation).

## C. HOLOGRAPHIC INVESTIGATION

### 1. Strand Burners

A major problem in the recording of the strand burning was introduced by the smoke. The strand size had to be limited to a width of 4 mm and depth of 1 to 1.5 mm. In this way the quantity of the smoke was kept low enough for the scene beam to penetrate. The opacity of the gases in the scene required that the intensity of the reference beam be reduced by means of neutral-density filters. This was necessary to maintain the necessary intensity ratio of the two beams. The problem could quite possibly be alleviated if the laser power was higher.

The insufficiency of the available laser power was also apparent when propellants with very small aluminum particles were burned. Thermal cells were introduced in that case and the only way to eliminate them after the use of a diffuser in the scene beam (which further reduced the laser intensity) was to use a pulse with a shorter duration than 50 nsec (i.e., 10 nsec). This resulted in even less available laser power and, therefore, most holograms were taken with a 50 nsec pulse.

Good quality holograms were obtained of propellants WGS-5A, 6A, 7A, 7 and N7 burned at pressures of 34 and 68 atm. Particle size data was readily obtainable from all the holograms except those for propellant WGS-7. Particle sizes produced by WGS-7 (7-8  $\mu\text{m}$ ) were smaller than the current resolution (11  $\mu\text{m}$ ) using a diffuse scene beam. Representative photographs of the holograms and corresponding frames from the high speed motion pictures (from the combustion bomb investigation) are presented in Figures 64 through 71.

Actual sizes of the particulates can be obtained from the holograms, eliminating the flame envelopes present in the movie pictures. The particle sizes measured from the holograms were the same as those in the cast

propellant, in agreement with the post-fire residue analysis discussed above.

No agglomeration and no noticeable pressure effects on mean particle diameter were observed in the holograms. This also agreed with the SEM data presented above.

## 2. 2-D Slab Motor

The laser power available from the pulsed ruby laser was adequate for obtaining holograms of the burning of small propellant strands. It was found to be inadequate when attempting to take holograms of propellant slabs. For this reason the laser beam diameter was reduced by changing the output diverging lens, increasing the power density by a factor of approximately six. No significant reduction in resolution was noticed when this change was made.

A technique for obtaining holographic recordings of the combustion process in a two-dimensional solid propellant rocket motor was developed during this investigation. A hologram of WGS-6A propellant was recorded at a steady state pressure of 29 atm in a cross-flow environment (of approximately 1.5 m/sec) with a laser pulse of 50 nanoseconds duration. Figure 22 is a reconstructed hologram of a 0-80 screw which was placed in the window hole to provide a scale for particle size determination. The threads are 317.5 microns from peak-to-peak. Figure 72 is a reconstructed hologram of the burning propellant. The vertical propellant surface is on the right side and the flow direction is upwards. The large particles are apparently pieces of binder or inhibitor. No appreciable agglomeration of aluminum was evident at this stage of the combustion process.

Greater laser power may be required to provide sufficient power densities to penetrate the smoke in the motor for propellants containing more aluminum or for thicker slabs. In addition, increased scene beam light intensity on the hologram could be obtained by enlarging the exit window of the motor. This

would allow more laser light from inside the motor to fall on the film plate, and would effectively increase the output power density without modification to the input beam. This modification is currently being made.

Motion pictures were also taken of WGS-6A at 1000 and 4000 frames per second and of WGS-7A at 4000 frames per second with both propellants at a steady state pressure of 29 atm. Figure 73 is a photograph of a frame from the test using propellant WGS-7A. Observation of the particle paths in each of these motion pictures provides visual verification of cross-flow conditions. As would be expected, those particles with the smaller initial sizes tended to track the cross-flow velocity field more closely than the larger particles.

## V. CONCLUSIONS

The goal of this initial investigation was to develop and compare experimental techniques that could be used for obtaining quantitative data on the effects of propellant properties, operating pressure and nozzle geometry on the behavior of metallized particulates within the grain port and nozzle of solid propellant rocket motors. The techniques employed were high speed motion pictures of strand burners and slab burners in a cross-flow environment, SEM analysis of post-fire residue (strand, slab, and motor), determination of  $D_{32}$  at the exit of an exhaust nozzle using measurements of scattered laser power spectra, and holograms of burning propellant strands and slabs in a cross-flow environment.

All techniques were successfully developed and employed to obtain particulate size data from a series of specially formulated propellants. It was not the purpose of this initial investigation to obtain data for current propellant compositions, but rather to demonstrate the ability to obtain the data. The propellants employed (except for one) produced particulate diameters in the gas phase that were essentially identical to those cast in the propellant. Thus, wide ranges in particulate size were neither expected or observed in the films or holograms.

The motion picture and holographic techniques were successfully demonstrated for operating pressures of 34 and 68 atm. and with up to 15% aluminum. Fourteen  $\mu\text{m}$  resolution was obtained in the high speed motion pictures with a 1.12X magnification (and very small depth of field) and an eleven  $\mu\text{m}$  resolution was obtained in the holograms.

Several improvements are required before the full set of techniques can be used together to obtain quantitative data from solid propellants with arbitrary composition. These are:

- (1) Use of laser light illumination and narrow pass filters with the

high speed motion pictures in order to eliminate the flame envelopes around the burning particles,

- (2) Use of photo-diode linear arrays in place of the translating photo-diode in order to improve the accuracy of the measurement of scattered laser power spectra.
- (3) Incorporation of a second diode array at the nozzle entrance so that particulate changes across the nozzle can be measured.
- (4) Increasing the power density that reaches the holographic plate by both laser and 2-D motor design changes.
- (5) Improving the obtainable resolution in reconstructed holograms through the use of better speckle removal techniques.
- (6) Development of techniques for automated data retrieval from holograms.

The first five items are being accomplished in the continuing effort at the Naval Postgraduate School.

## REFERENCES

1. Crump, J. E., Prentice, J. L., and Kraeutle, K. J., "Role of the Scanning Electron Microscope in the Study of Solid Propellant Combustion: II Behavior of Metal Additives", *Comb. Sci. and Tech.* Vol. 1, Nov. 1969, pp. 205-223.
2. Boggs, et al., "Mechanisms of Combustion", NWC report NWCTP5514, July 1973.
3. Kraeutle, K. J., "Particle Size Analysis in Solid Propellant Combustion Research", Experimental Diagnostics in Combustion of Solids, AIAA, *Progress in Astronautics and Aeronautics*, 1978, Vol. 63, pp. 76-108.
4. Barrere, et al., Rocket Propulsion, Elsevier Pub. Co., 1960, pp. 103-109.
5. Hill, P. G. and Peterson, C. R., Mechanics and Thermodynamics of Propulsion, Addison Wesley, 1970, pp. 418-422.
6. Geisler, R. L., Kinkead, S. A., and Beckman, C. W., "The Relationship Between Solid Propellant Formulation Variables and Motor Performance", AIAA Paper 75-1199, Oct. 1975.
7. 1977 JANNAF Aluminum Combustion Workshop, 10-11 May, 1977, Magna, Utah.
8. JANNAF Workshop on "Combustion Efficiency of Highly Aluminized Solid Propellants", Sept. 1980.
9. George, D., "Recent Advances in Solid Rockets Motor Performance Prediction Capability", AIAA Paper No. 81-0033, AIAA 19th Aerospace Sciences Meeting, 12-15 January 1981, St. Louis, MO.
10. Hermsen, R. W., "Aluminum Oxide Particle Size for Solid Rocket Motor Performance Prediction", AIAA-81-0035, AIAA 19th Aerospace Sciences Meeting, 12-15 January 1981.
11. Cashdollar, K. L., Lee, C. K., and Singer, J. M., "Smoke Particle Size and Concentration Measurements by a Three Wavelength Light Transmission Technique", presented at Hartford Meeting, Eastern Section/Combustion

Institute, November 10, 1977.

12. Hewett, M. E. and Netzer, D. W., "Application of Light Extinction Measurements to the Study of Combustion in Solid Fuel Ramjets", NPS Report, NPS 67-78-008, Nov. 1978.
13. Schryer, D. R., "Investigation of Light Scattering as a Technique for Detecting Discrete Soot Particles in a Luminous Flame", NASA Tech. paper 1235, July 1978.
14. Weber, F. N., "Laser Doppler Spectrometer Method of Particle Sizing", NASA Cr-146064, January 1976.
15. Holve, D. and Self, S. A., "An Optical Particle-Sizing Counter for In-Situ Measurements", Project Squid TR-SU-2-PU, January 1978.
16. Willoughby, P. G., Baker, K. K., and Hermsen, R. W., "Photographic Study of Solid Propellants Burning in an Acceleration Environment", UTC Contractor Report, NASA CR-66824, Oct. 21, 1969.
17. Abraham, M., Klahr, O. A., Gerhardt, R. R., and Netzer, D. W., "An Investigation of Solid Propellant Combustion in Standard and High Acceleration Environments", NPS report NPS 57Nt-74031, March 1974.
18. Gany, A., Caveny, L. H., and Summerfield, M., "Aluminized Solid Propellants Burning in a Rocket Motor Flow Field", AIAA J., Vol. 16, No. 7, July 1978, pp. 736-739.
19. Caveny, L. H., and Gany, A., "Breakup of Al/Al<sub>2</sub>O<sub>3</sub> Agglomerates in Accelerating Flow Fields", AIAA paper 79-0300, presented at 17th Aerospace Sciences Meeting, New Orleans, LA., Jan 15-17, 1979.
20. Briones, R. A., and Wuerker, R. F., "Application of Holography to the Combustion Characterization of Solid Rocket Propellants", AFRLP report AFRLP-TR-77-90, April 1978.
21. Briones, R. A., and Wuerker, R. F., "Holography of Solid Propellant

- Combustion", Experimental Diagnostics in Combustion of Solids, AIAA, Progress in Astronautics and Aeronautics, 1978, Vol. 63, pp. 251-276.
22. Boggs, T. L., et al, "Cinephotomicrography and Scanning Electron Microscopy as Used to Study Solid Propellant Combustion at the Naval Weapons Center", NWC TP 5944, May 1977.
  23. Bumprecht, R. O. and Sliepeevich, C.M., "Scattering of Light by Large Spherical Particles", Journal of Phys. Chem. No. 57, 1953.
  24. Chin, J. H., Sliepeevich, C. M. and Tribus, M., "Particle Size Distribution in Polydispersed Systems by Means of Measurements of Angular Variation of Intensity of Forward-Scattered Light at Very Small Angles", Journal of Phys. Chem., No. 59, 1955.
  25. Dobbins, R. A., Crocco, L. and Glassman, I., "Measurement of Mean Particle Sizes of Sprays from Diffractively Scattered Light", AIAA Journal, Vol. 1, No. 8, 1963.
  26. Muggels, R. A. and Evans, H. D., "Droplet Size Distribution in Sprays", Ind. Eng. Chem., 43, 1951.
  27. Roberts, J. H. and Webb, M. J., "Measurements of Droplet Size for Wide Range Particle Distributions", AIAA Journal, Vol. 2, No. 3, 1964.
  28. Dobbins, R. A. and Jizmagian, G. S., "Optical Scattering Cross Sections for Polydispersions of Dielectric Spheres", Journal of the Optical Society of America, Vol. 56, No. 10, 1966.
  29. Dobbins, R. A. and Jizmagian, G. S., "Particle Size Measurements Based on Use of mean Scattering Cross Sections", Journal of the Optical Society of America, Vol. 56, No. 10, 1966.
  30. Hodkinson, J. R., "Particle Sizing by Means of the Forward Scattering Lobe", Applied Optics, Vol. 5, 1966.
  31. Nejad, A. S., Schetz, J. A. and Jakubowski, A. K., "Mean Droplet Diameter

Resulting from Atomization of a Transverse Liquid Jet in a Supersonic Air Stream", AFOSR-TR-79-0004, November 1978.

32. Powell, E. A., Cassanova, R. A., Bandston, C. P. and Zinn, B. I., "Combustion Generated Smoke Diagnostics by Means of Optical Measurement Techniques", AIAA 14th Aerospace Sciences Meeting, January 1976, AIAA Paper No. 67-76.
33. Thompson, B.J., et al, "Application of Hologram Techniques for Particle Size Analysis", Applied Optics, Vol. 6, No. 3, March 1967.
34. Gumprecht, R. O. and Sliepeevich, C. M., "Scattering of Light by Large Spherical Particles", J. of Phys. Chem. No. 57, 1953.
35. Klein, N. and Dweilde, M. A., "Pulsed Holography for Combustion Diagnostics", CPIA Publication 329, November 1980.
36. Briones, R. A. and Wuerker, R. F., "Instruction Manual for the Improved Ruby Laser Holographic Illuminator", AFRPL-TM-78-11, July 1978.
37. Wuerker, R. F. and Briones, R. A., "Operation Manual for Lens-Assisted Multipulse Holocamera with Reflected Light Option", AFRPL-TM-78-12, July 1978.
38. Kraeutle, K. J., "Applications of Particle Size Analysis in Combustion Research," AIAA Paper 77-978, July 1977, American Institute of Aeronautics and Astronautics, New York, N.Y.
39. Ditore, M. J., Poynter, R., and Schmidt, W., "Zirconium/Aluminum Combustion," Aerojet Solid Propulsion Company, R & D Status Report LBA-MPR-18, April 1980.

TABLE I  
PROPELLANT COMPOSITIONS

Propellant Designation	Binder % Weight	Oxidizer % Weight	Metal % Weight	Mean Metal Diameter, $\mu\text{m}$
WGS-5A	HTPB 12	AP 83	Al 5	75-88
WGS-6A	HTPB 12	AP 83	Al 5	45-62
WGS-7A	HTPB 12	AP 83	Al 5	23-27
WGS-7	HTPB 12	AP 83	Al 5	7-8
NWC-1 <sup>1</sup>	HTPB 12	AP 87	Al <sub>2</sub> O <sub>3</sub> 1.0	8
NWC-2 <sup>1</sup>	HTPB 12	AP 87.5	Al <sub>2</sub> O <sub>3</sub> 0.5	8
N-7	PBAN 18	AP 67.0	Al 15	44

Note:  
1. Approximate formulation

TABLE II  
PARTICLE COLLECTION TEST CONDITIONS

Test Number	Propellant Type	Pressure PSI
1445240480	WGS-5A	500
1515280380	WGS-5A	500
1500250180	WGS-5A	500
1445180480	WGS-5A	1000
1030030580	WGS-6A	500
1600170480	WGS-6A	1000
1215030580	WGS-7A	500
1400240480	WGS-7A	1000
1100030580	WGS-7	500
1500210480	WGS-7	1000
1230010580	NWC-1	500
1520090480	NWC-1	500
150010580	NWC-1	1000
1200110580	NWC-2	500
1615100580	NWC-2	1000

**TABLE III**  
**HIGH SPEED MOTION PICTURE TEST CONDITIONS**

Test Number	Propellant Type	Pressure PSI	Film Type	f/STOP	EXTERNAL LIGHT
1545050480	WGS-5A	500	EKTACHROME 7250	4.0	650 W SIDE
1600260480	WGS-5A	500	KODACHROME 25	1.9	1200 W SIDE 650 W BACK
1500300480	WGS-5A	1000	KODACHROME 25	1.9	1200 W SIDE 650 W BACK
1415010580	WGS-6A	500	KODACHROME 25	1.9	1200 W SIDE 650 W BACK
1415250580	WGS-6A	500	KODACHROME 25	1.9	1200 W SIDE 650 W BACK
1315010580	WGS-6A	1000	KODACHROME 25	1.9	1200 W SIDE 650 W BACK
1100250580	WGS-6A	1000	KODACHROME 25	1.9	1200 W SIDE 650 W BACK
1300250580	WGS-7A	500	EKTACHROME 7250	5.6	1200 W SIDE 650 W BACK
1700300480	WGS-7A	1000	KODACHROME 25	1.9	1200 W SIDE 650 W BACK
1345250580	WGS-7	500	KODACHROME 25	1.9	1200 W SIDE 650 W BACK

TABLE III  
(continued)

Test Number	Propellant Type	Pressure PSI	Film Type	f/STOP	INTERNAL LIGHT
1615300480	WGS-7	1000	KODACHROME 25	1.9	1200 W SIDE 650 W BACK
1500250580	NWC-1	500	KODACHROME 25	1.9	1200 W SIDE 650 W BACK
1145250580	NWC-1	1000	KODACHROME 25	1.9	1200 W SIDE 650 W BACK
1530250580	NWC-2	500	KODACHROME 25	1.9	1200 W SIDE 650 W BACK
1215250580	NWC-2	1000	KODACHROME 25	1.9	1200 W SIDE 650 W BACK

**Note:**

1. The Frame rate for all tests was 5000 pictures per second.

**TABLE IV**  
**RESOLUTION TARGET TEST CONDITIONS**

TEST NUMBER	FILM TYPE	WINDOW IN PLACE	PICTURES PER SEC	F/STOP	EXTERNAL LIGHT
1630250580	KODACHROME 25	NO	50-250	1.9	650 WATT BACK LIGHT
1645250580	KODACHROME 25	YES	50-250	1.9	650 WATT BACK LIGHT
1745030480	EKTACHROME 7250	NO	50-250	4	650 WATT BACK LIGHT
1700250580	EKTACHROME 7250	YES	50-250	4	650 WATT BACK LIGHT
1630310580	4X 7224	NO	50-250	5.6	650 WATT BACK LIGHT
1530310580	4X 7224	YES	50-250	5.6	650 WATT BACK LIGHT
1515310580	2X 7222	NO	50-250	4	650 WATT BACK LIGHT
1615310580	2X 7222	YES	50-250	4	650 WATT BACK LIGHT
MODIFIED BOMB AND CAMERA	EKTACHROME 7239	YES	50-250	1.9	650 WATT BACK LIGHT

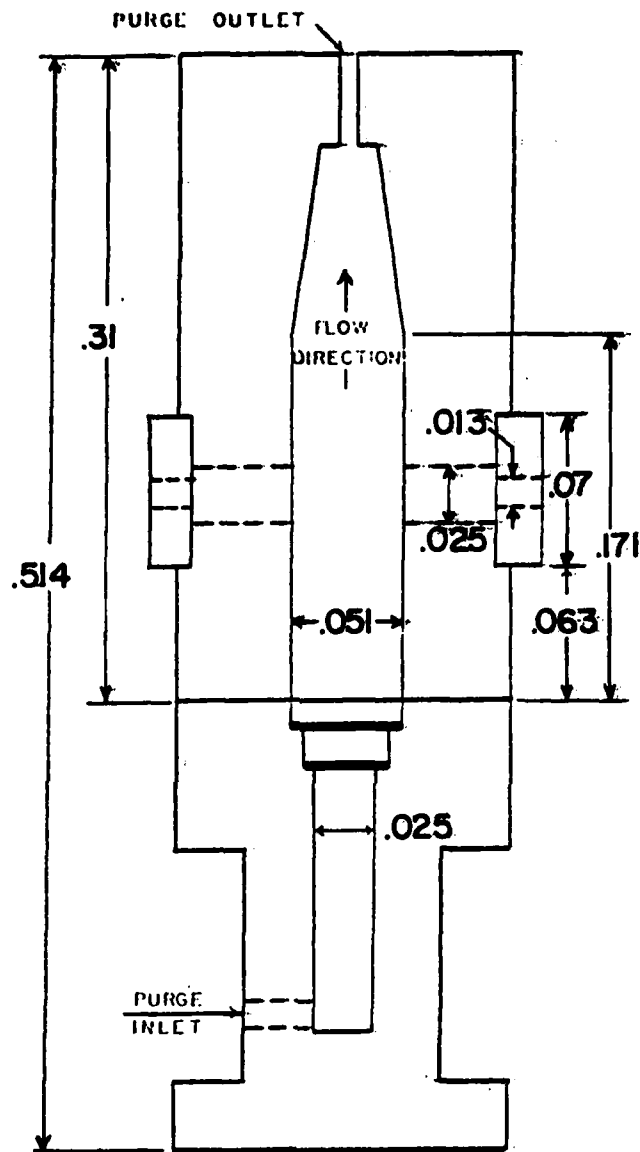
**TABLE V**  
**BURNING RATE EXPONENTS**

<b>PROPELLANT TYPE</b>	<b>BURNING RATE EXPONENT</b>
<b>WGS-5A</b>	<b>0.301</b>
<b>WGS-6A</b>	<b>0.273</b>
<b>WGS-7A</b>	<b>0.275</b>
<b>WGS-7</b>	<b>0.272</b>
<b>NWC-7</b>	<b>0.247</b>
<b>NWC-2</b>	<b>0.299</b>

TABLE VI  
 VOLUME-SURFACE MEAN DIAMETER ( $D_{32}$ ) MEASUREMENT RESULTS

DISTANCE FROM OPTICAL C.L. (cm)		FWD ANGLE		OUTPUT VOLTAGE (mv)		$I(\theta)$	$\bar{\theta}$		$D_{32}$
ON CHART	TRUE	$\theta$ (rad)	$\theta$ (rad)	COLD	HOT		Universal 1-37 $\mu$ Curve	Universal 1-37 $\mu$ Cal.	
0	0	0	0	163.9	183.1	1.00	0	0	-
1.09	.59	.012	.012	132.8	138.6	.30	1.82	1.08	18.1
1.78	.96	.019	.019	36.5	40.3	.20	2.08	1.25	13.3
2.13	1.15	.023	.023	17.3	20.3	.16	2.25	1.35	11.8
2.57	1.38	.028	.028	7.7	9.0	.07	2.83	1.63	11.7
2.92	1.57	.031	.031	3.5	4.8	.07	2.83	1.63	10.5

$$D_{32} = \frac{\lambda \bar{\theta}}{\pi \theta} = .201 \frac{\bar{\theta}}{\theta}$$



DIMENSIONS: meters

Figure 1.  
Schematic of Combustion Bomb

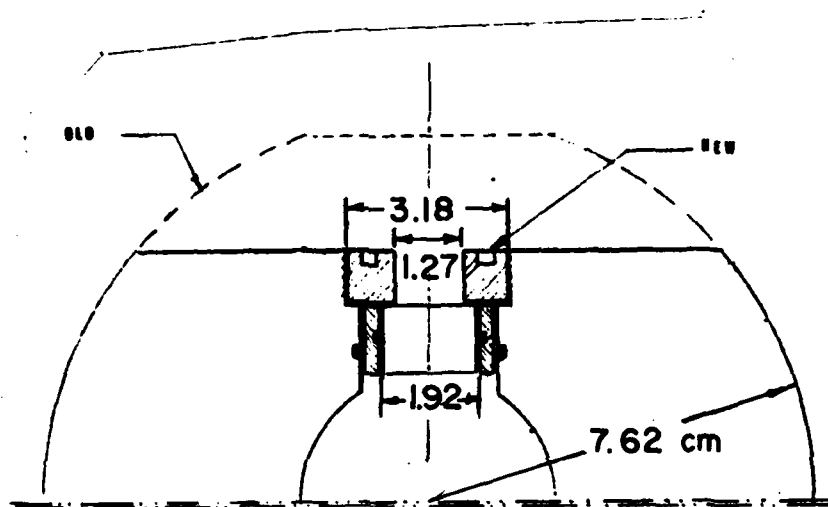


Fig. 2. Schematic of Combustion Bomb Modification

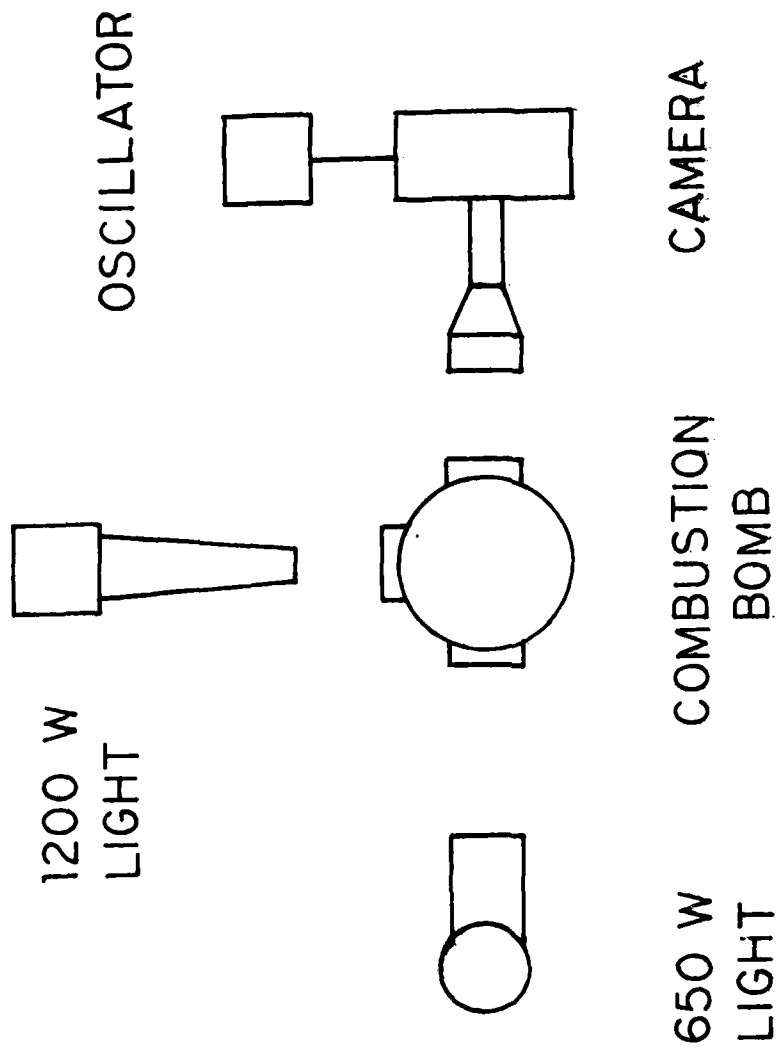


Fig. 3. Schematic of Experimental Apparatus - Combustion Bomb

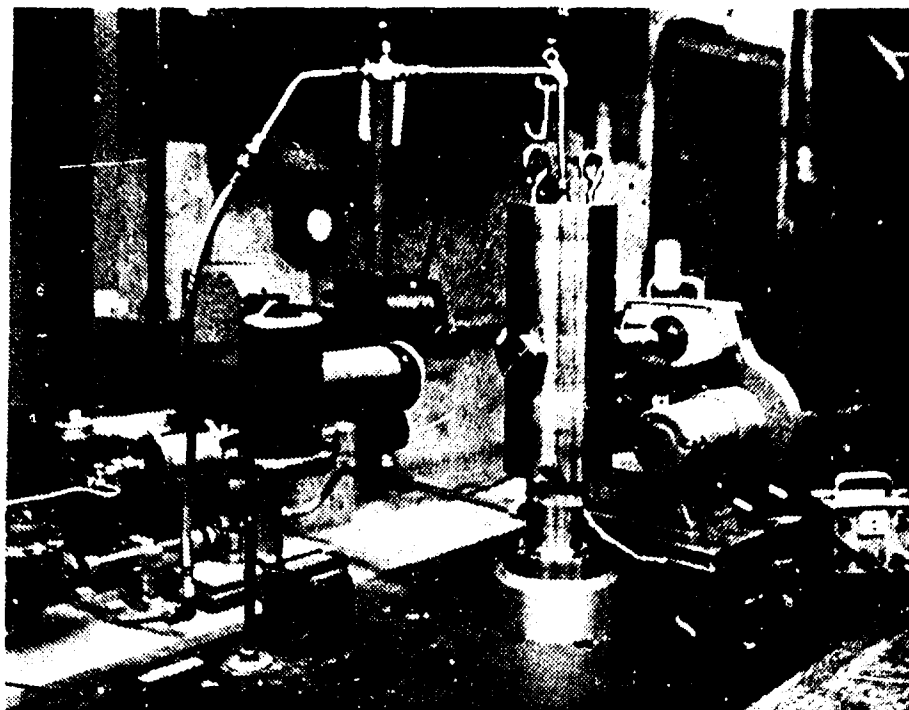
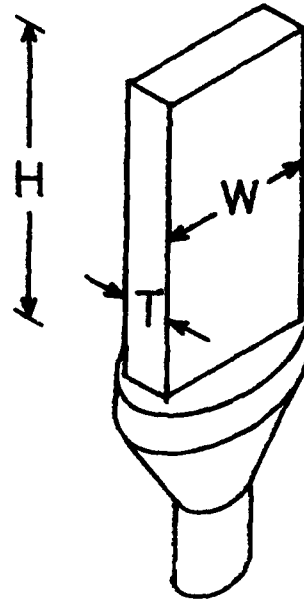


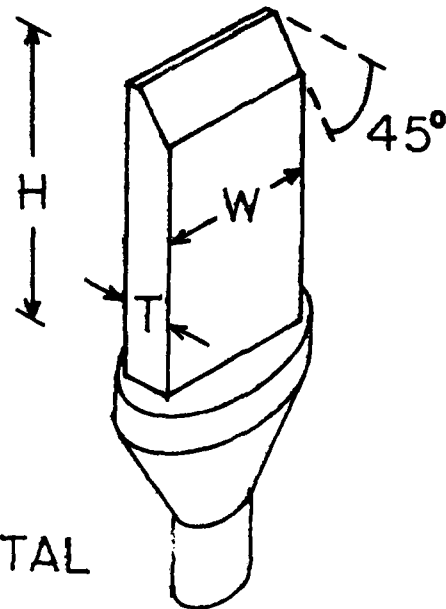
FIGURE 4    Photograph of Experimental  
Apparatus - Combustion Bomb

FLAT TOP

H = 10 mm  
W = 7 mm  
T = 2 mm



SLANT TOP

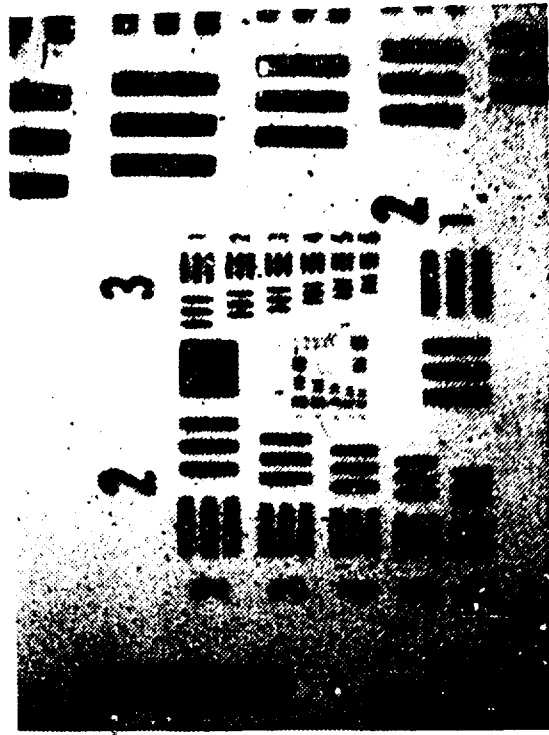


PEDESTAL

Fig. 5. Propellant Strand Dimensions



a. Initial Study



b. Modified Combustion Bomb

Fig. 6. Photographs of 1951 USAF Resolution Target

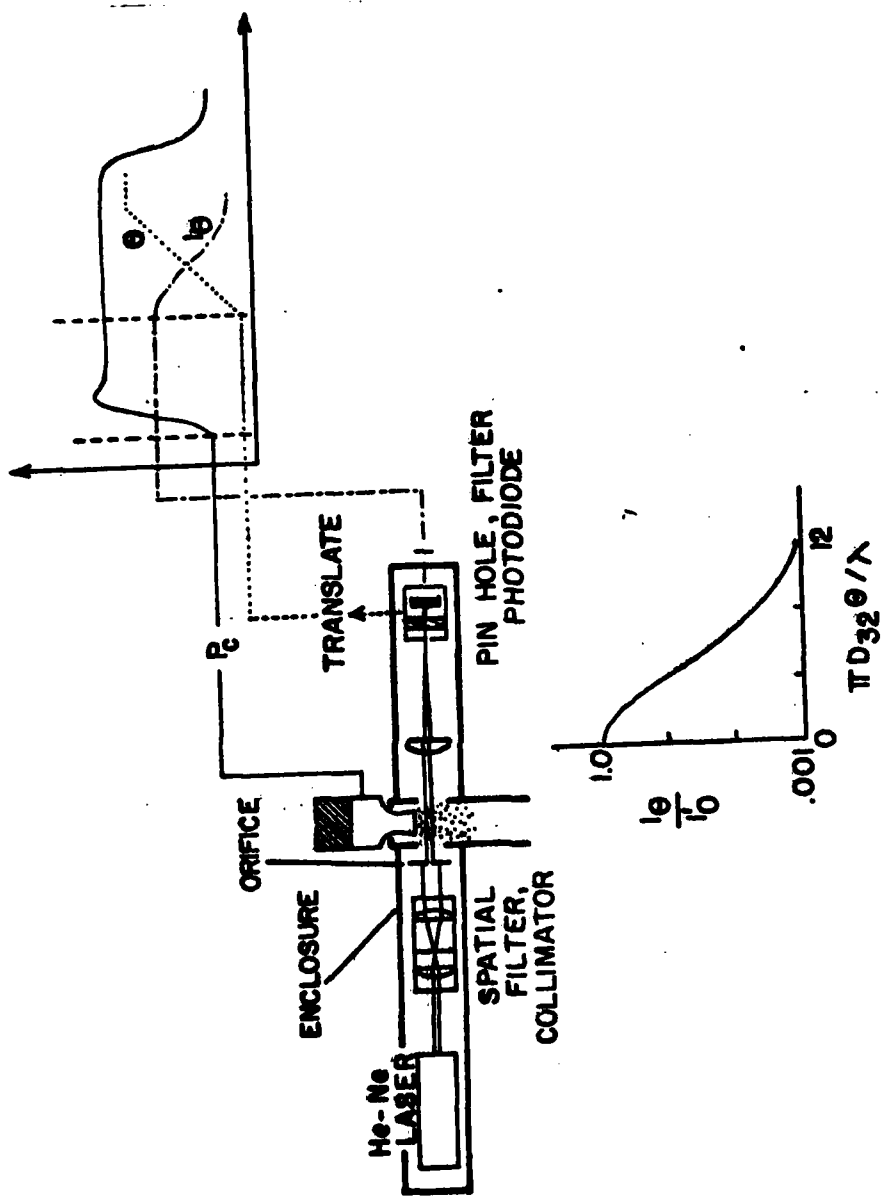


Fig. 7. Schematic Diagram of Diffractively Scattered Light Apparatus

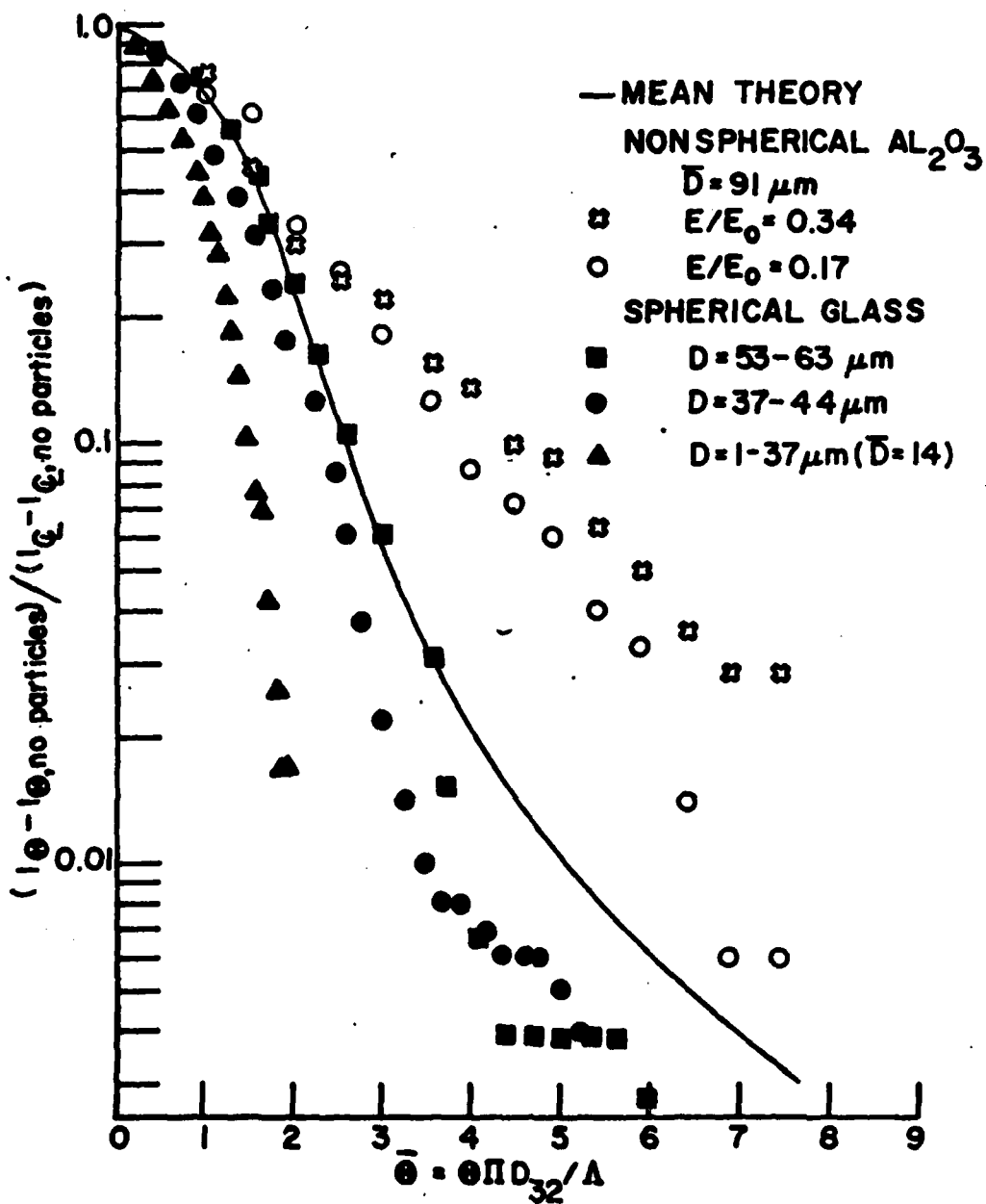


Fig. 8. Nondimensionalized Illumination Profiles [I(θ) versus θ̄]

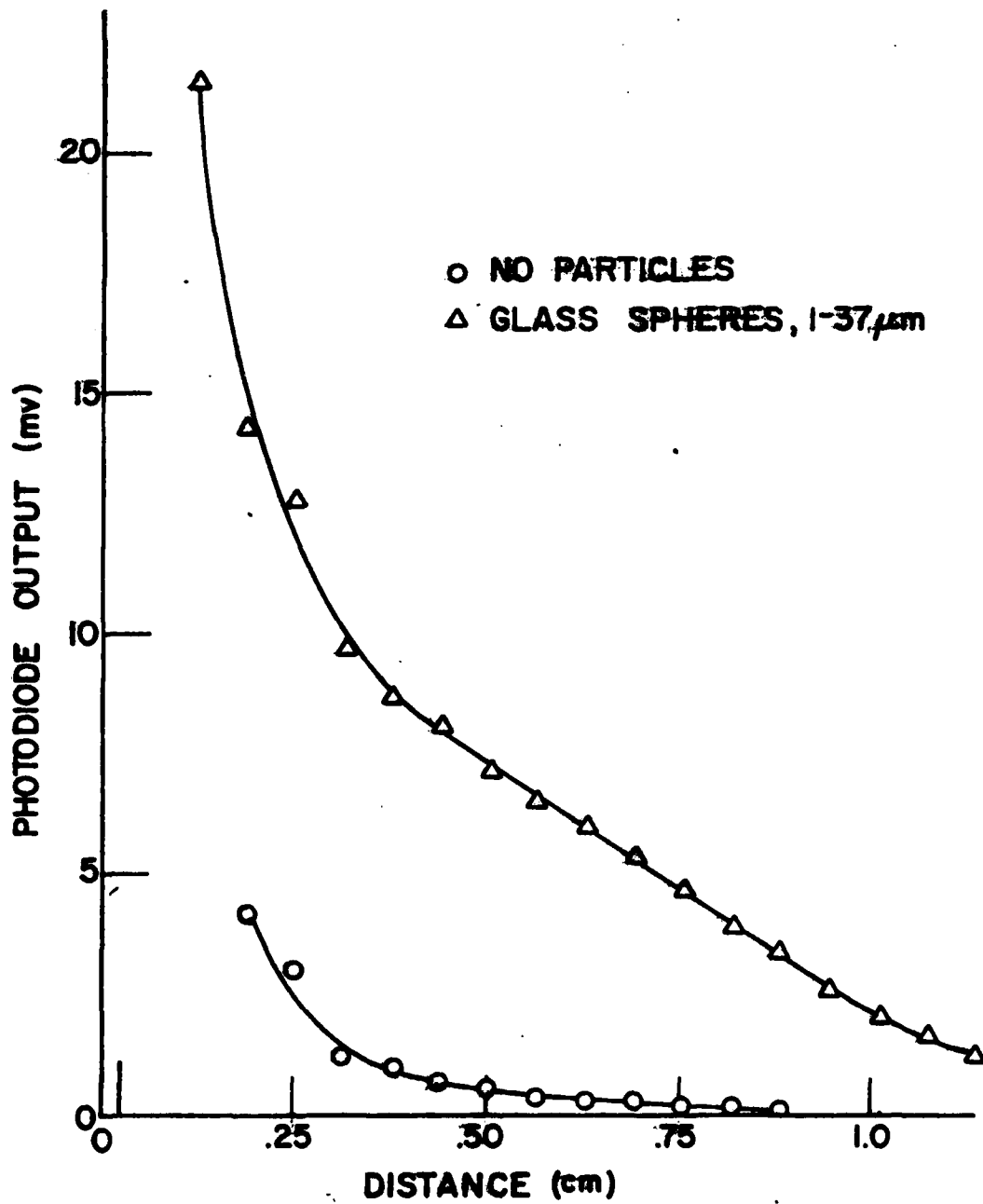
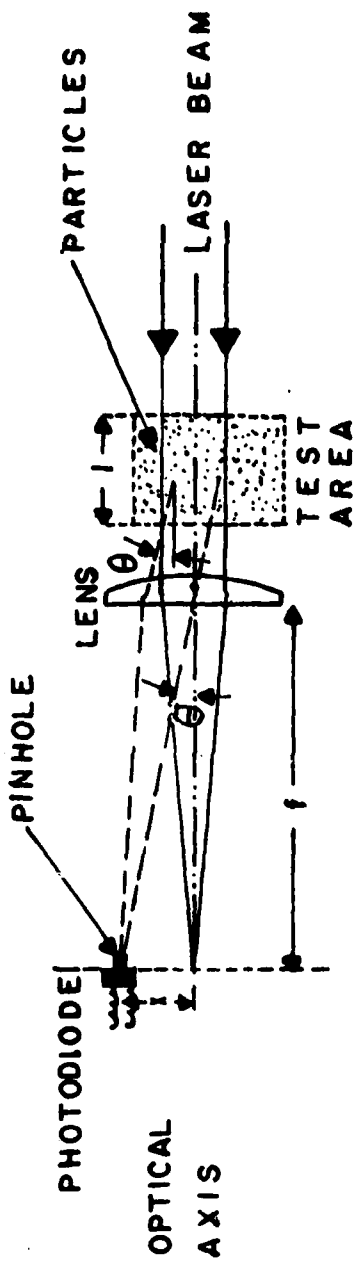


Fig. 9. Photodiode Output Voltage versus Distance from Centerline for Glass Beads



For air:  $\theta \approx \frac{x}{f}$

For water:  $\theta \approx \frac{x}{f \times 1.35}$ , where 1.35 is the refractive index of water [Ref. 34]

Fig. 10. Light Scattering Geometry

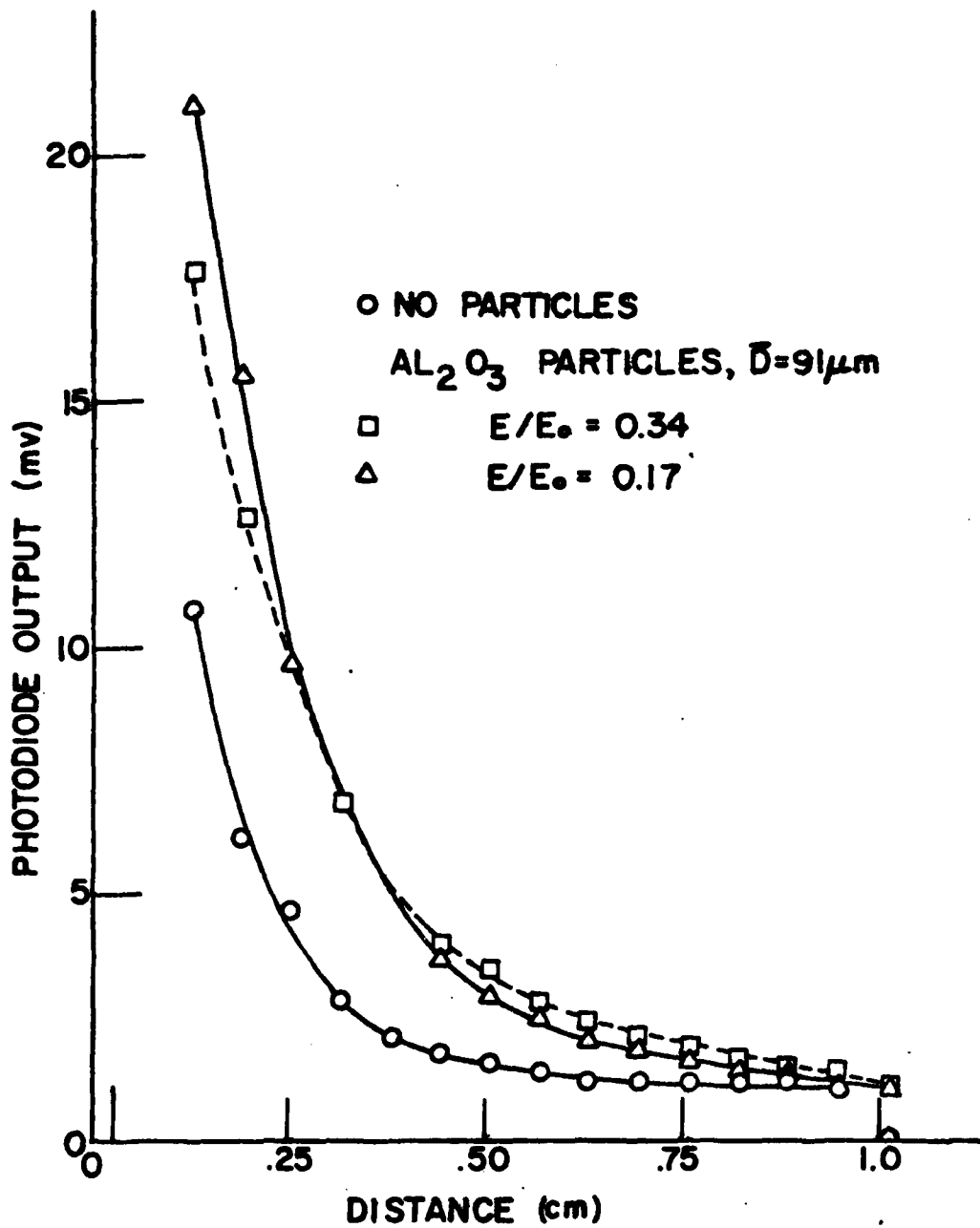


Fig. 11. Photodiode Output Voltage versus Distance from Centerline for Al<sub>2</sub>O<sub>3</sub> Particles

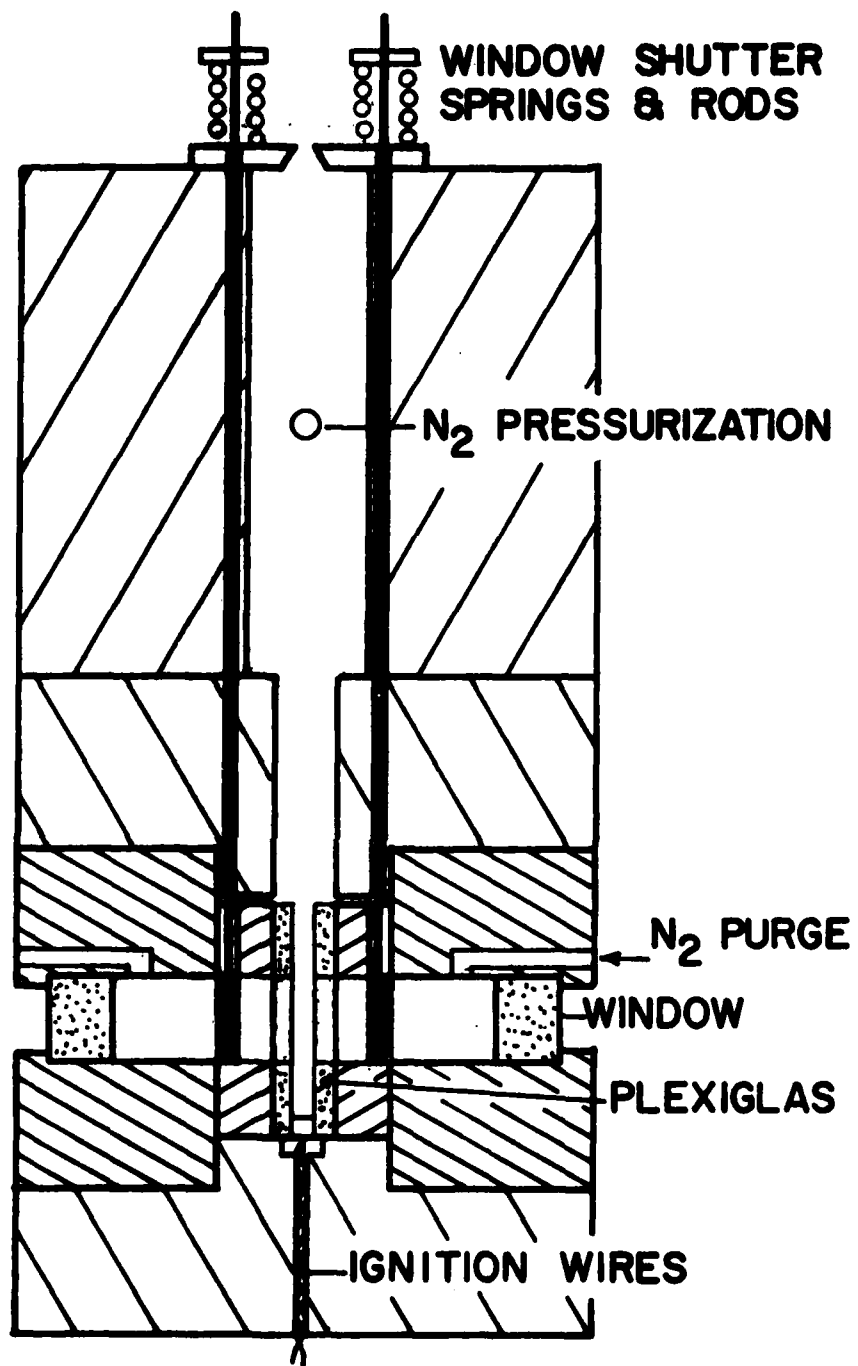


Figure 12 Motor Line Drawing, Side View

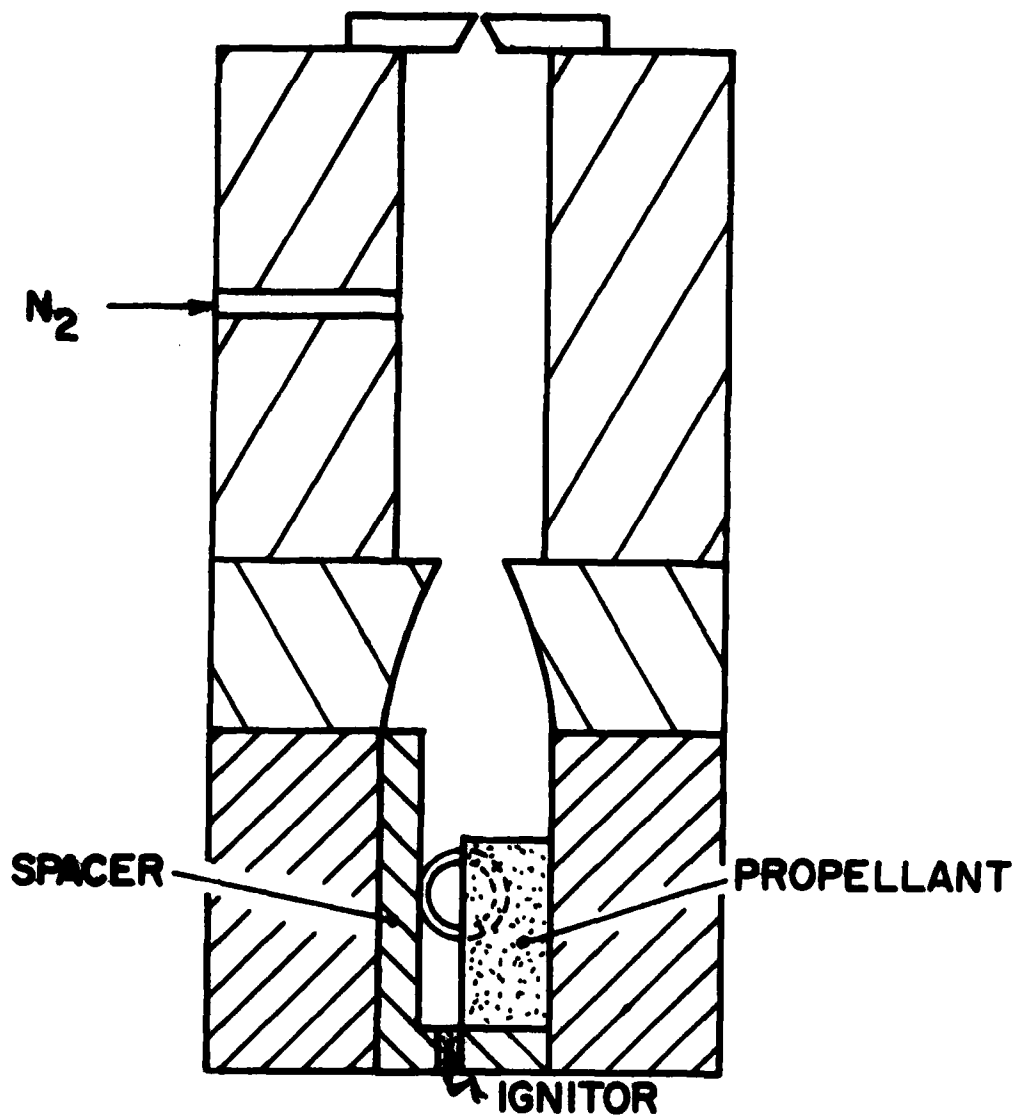


Figure 13 Motor Line Drawing, Window Side View

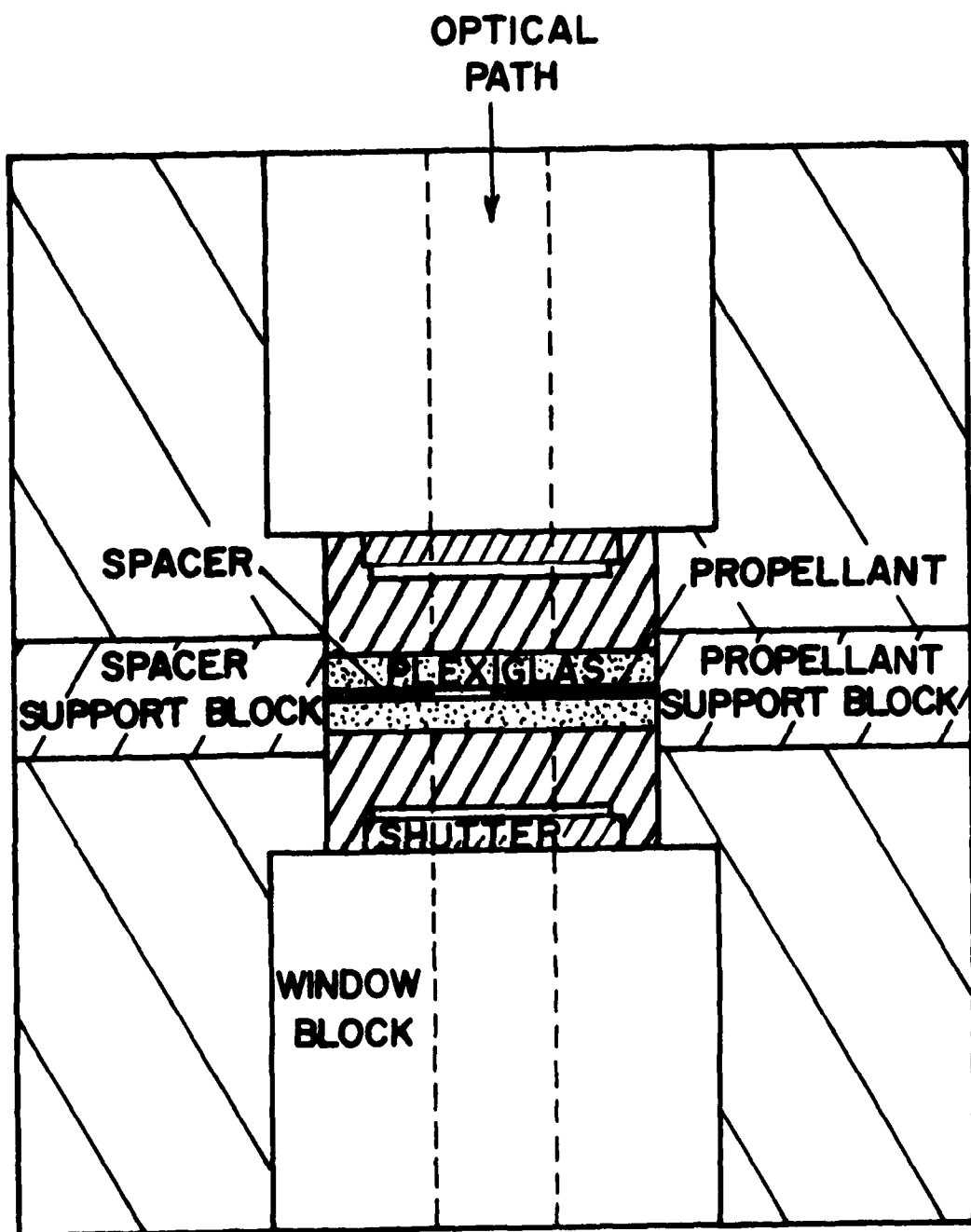


Figure 14 Plexiglas Spacer Arrangement

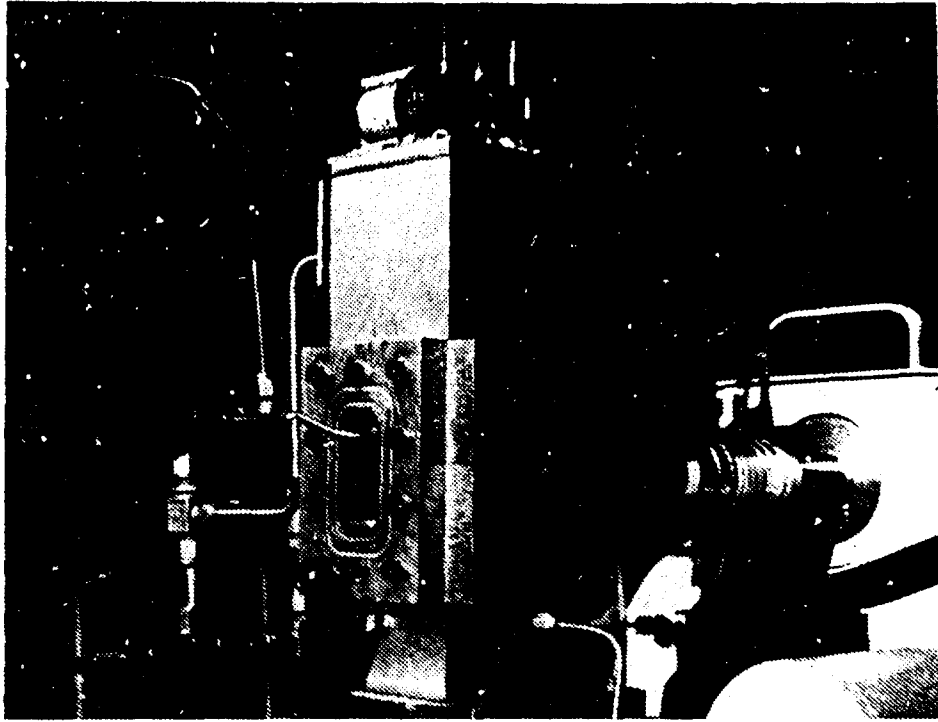


Figure 15 High Speed Motion Picture Apparatus

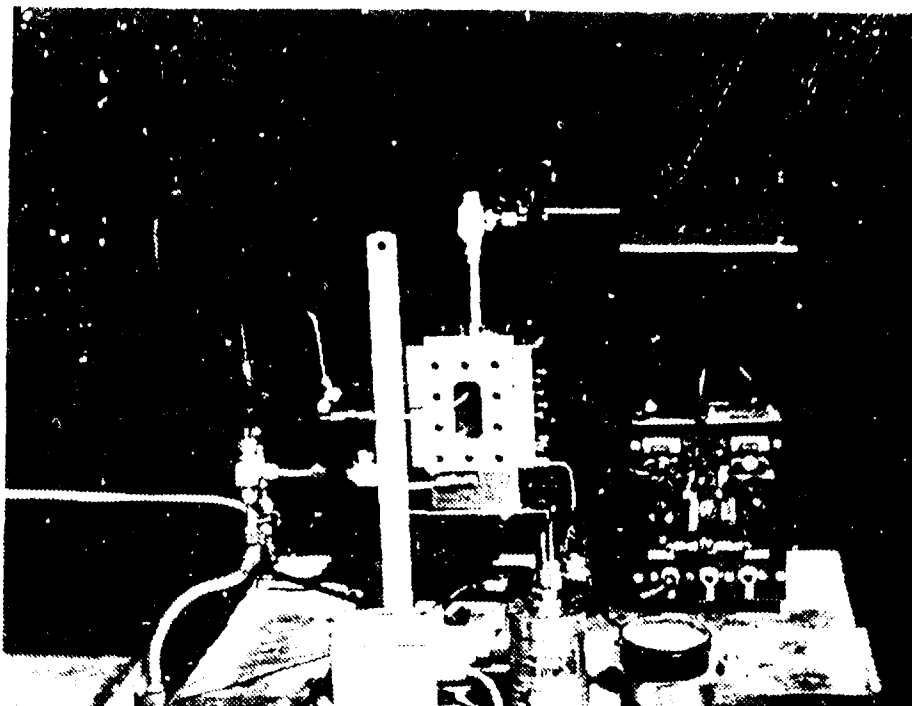


Fig. 16 Photograph of 2-D Motor with Control Box and Hologcamera

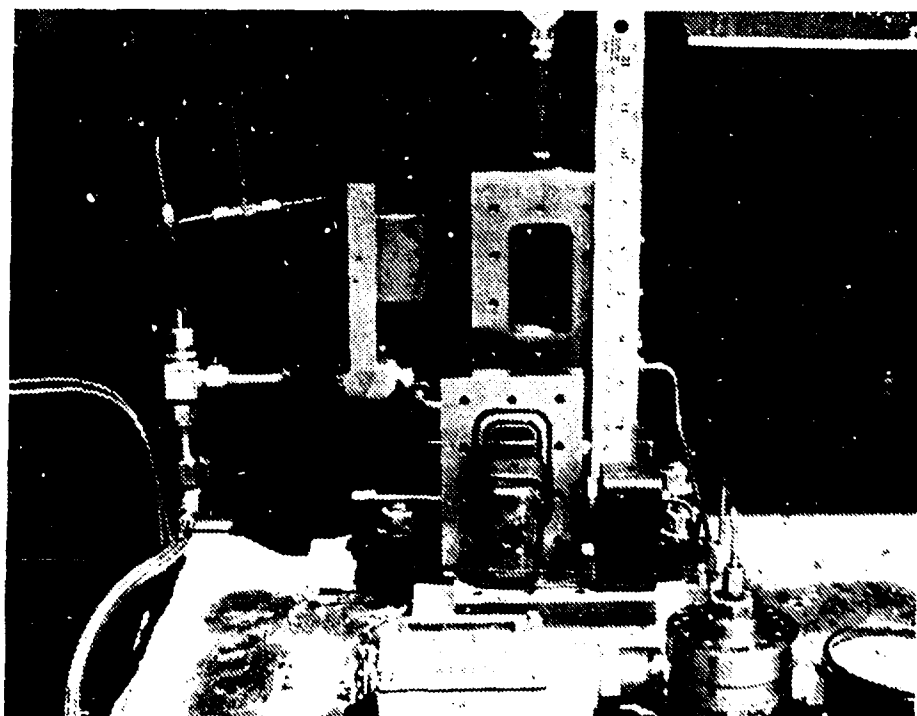


Fig. 17 Photograph of 2-D Motor Components

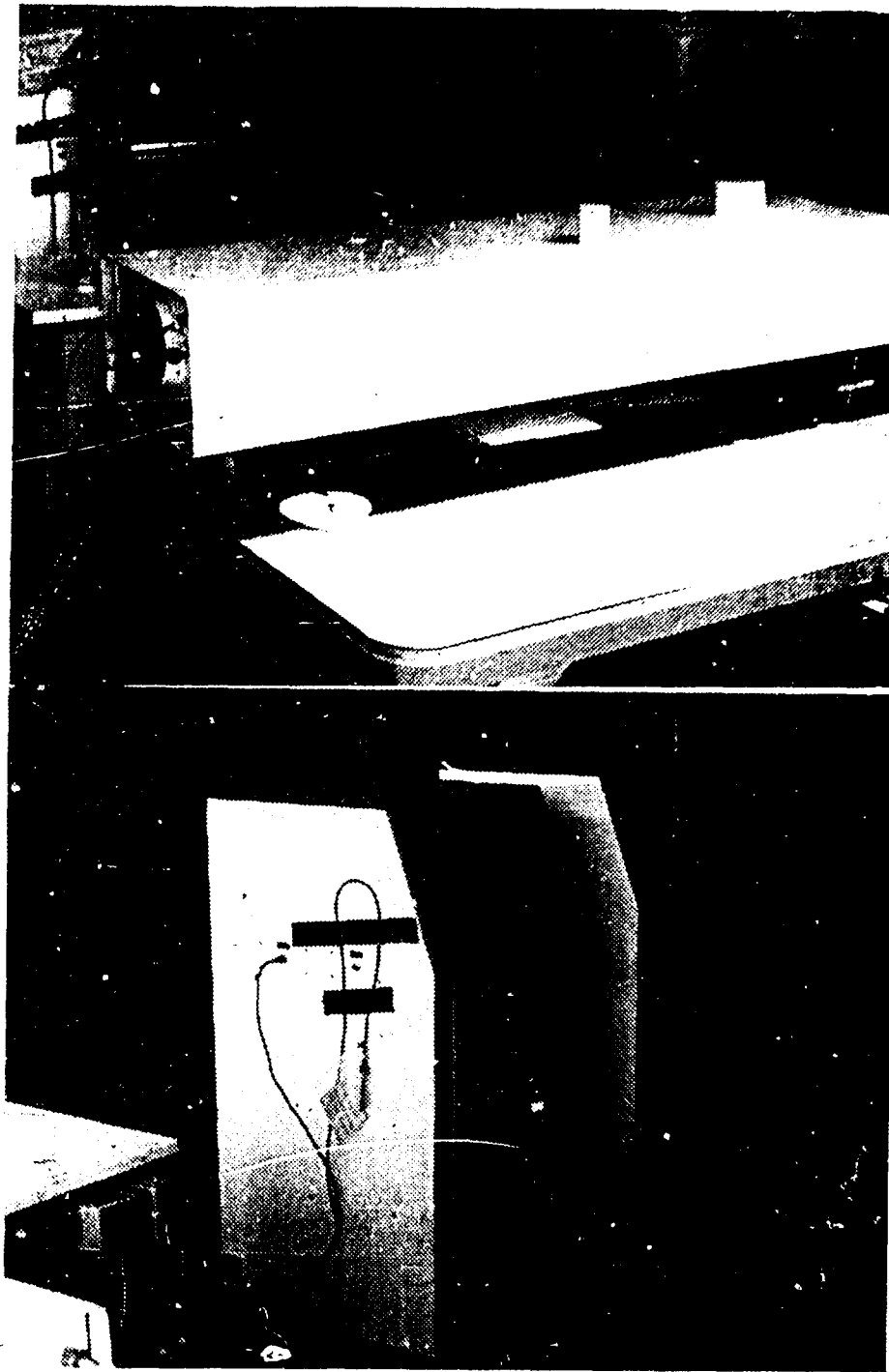


Fig. 18 Photographs of RPL Ruby Laser Components

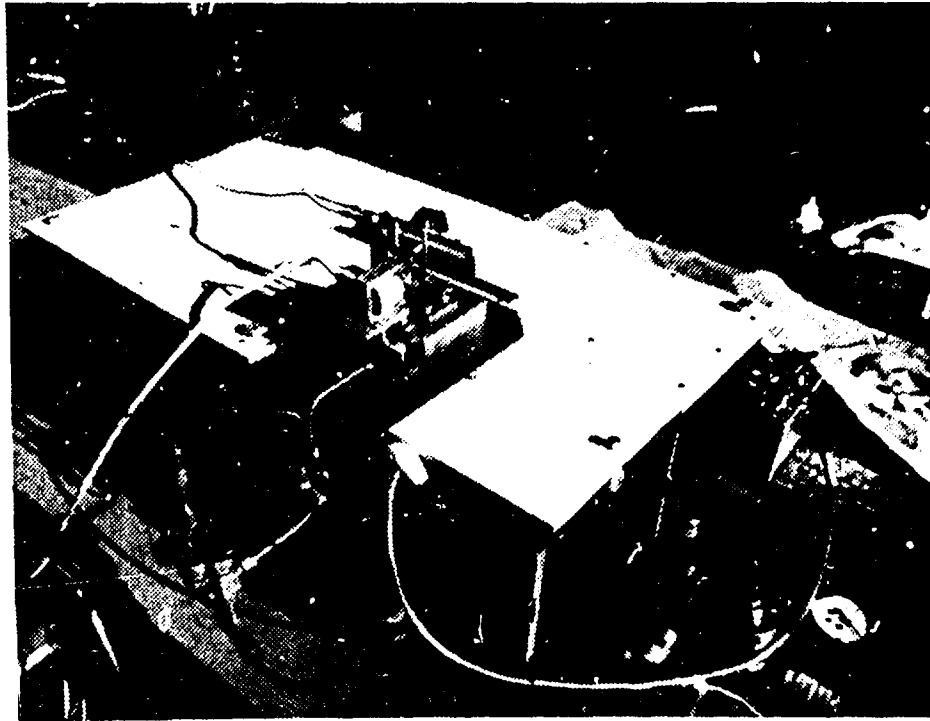


Figure 19 Lens Assisted Holographic System

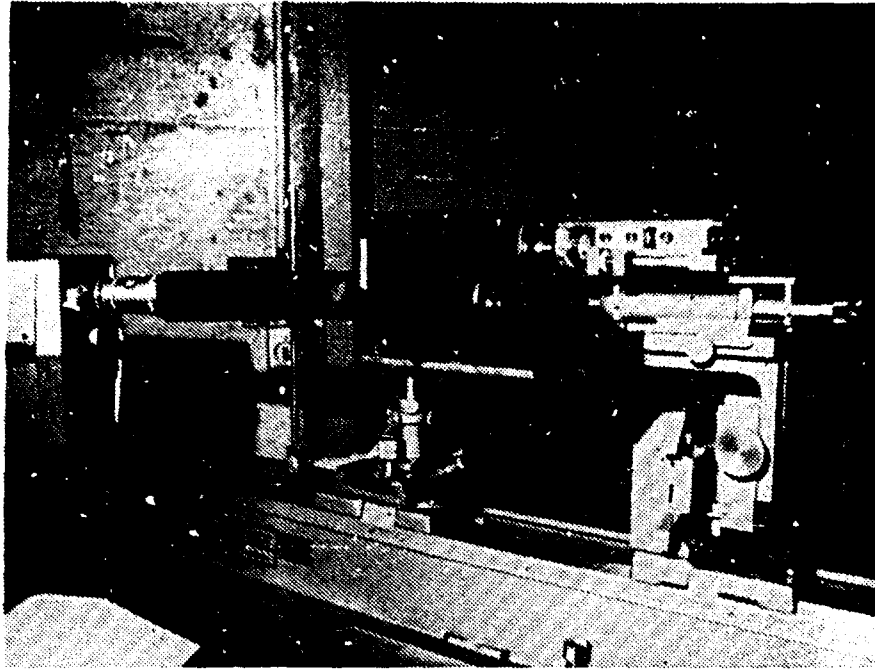


Figure 20 Holographic Reconstruction Apparatus



Fig. 21 Hologram of 1951 USAF Resolution Target

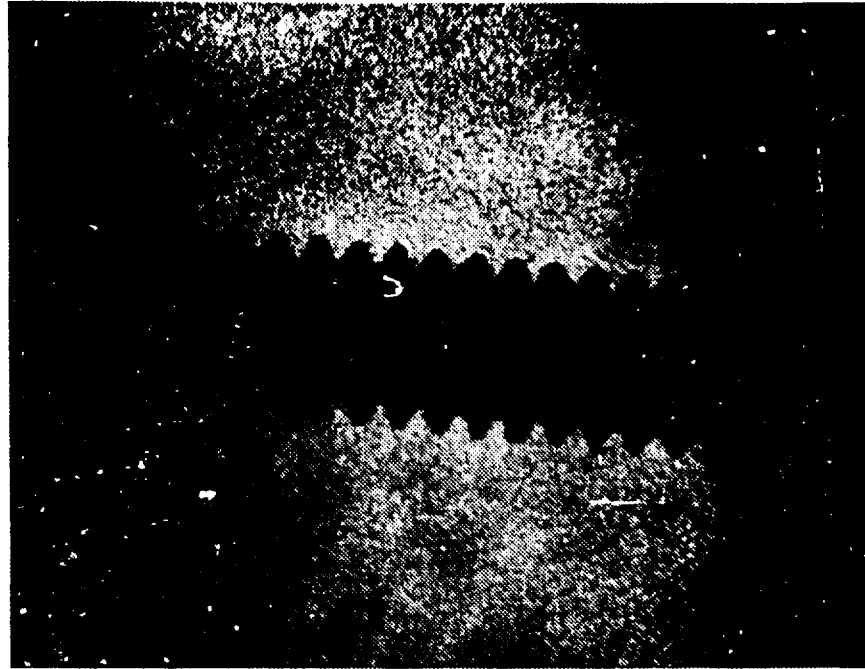
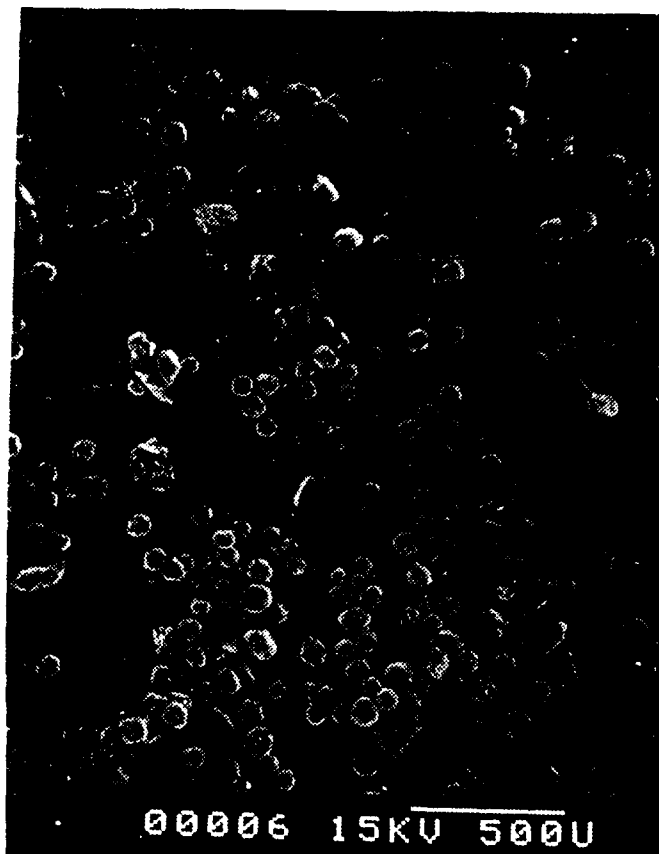
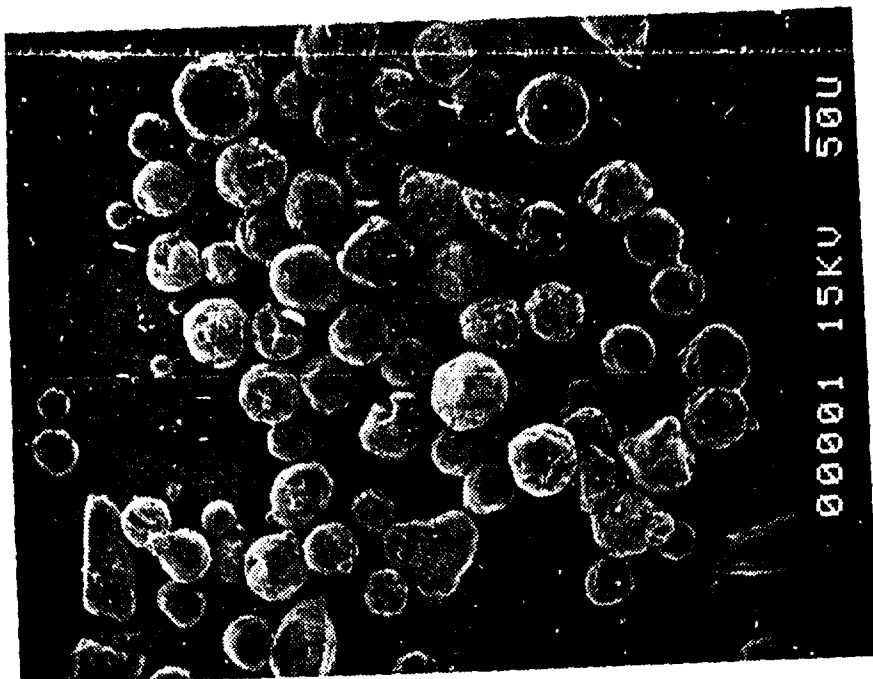


Fig. 22. Photograph of Reconstructed Hologram of 0-80 screw used for Particle sizing.

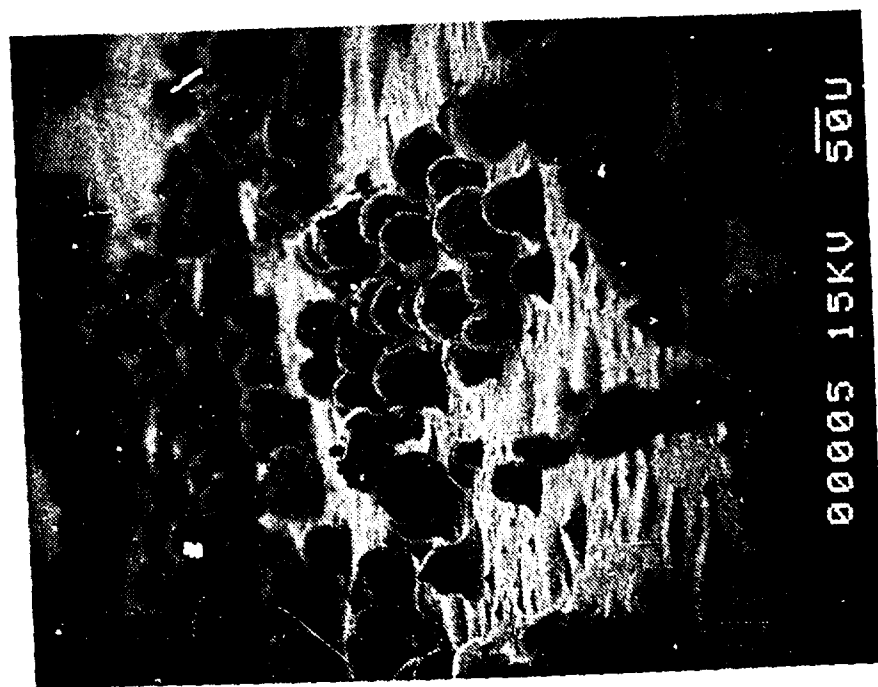


(a)

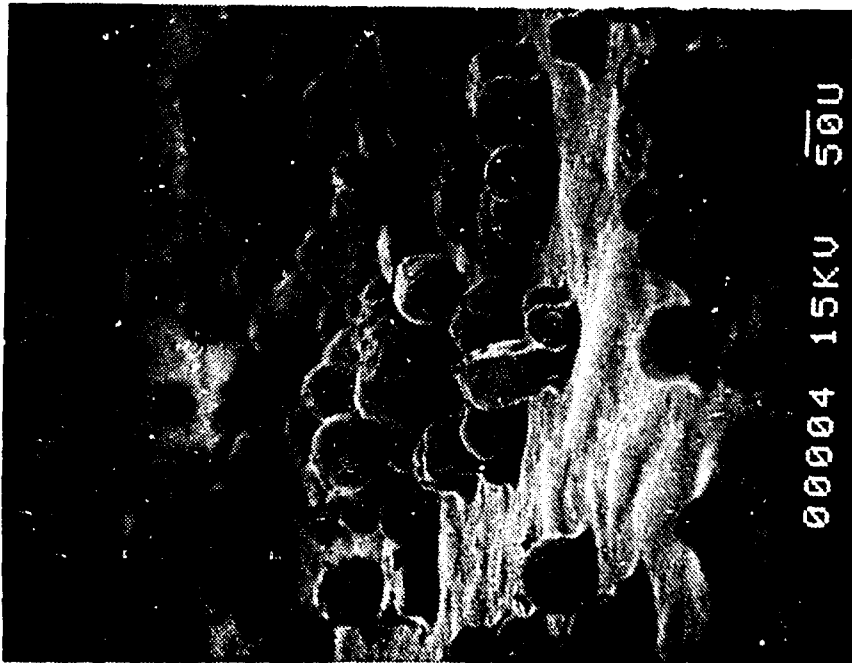
FIGURE 23 Photomicrographs of Postfire Residue  
(1445240480, WGS-5A,  $P_c = 34$  atm. )



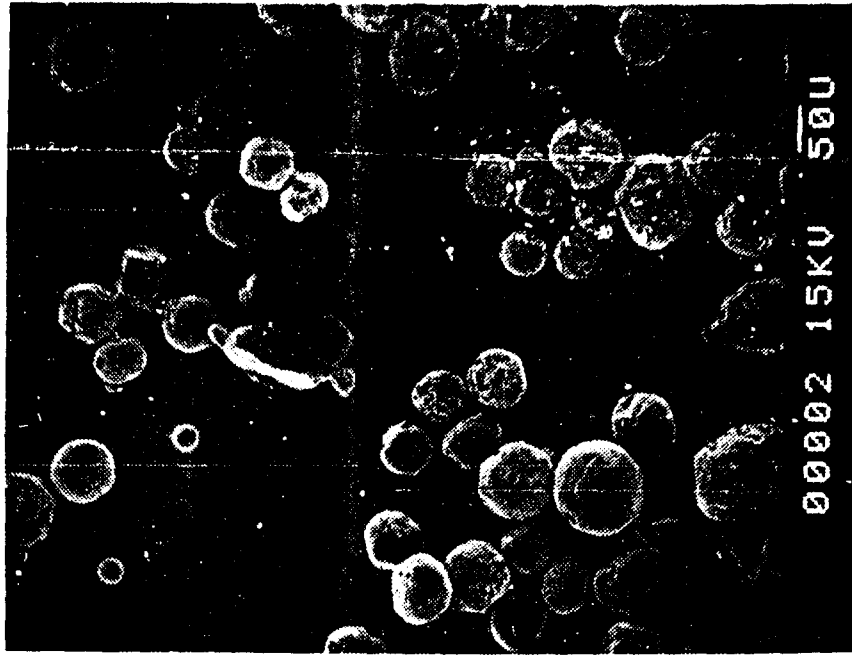
(e)



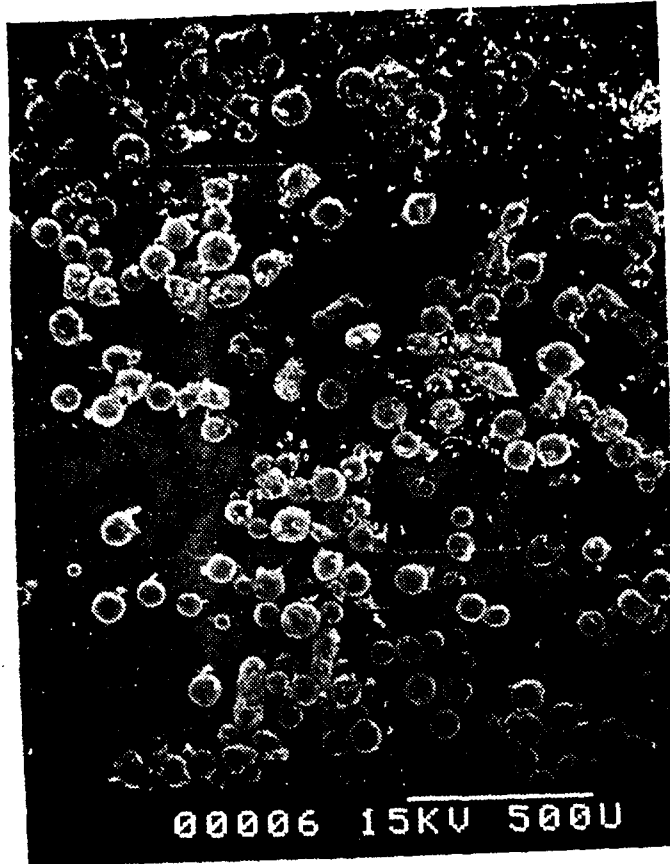
(b)



(a)



(e)

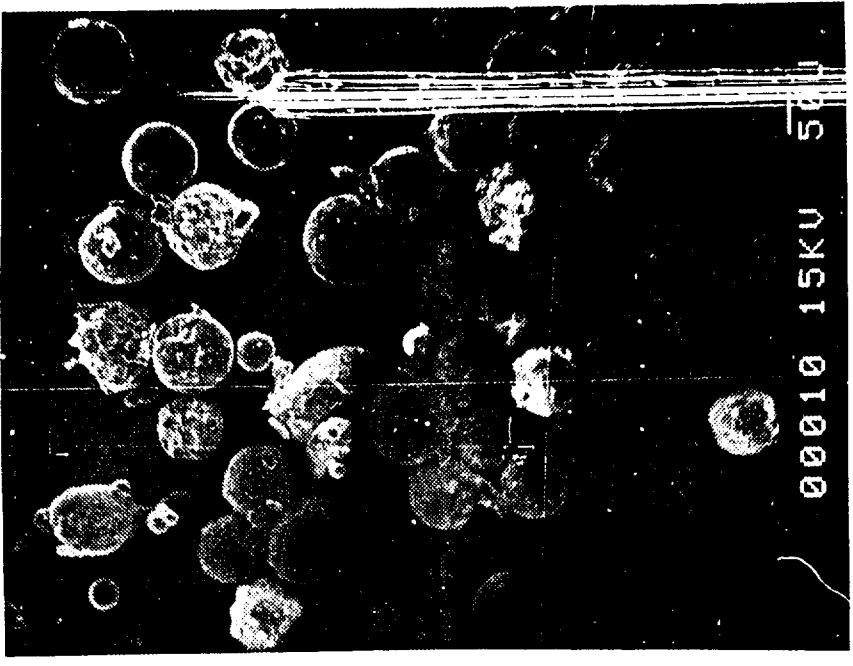


(a)

FIGURE 24 Photomicrographs of Postfire Residue  
(1445180480, WGS-5A,  $P_c = 68$  atm. )



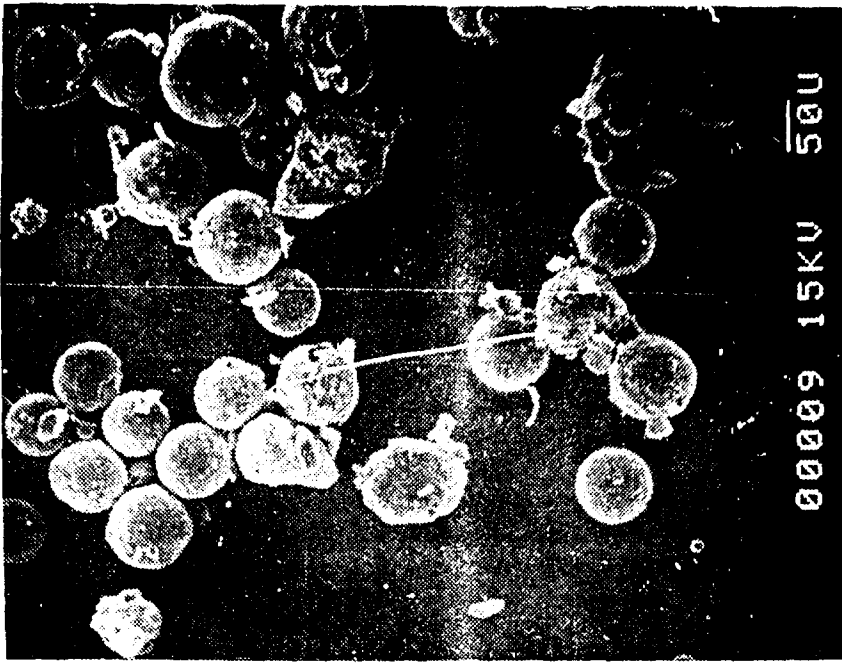
(b)



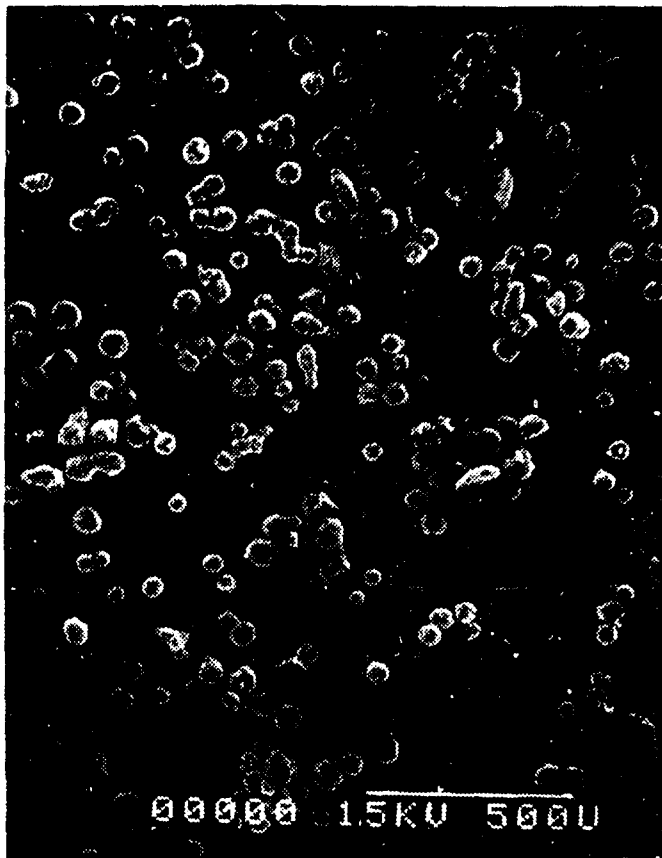
(c)



(a)

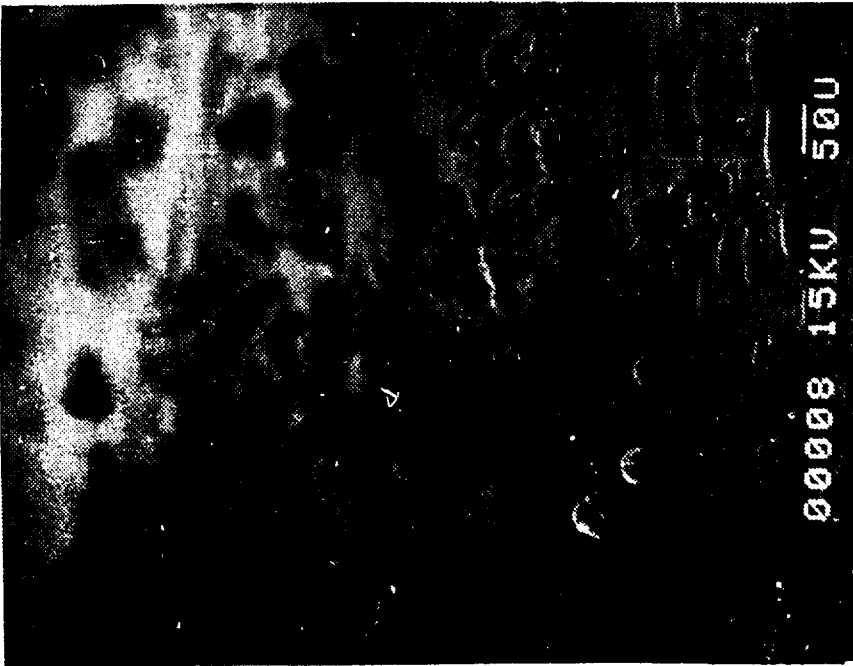


(e)

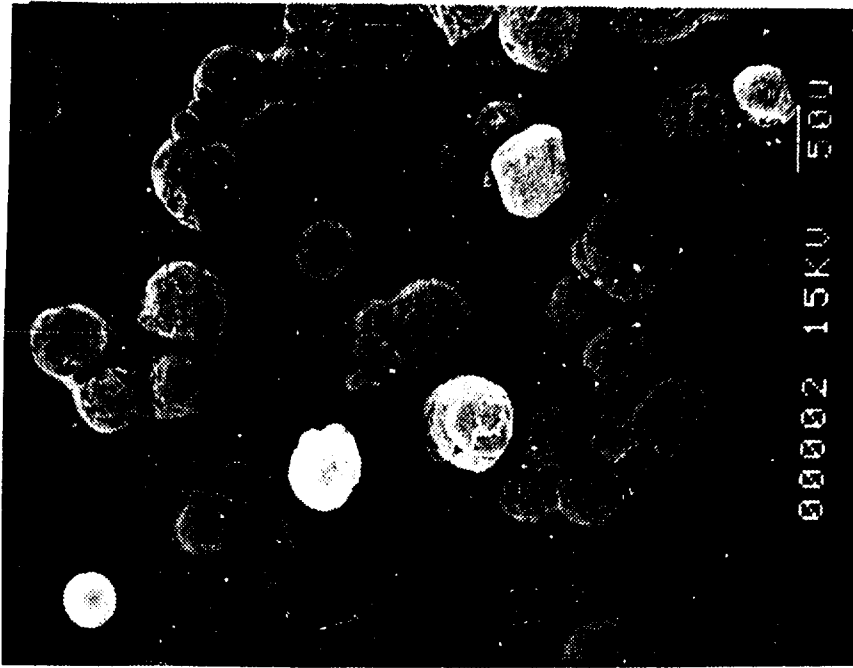


(a)

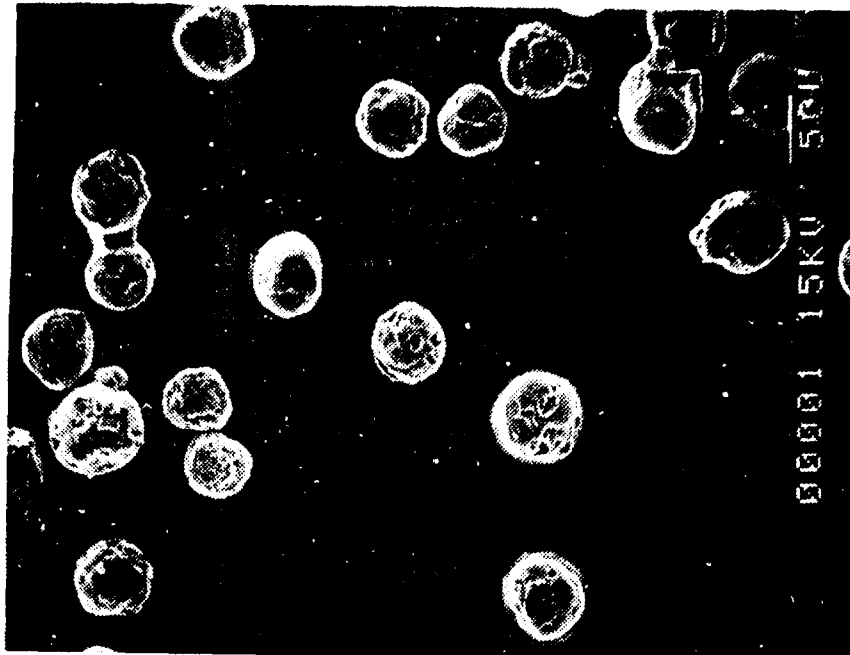
FIGURE 25 Photomicrographs of Postfire Residue  
(10030030580, WGS-6A,  $P_c = 34$  atm.)



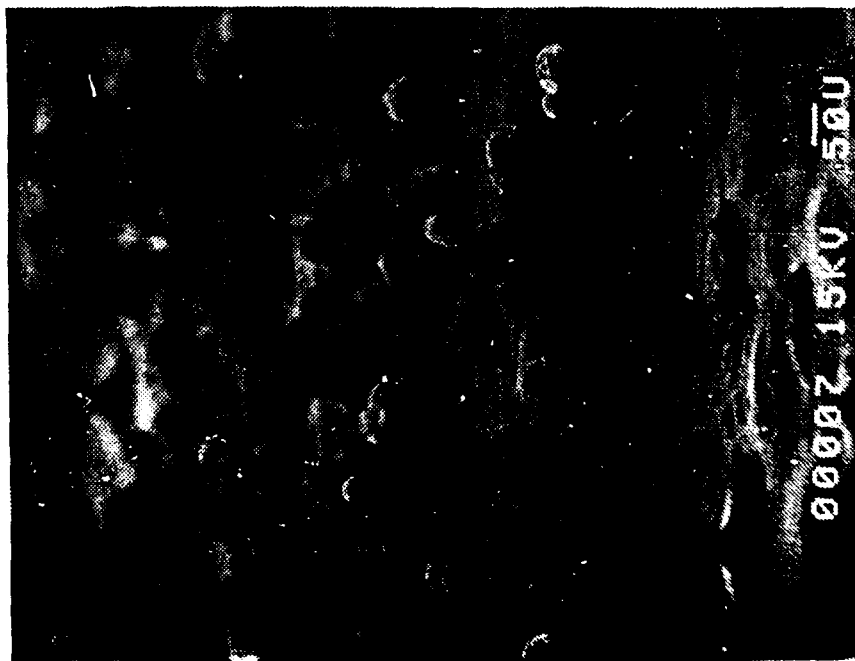
(b)



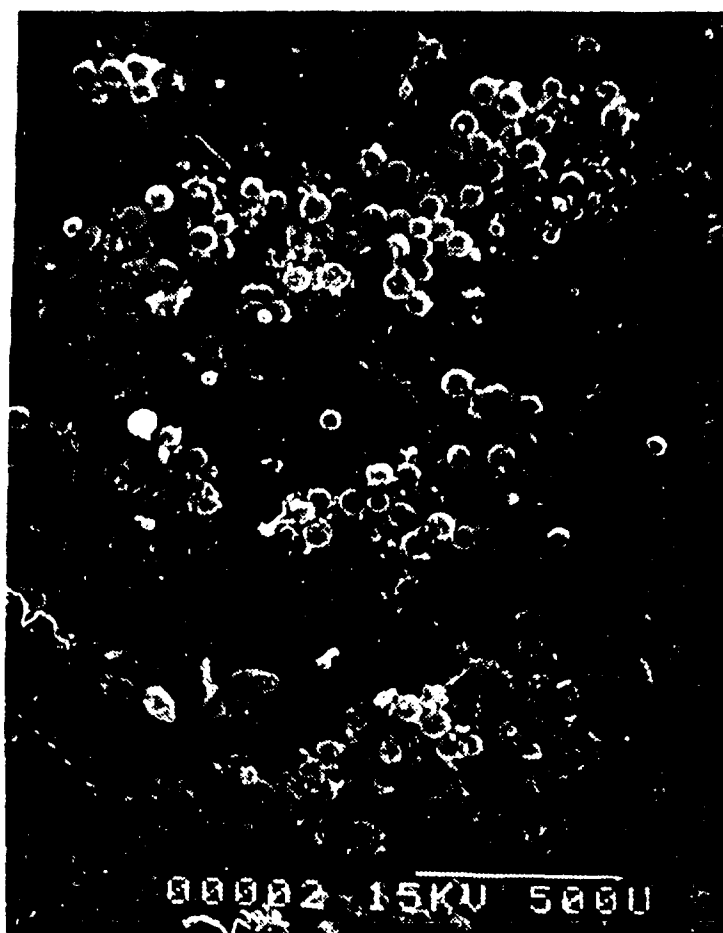
(c)



(e)



(d)

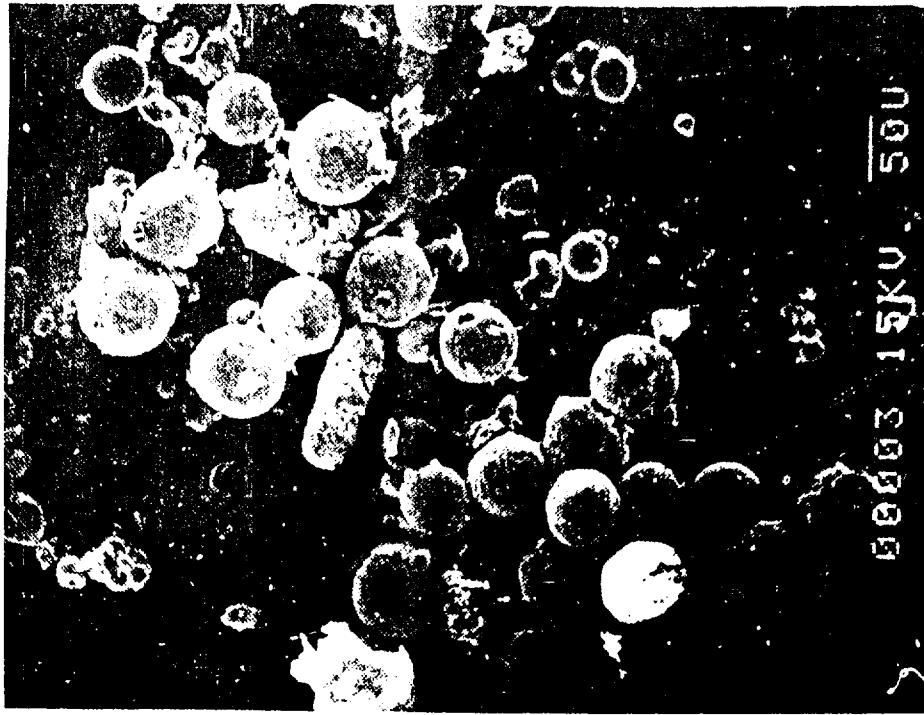


(a)

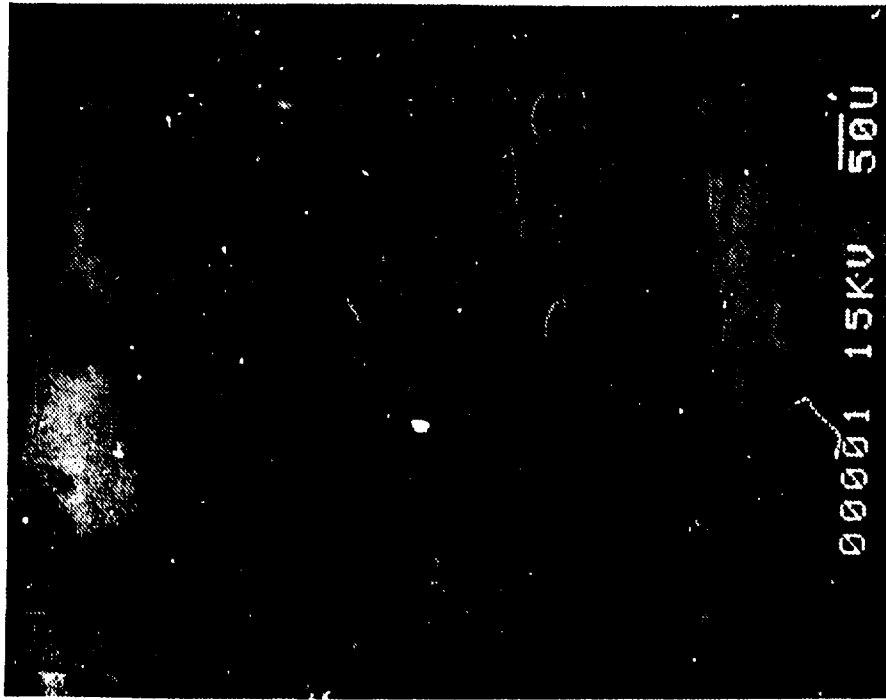
FIGURE 26 Photomicrographs of Postfire Residue  
(160017040, WGS-6A,  $P_c = 68$  atm. )



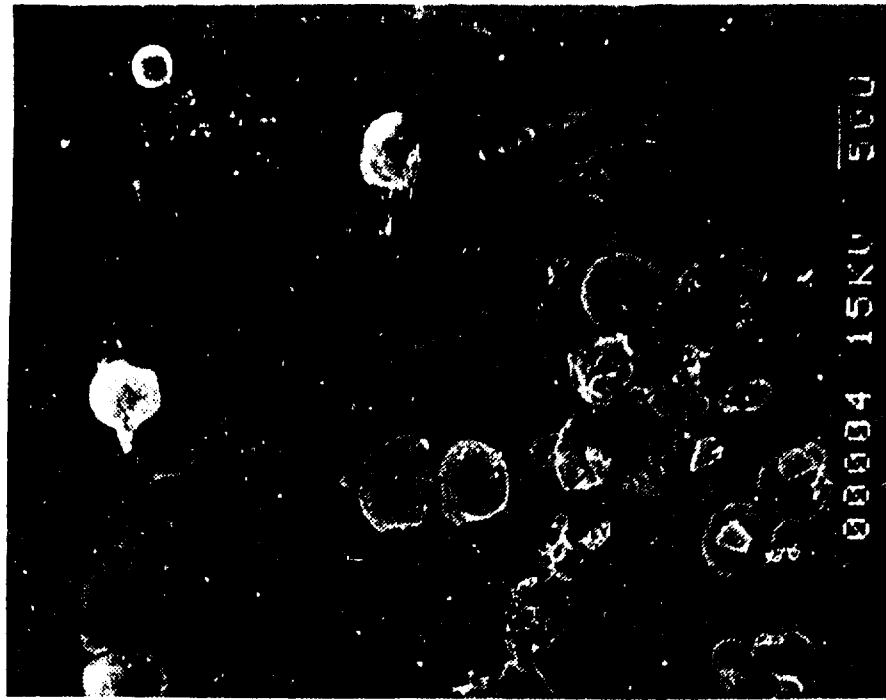
(b)



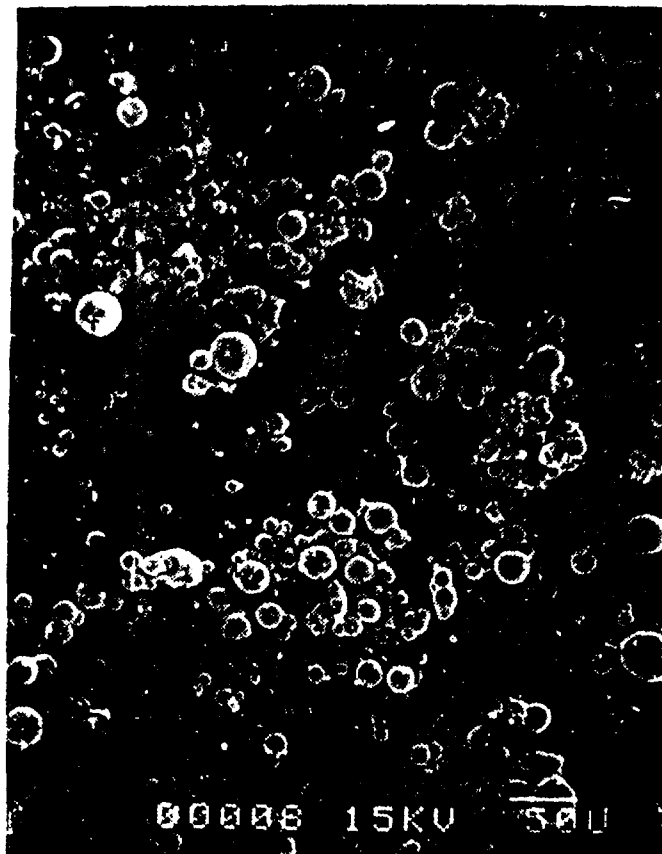
(c)



(d)

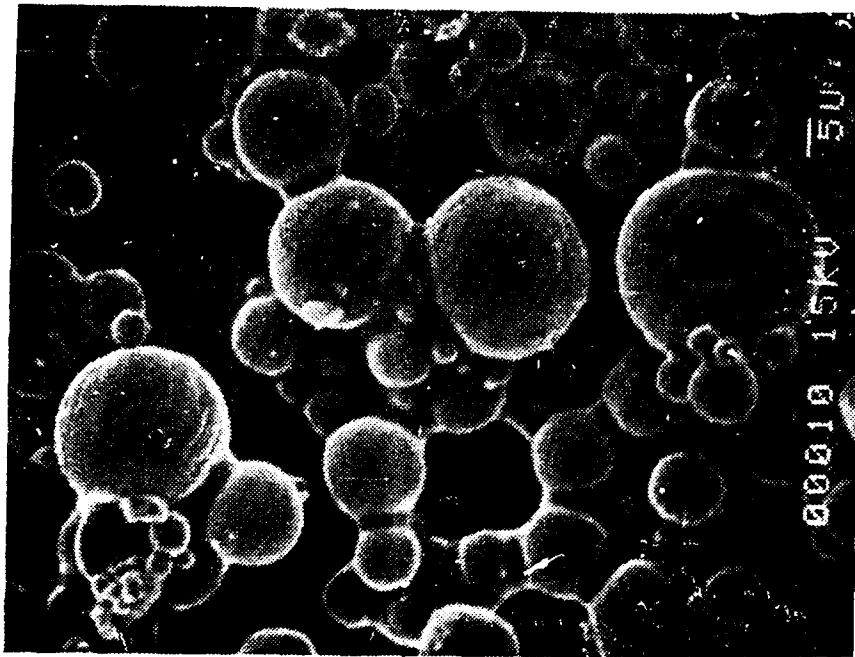


(e)



(a)

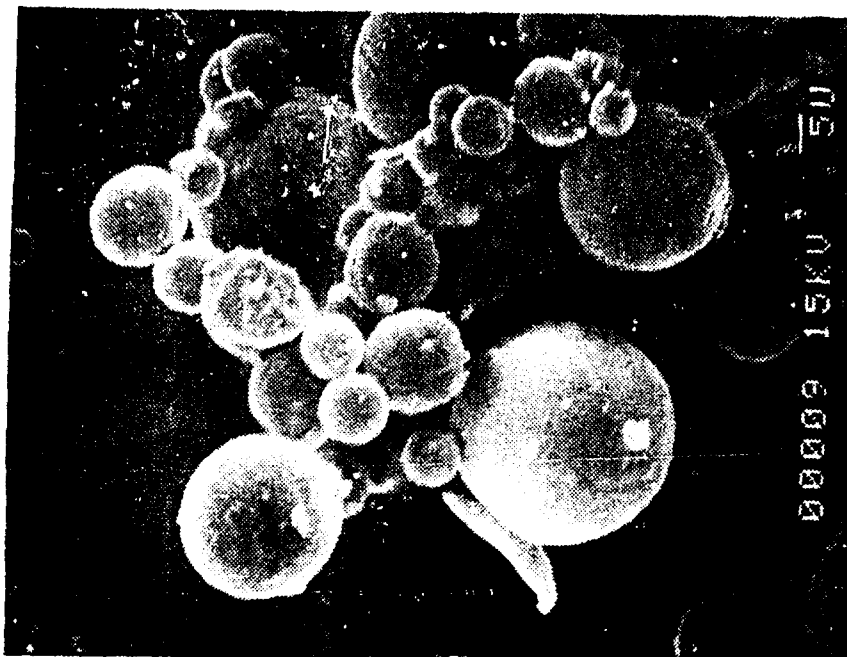
FIGURE 27 Photomicrographs of Postfire Residue  
(1215030580, WGS-7A,  $P_c = 34$  atm.)



(c)



(b)



(e)



(d)



(a)

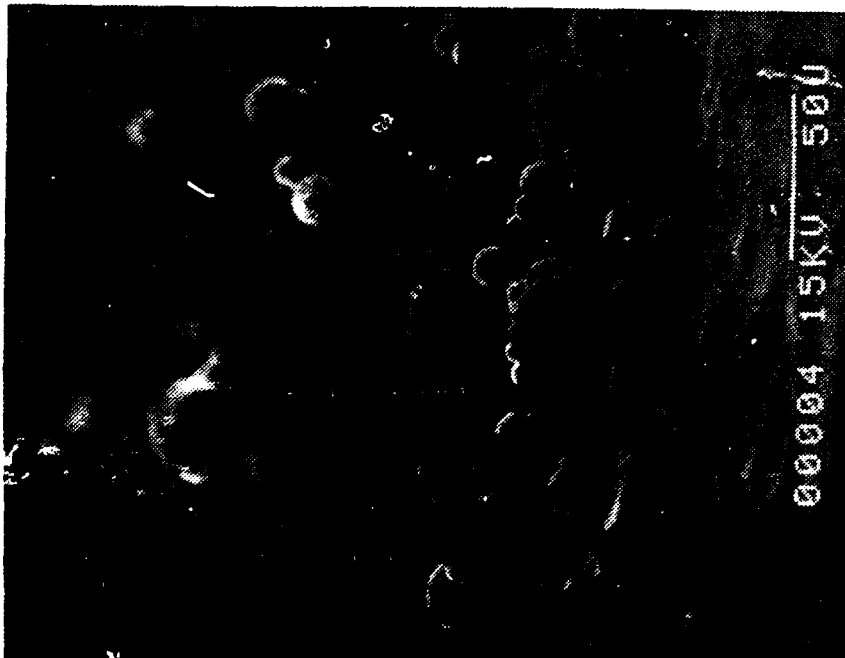
FIGURE 28 Photomicrographs of Postfire Residue  
(1400240480, WGS-7A,  $P_c = 68$  atm.)



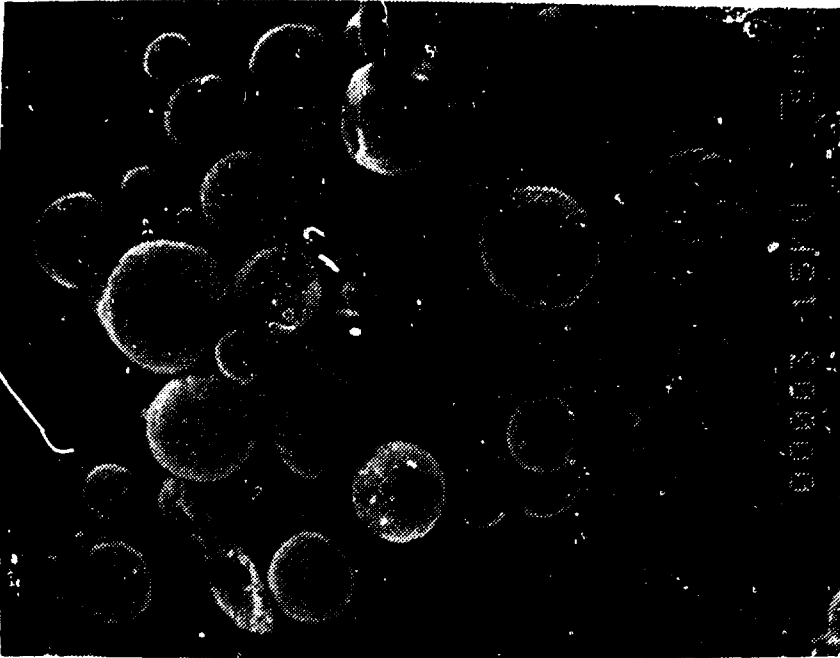
(b)



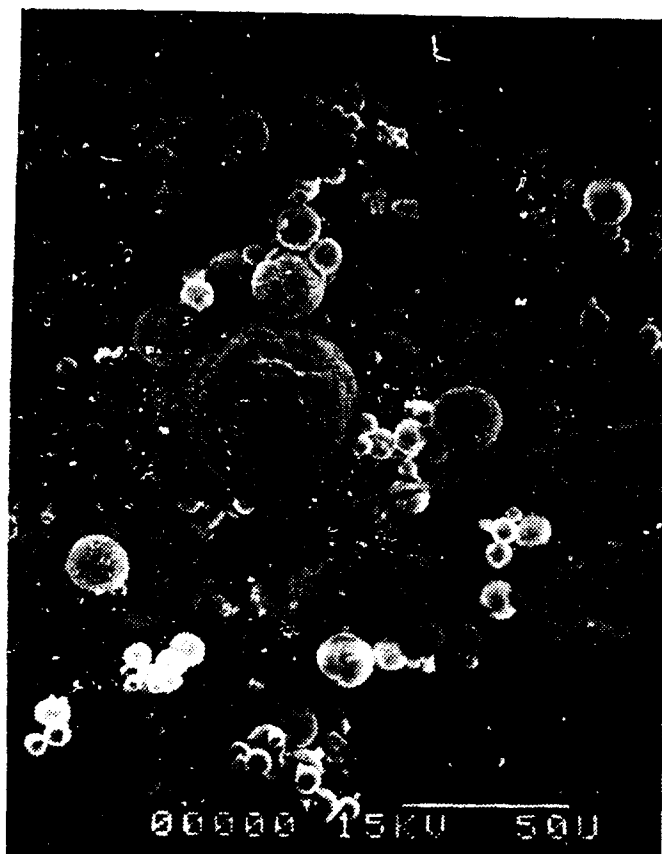
(c)



(a)



(e)

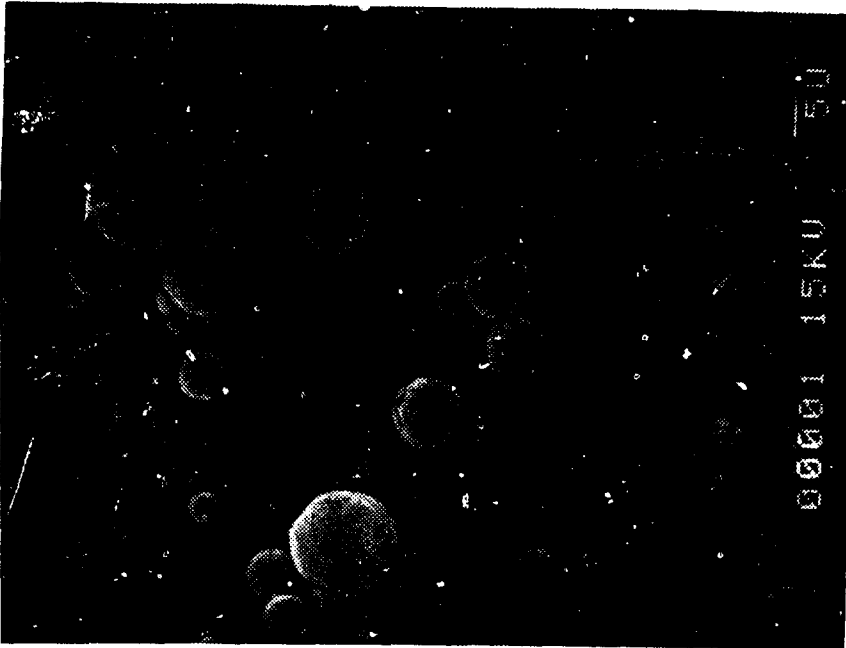


(a)

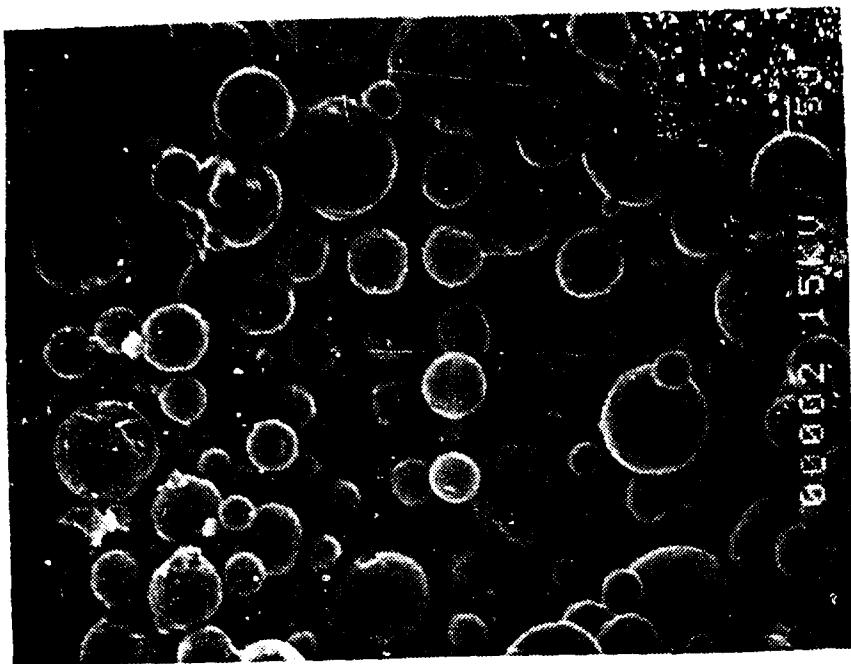
FIGURE 29 Photomicrographs of Postfire Residue  
(1100030580, WGS-7,  $P_c = 34$  atm.)



(b)



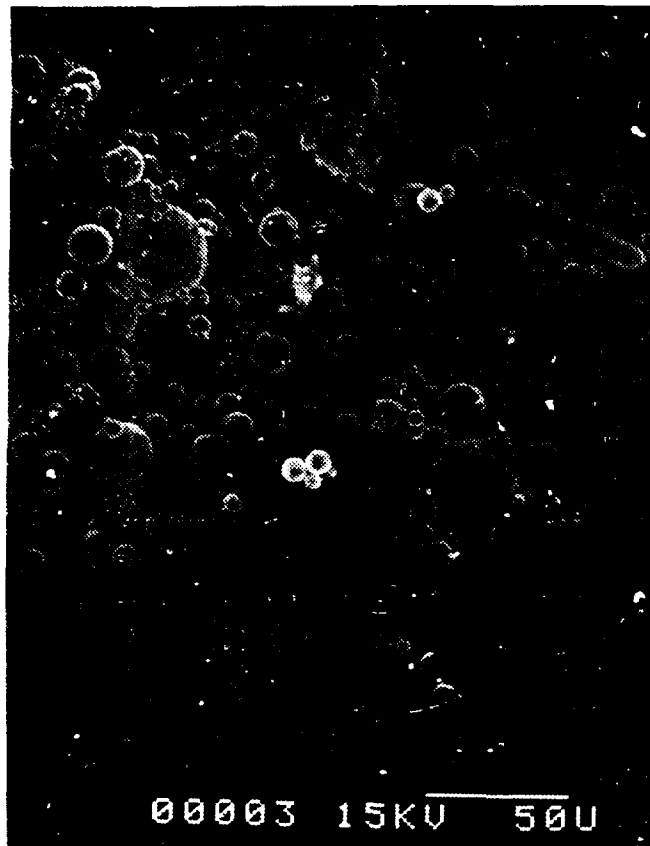
(c)



(e)



(d)

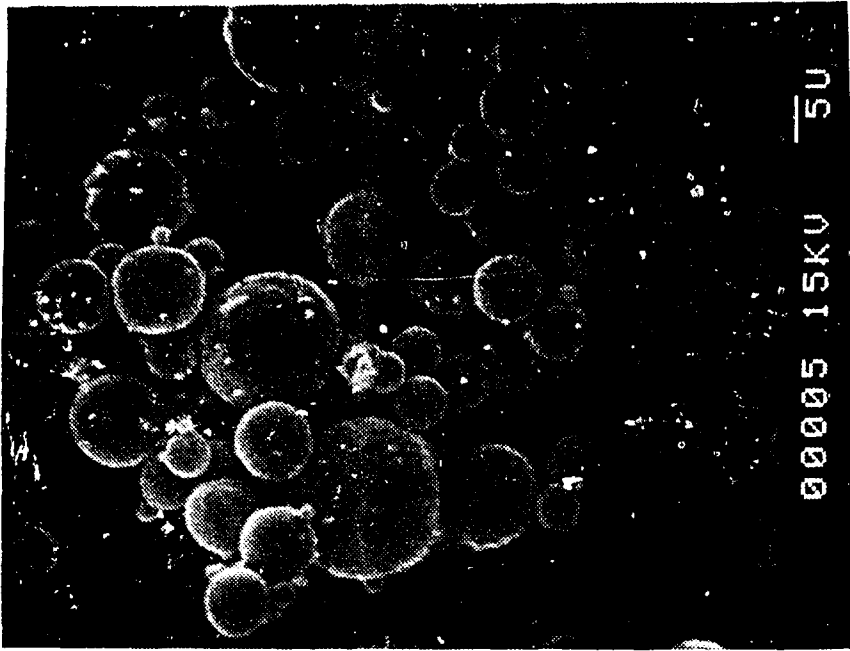


(a)

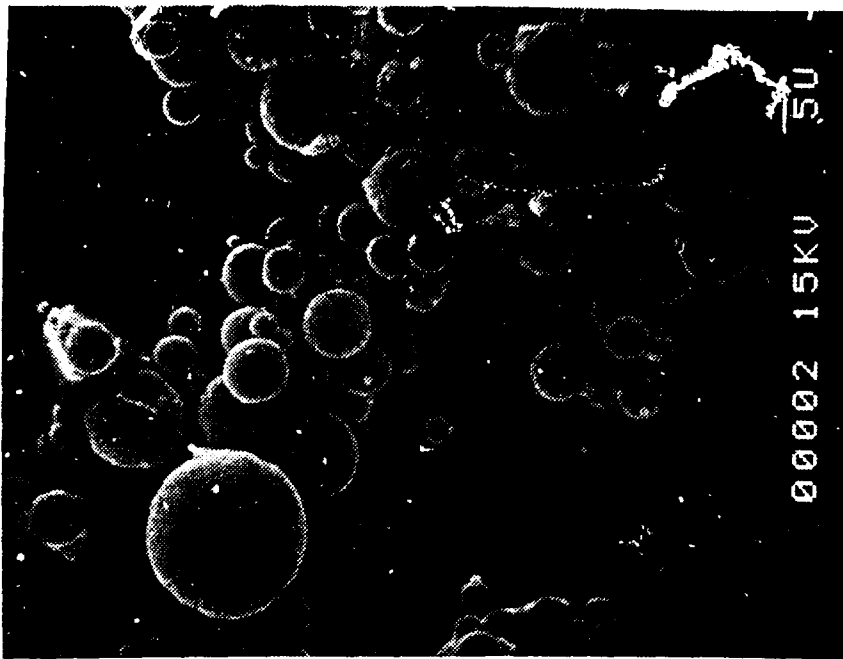
FIGURE 30 Photomicrographs of Postfire Residue  
(1500210480, WGS-7,  $P_c = 68$  atm. )



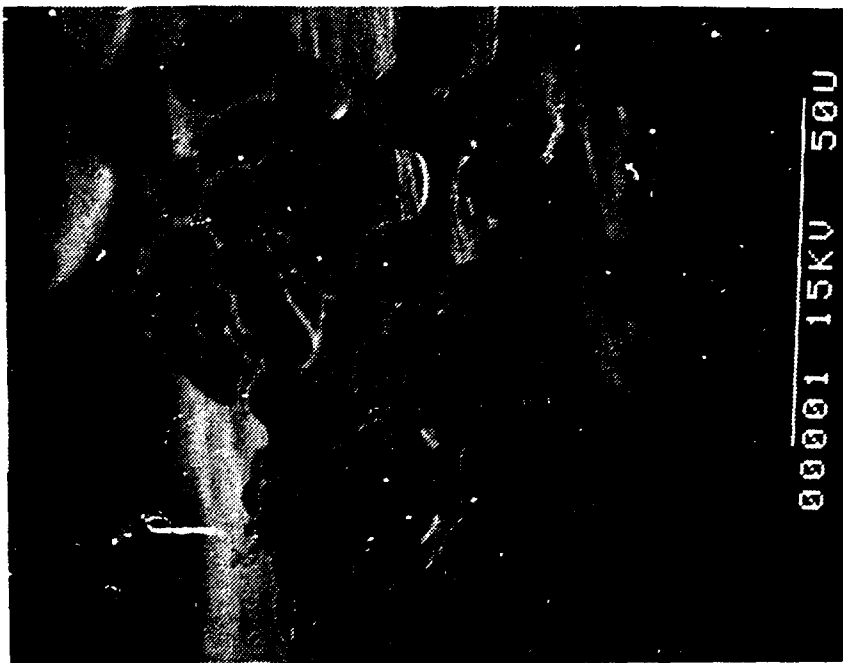
(b)



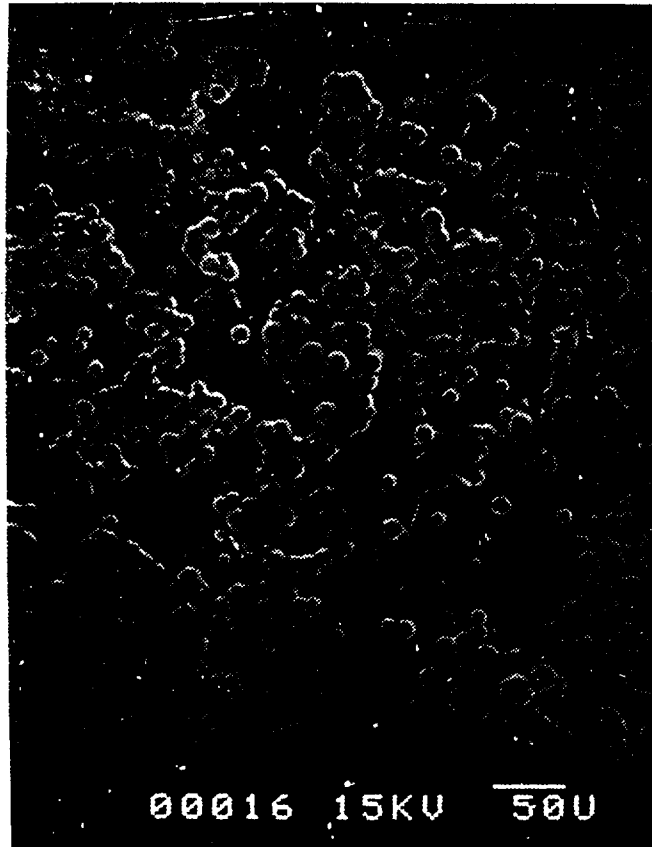
(c)



(e)

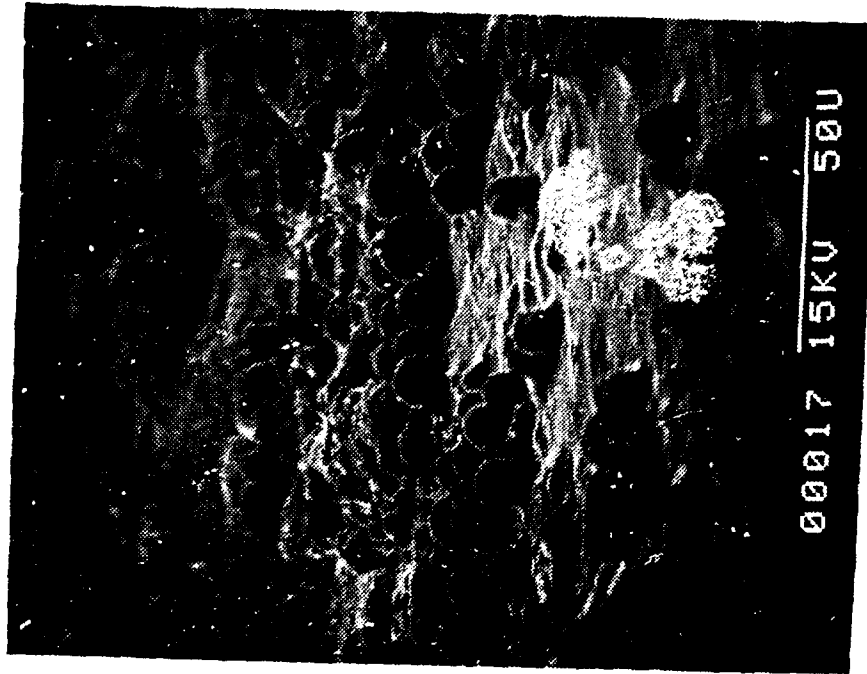


(d)

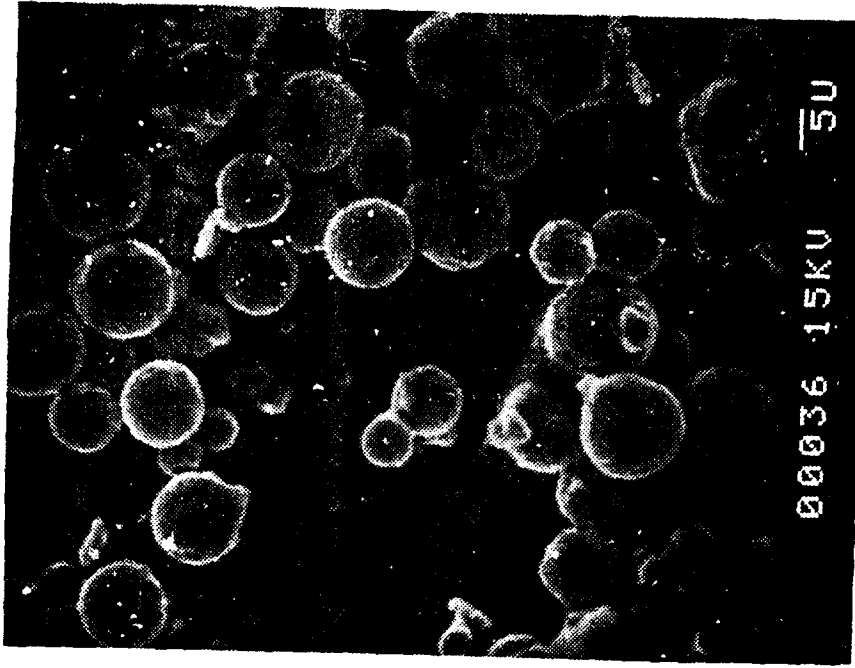


(a)

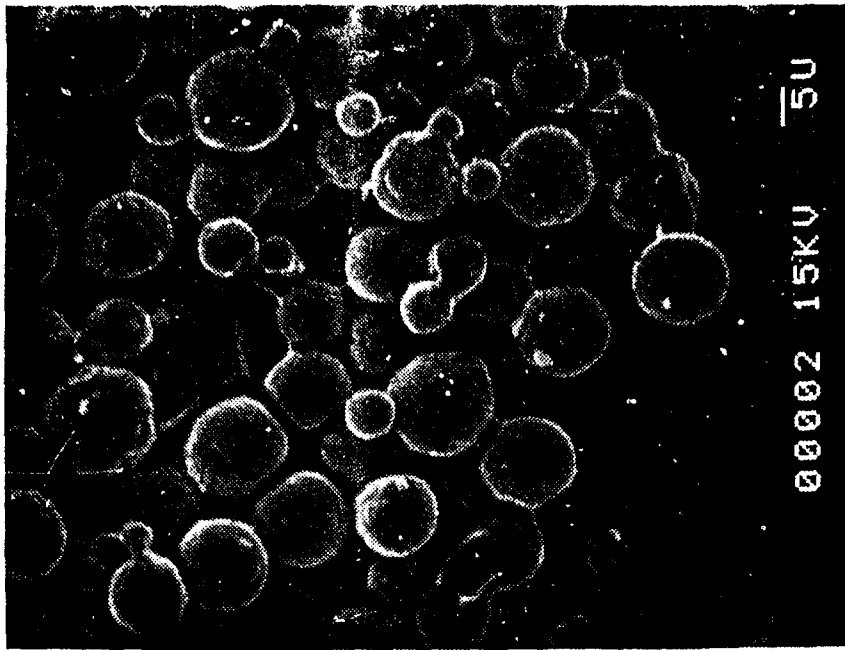
FIGURE 31 Photomicrographs of Postfire Residue  
(1230110580, NWC-1,  $P_c = 34$  atm.)



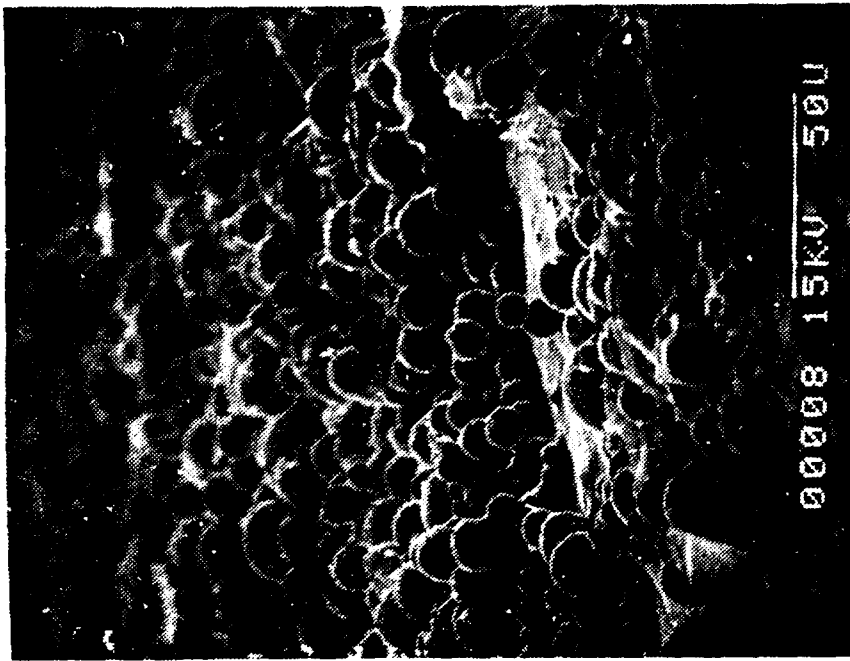
(b)



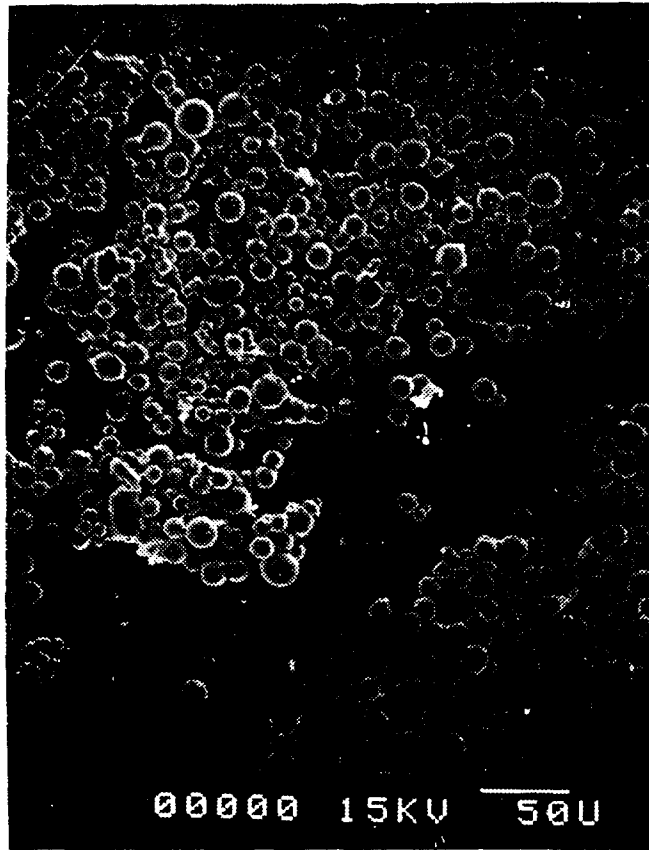
(c)



(e)

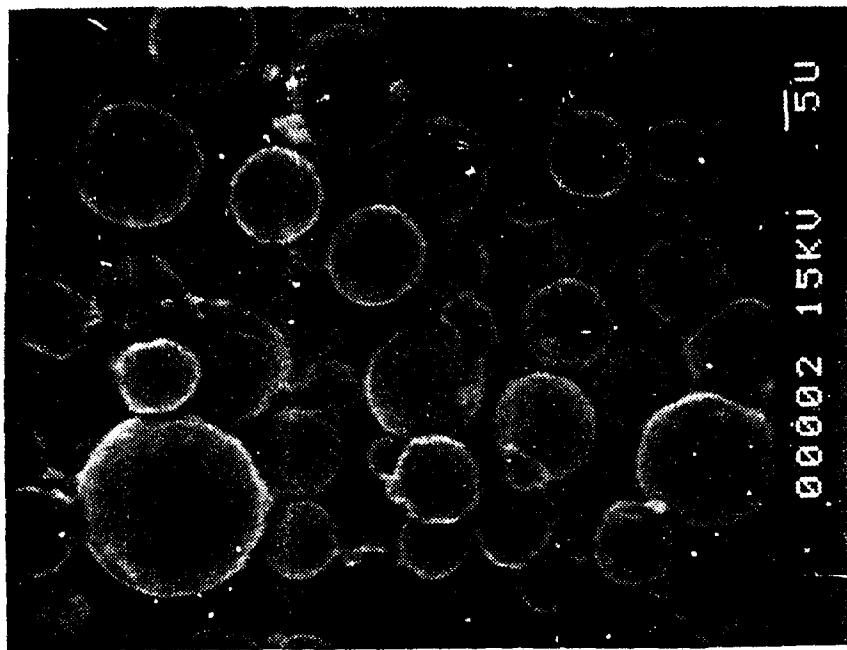


(d)

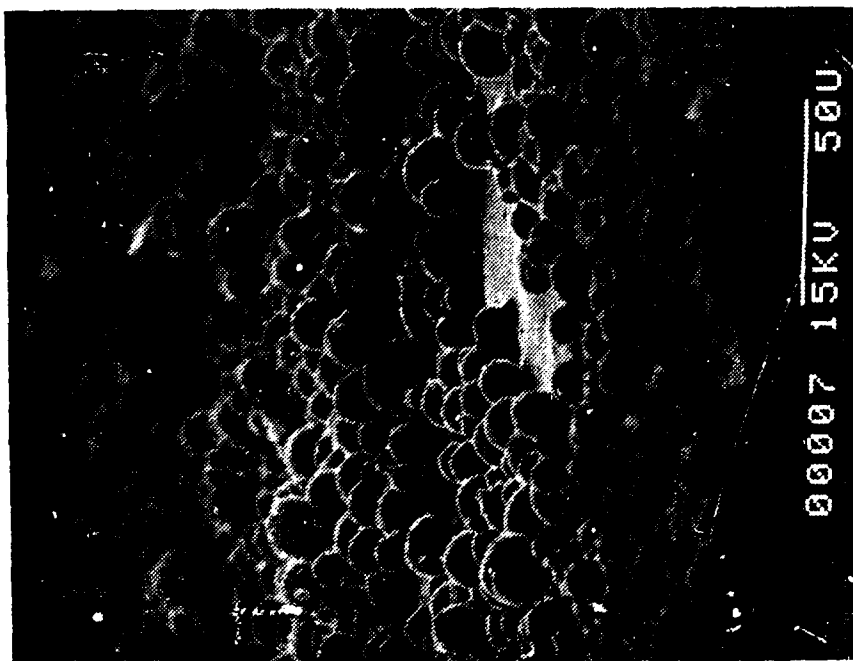


(a)

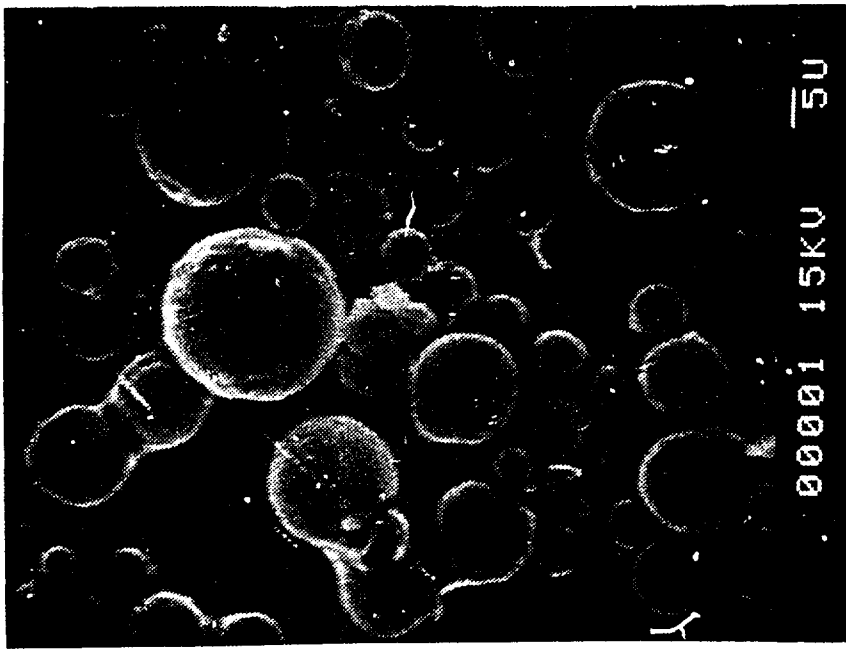
FIGURE 32 Photomicrographs of Postfire Residue  
(150010580, NWC-1,  $P_c = 68$  atm. )



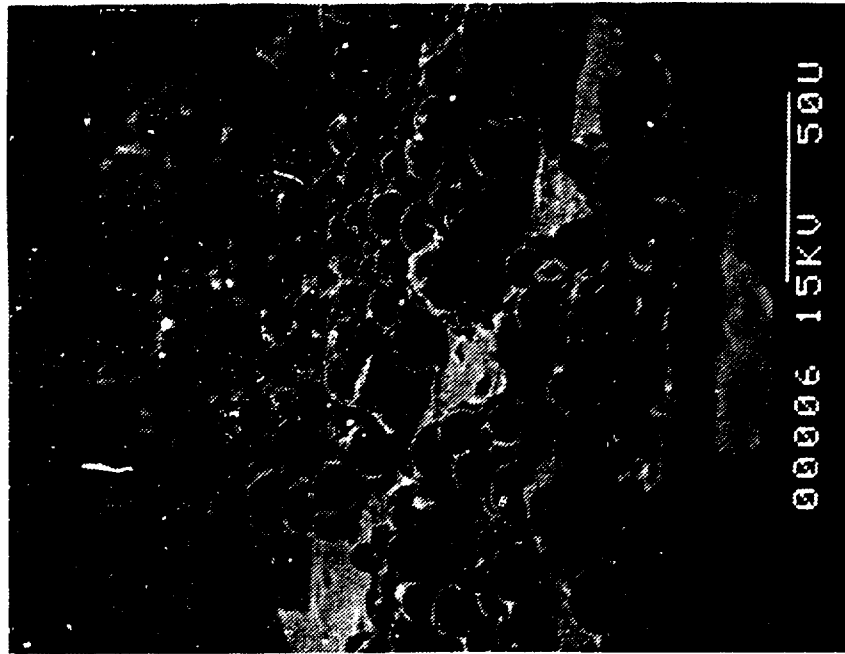
(c)



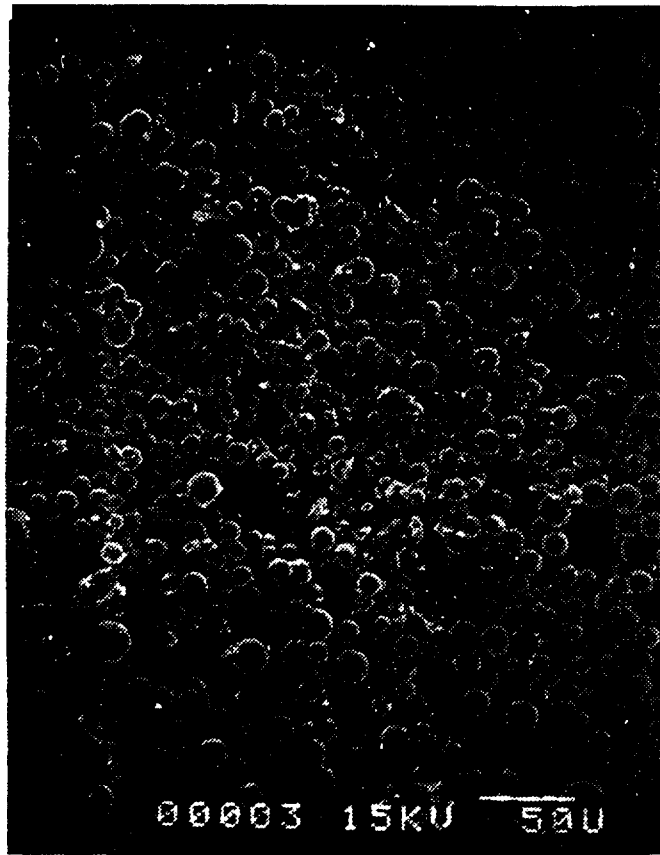
(b)



(e)

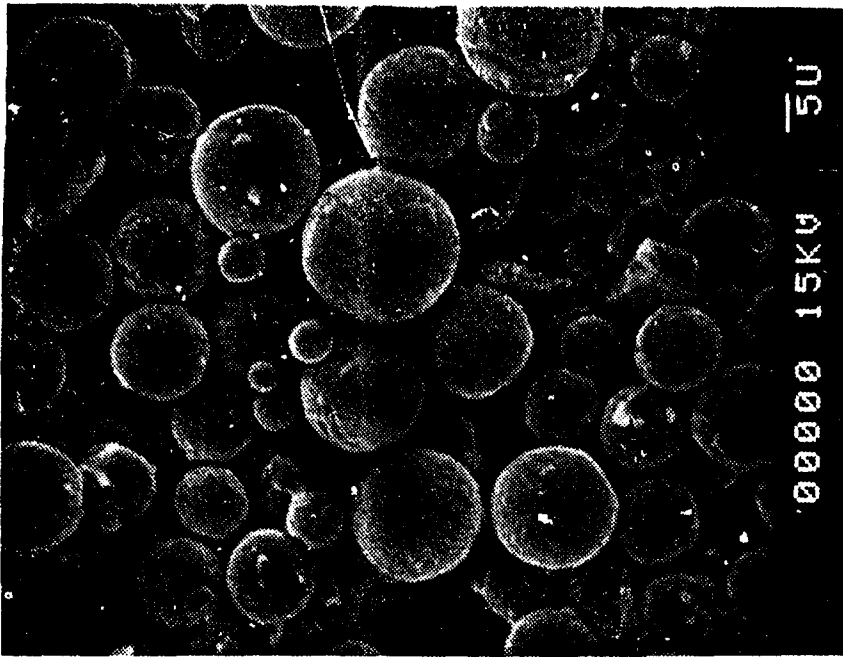


(d)

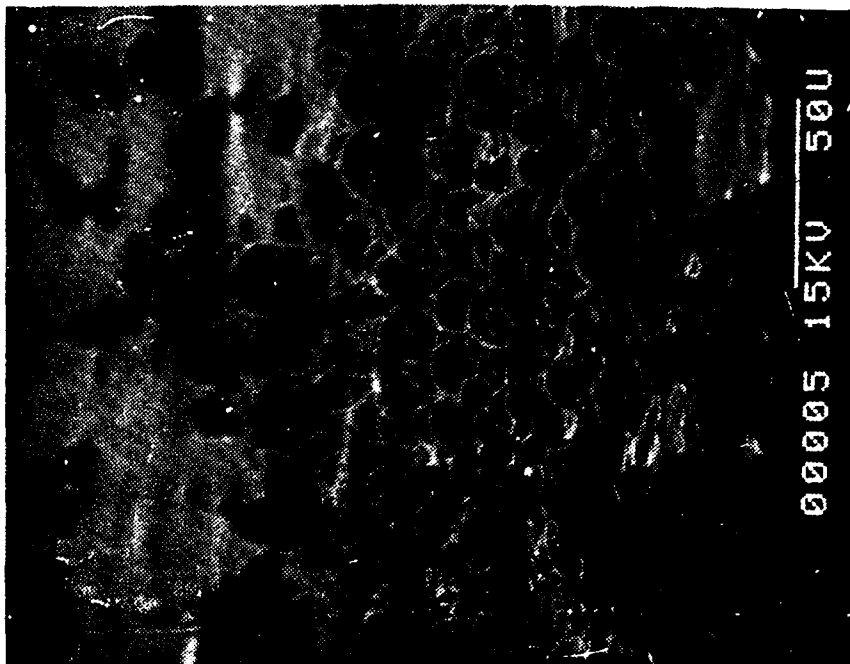


(a)

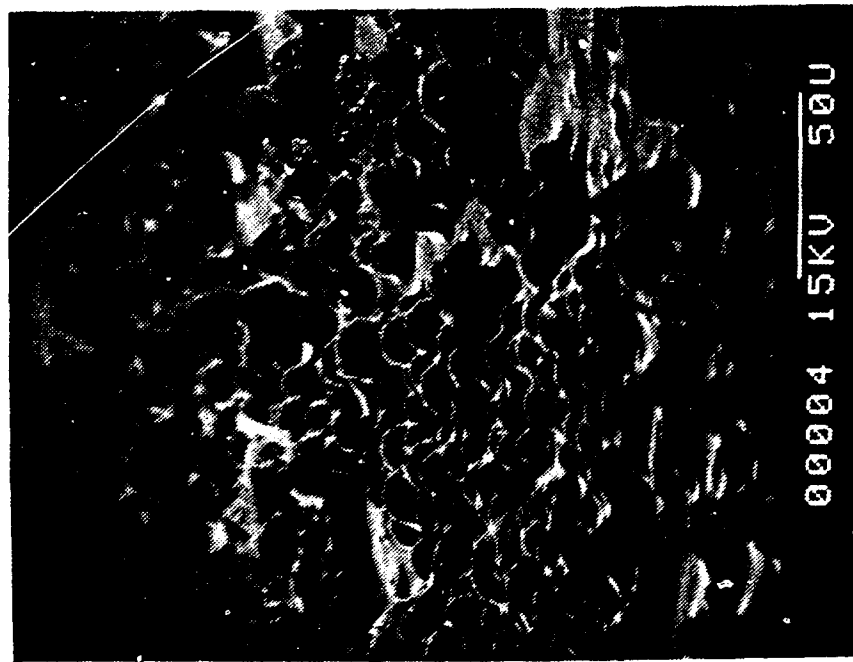
FIGURE 33 Photomicrographs of Postfire Residue  
(1200110580, NWC-2,  $P_c = 34$  atm.)



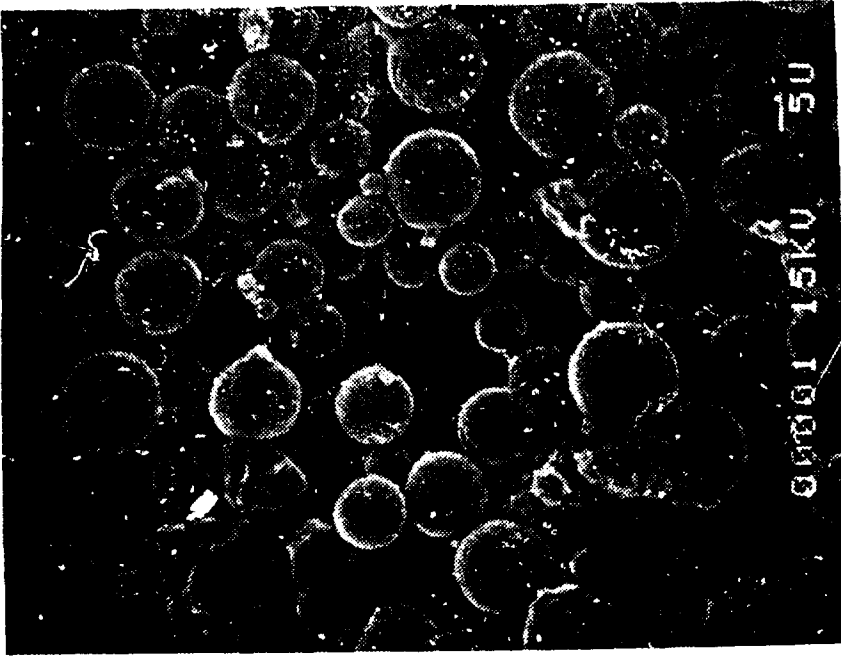
(c)



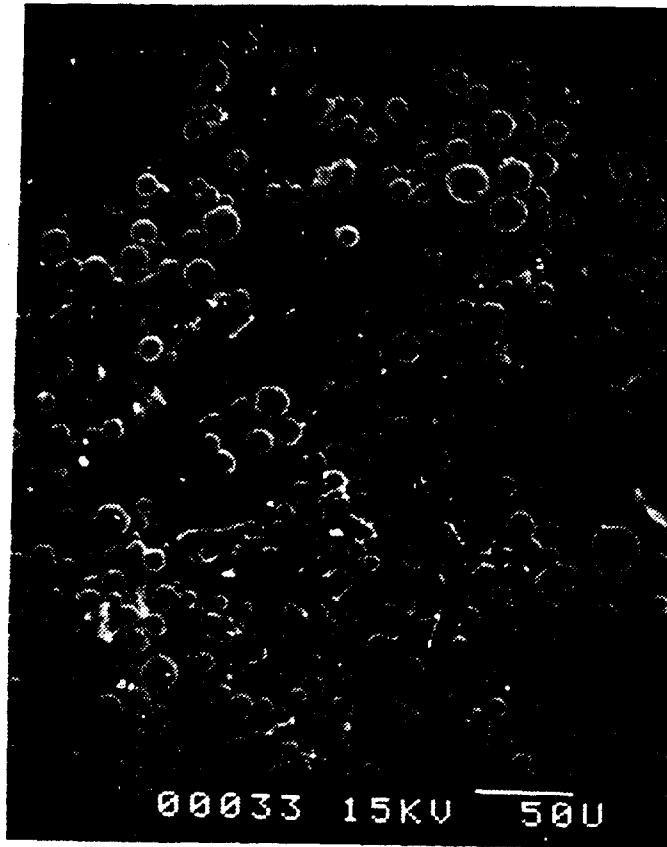
(b)



(a)

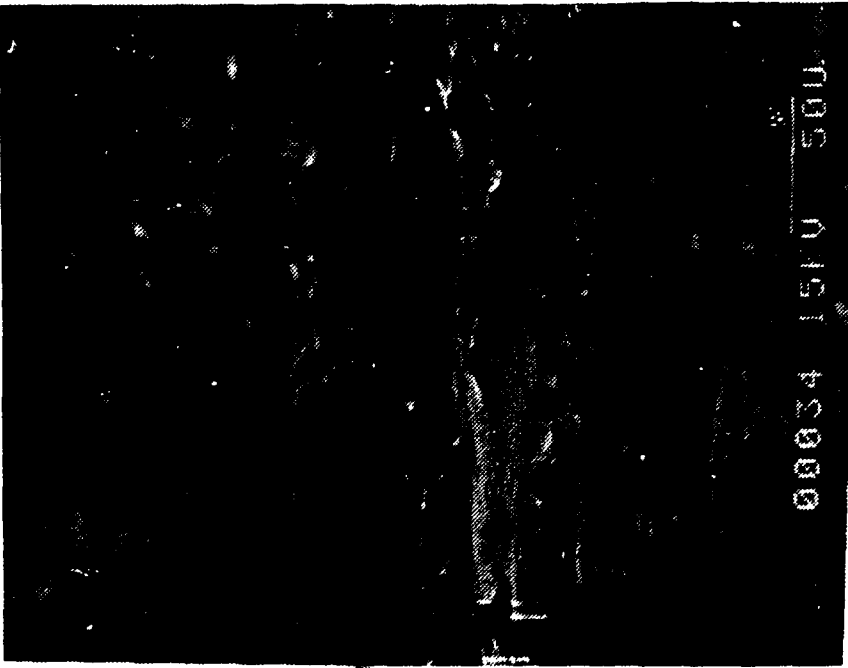


(e)

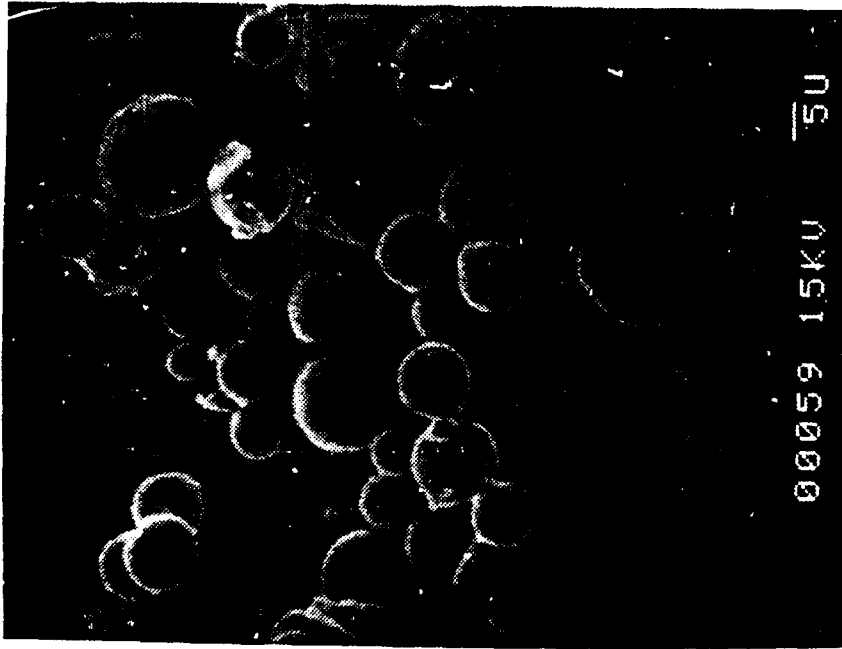


(a)

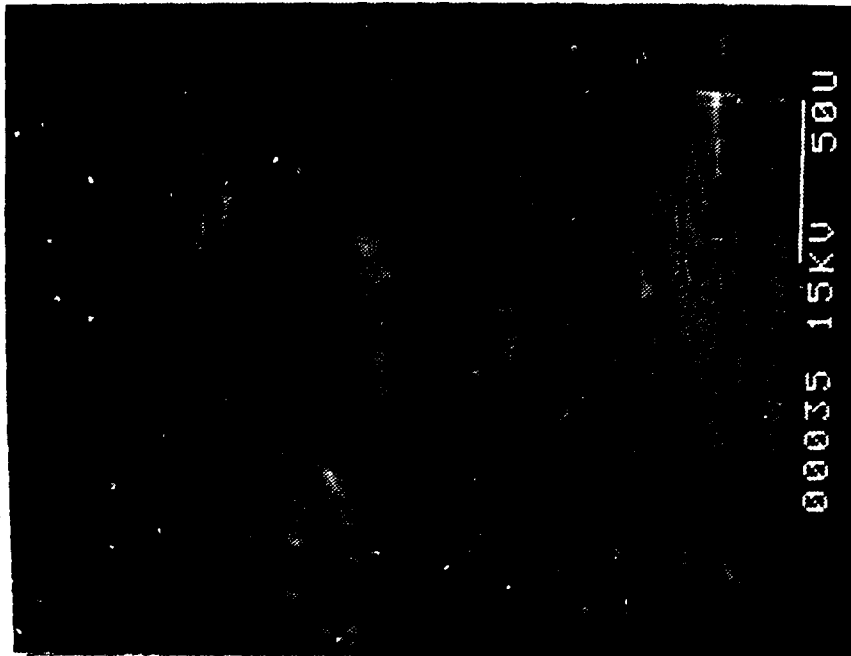
FIGURE 34 Photomicrographs of Postfire Residue  
(1615100580, NWC-2,  $P_c = 68$  atm. )



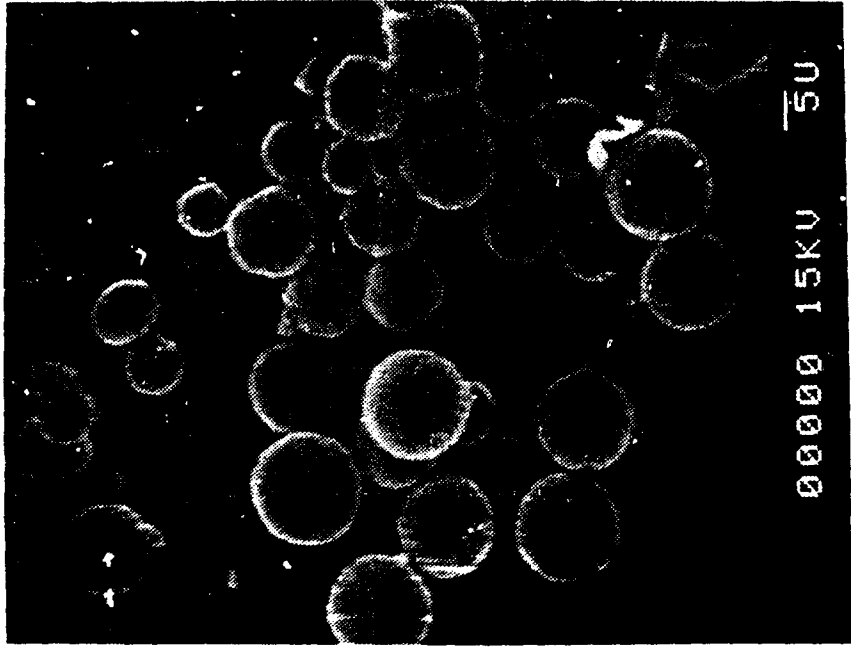
(b)



(c)



(d)



(e)

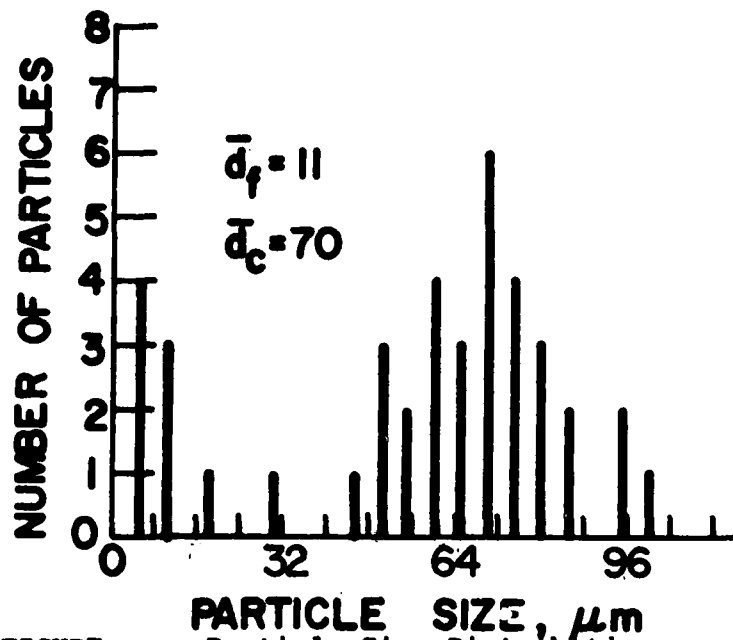


FIGURE 35 Particle Size Distribution  
 (1445240480, WGS-5A,  $P_c = 34$  atm. )

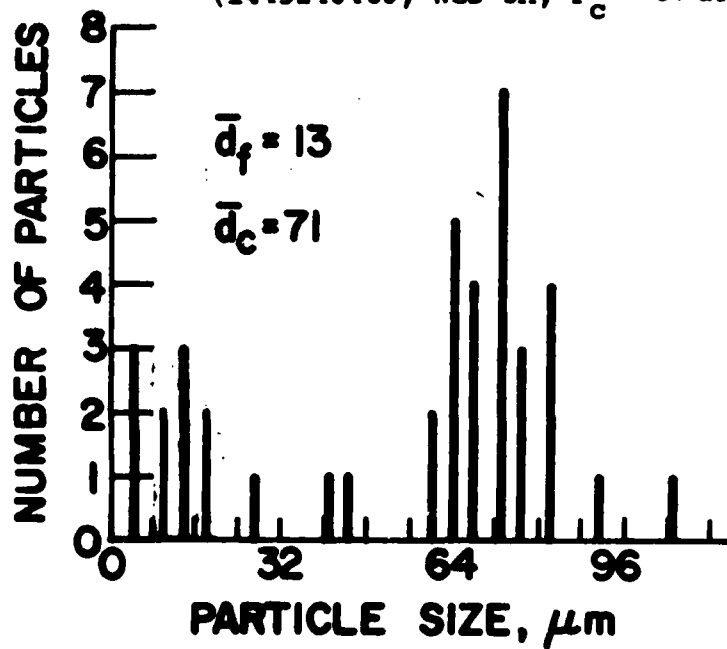


FIGURE 36 Particle Size Distribution  
 (1445180480, WGS-5A,  $P_c = 68$  atm. )

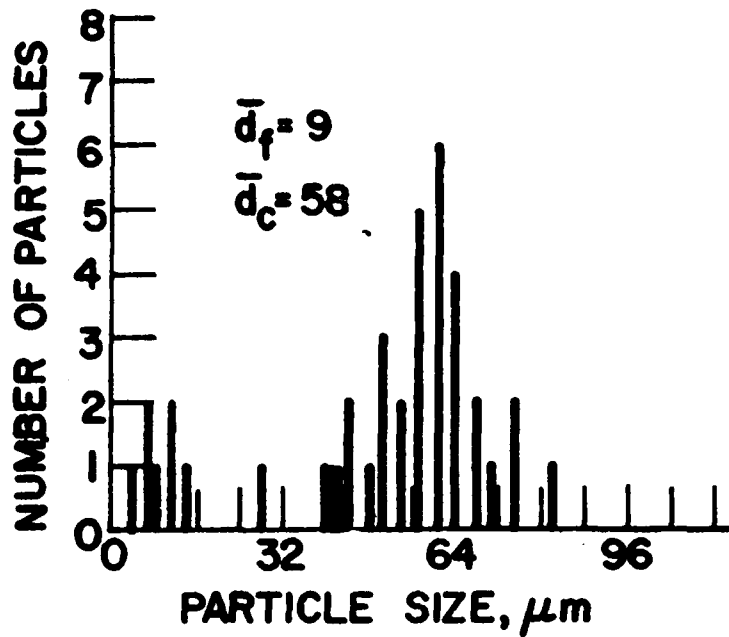


FIGURE 37 Particle Size Distribution  
(1030030580, WGS-6A,  $P_c = 34$  atm.)

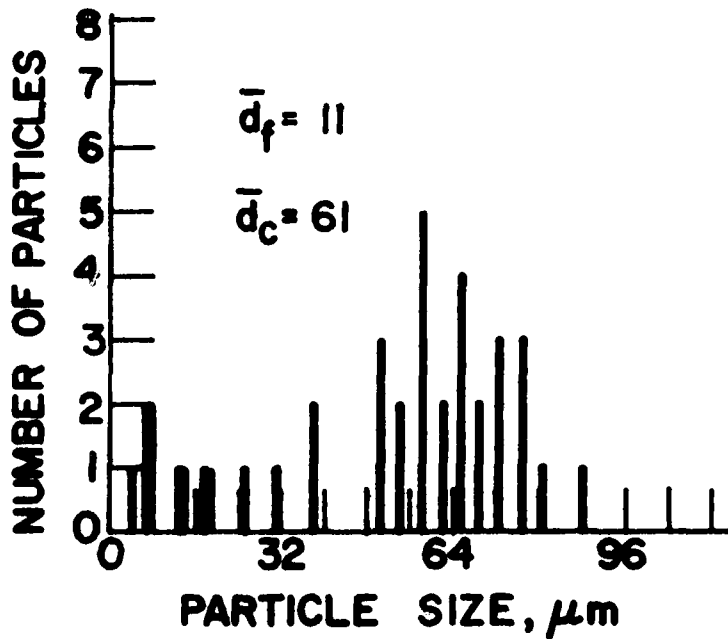


FIGURE 38 Particle Size Distribution  
(1600170480, WGS-6A,  $P_c = 68$  atm.)

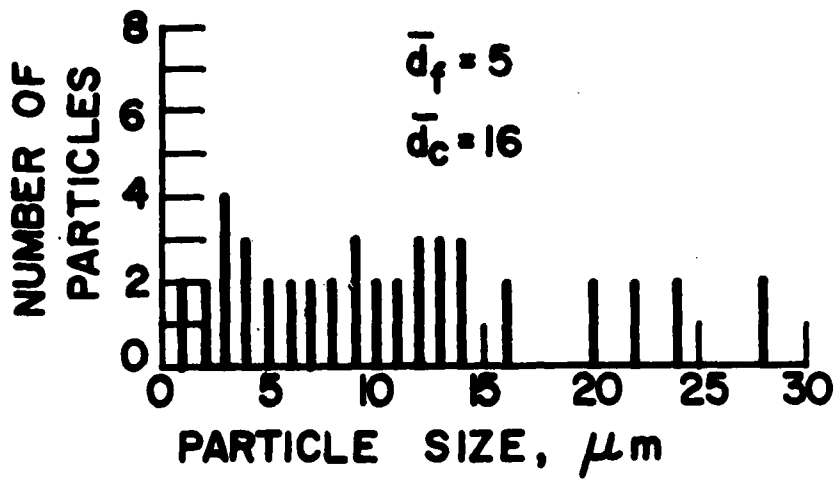


FIGURE 39 Particle Size Distribution  
(1215030580, WGS-7A,  $P_c = 34$  atm.)

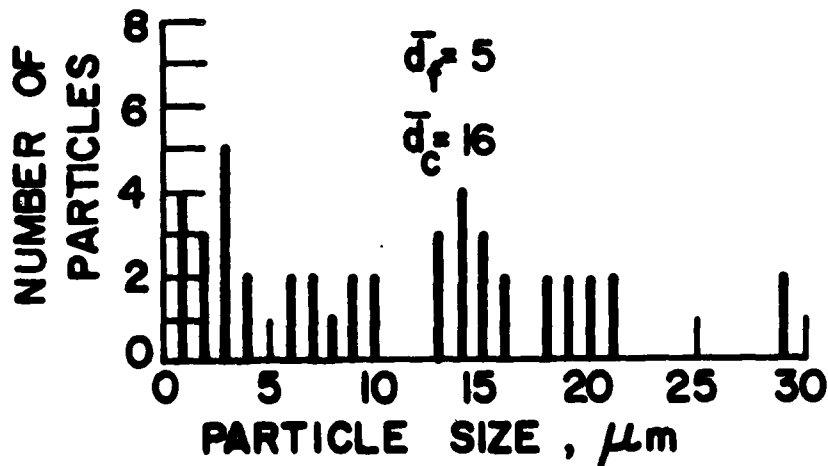


FIGURE 40 Particle Size Distribution  
(1400240480, WGS-7A,  $P_c = 68$  atm.)

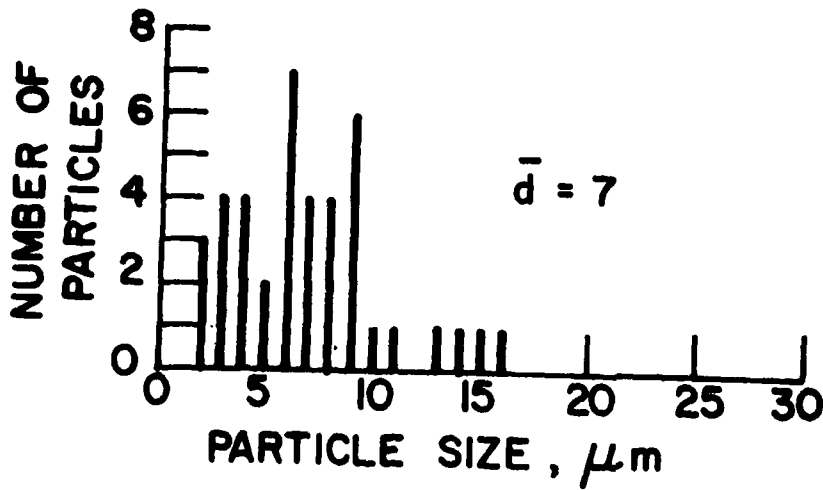


FIGURE 41 Particle Size Distribution  
(1100030580, WGS-7,  $P_c = 34$  atm.)

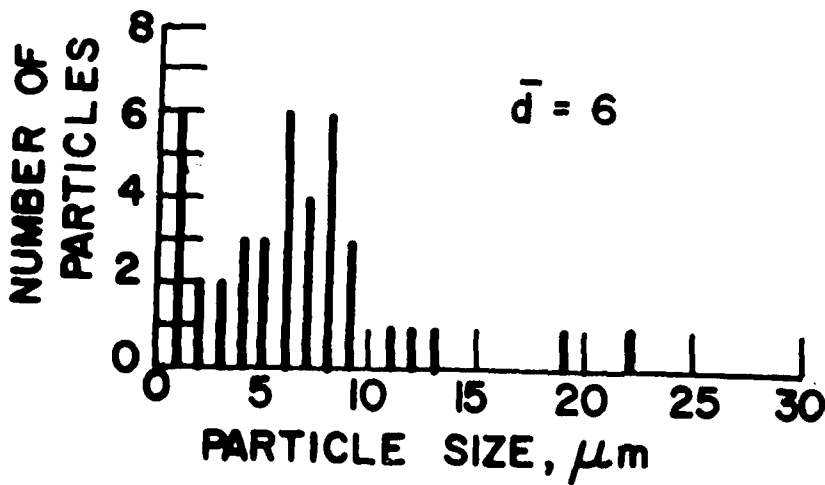


FIGURE 42. Particle Size Distribution  
(1500210480, WGS-7,  $P_c = 68$  atm.)

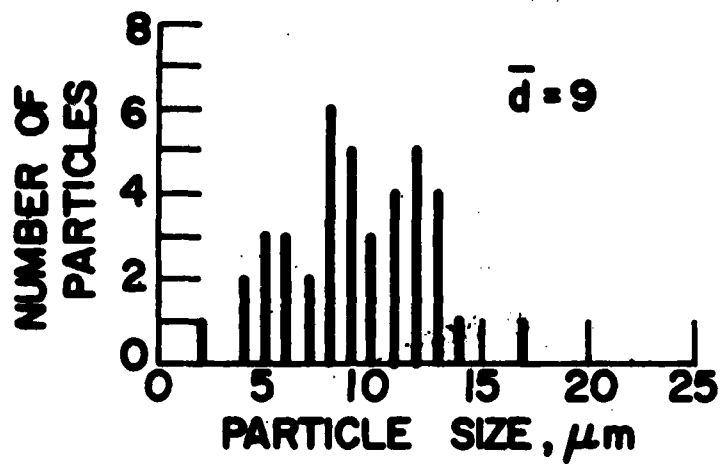


FIGURE 43 Particle Size Distribution  
(1230110580, NWC-1,  $P_c = 34$  atm.)

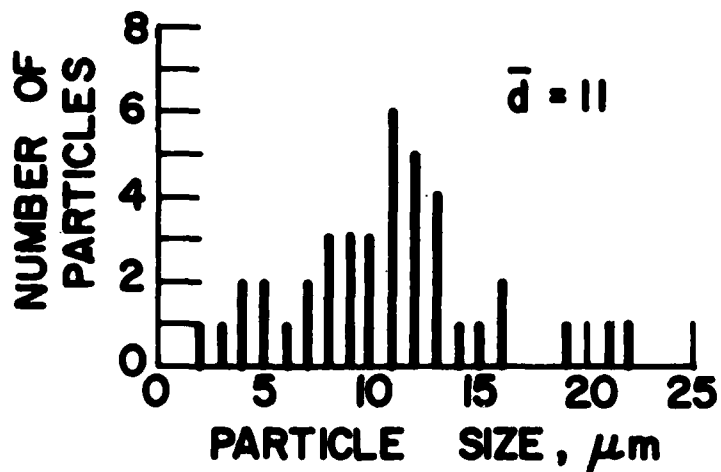


FIGURE 44 Particle Size Distribution  
(1500100580, NWC-1,  $P_c = 68$  atm. )

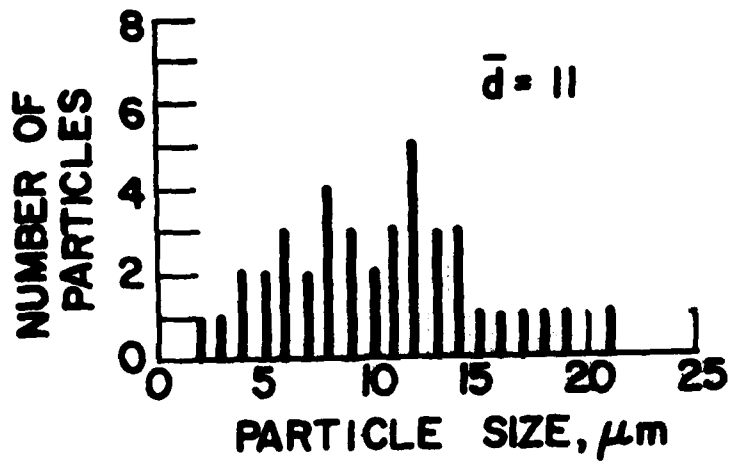


FIGURE 45. Particle Size Distribution  
(1200110580, NWC-2,  $P_c = 34$  atm.)

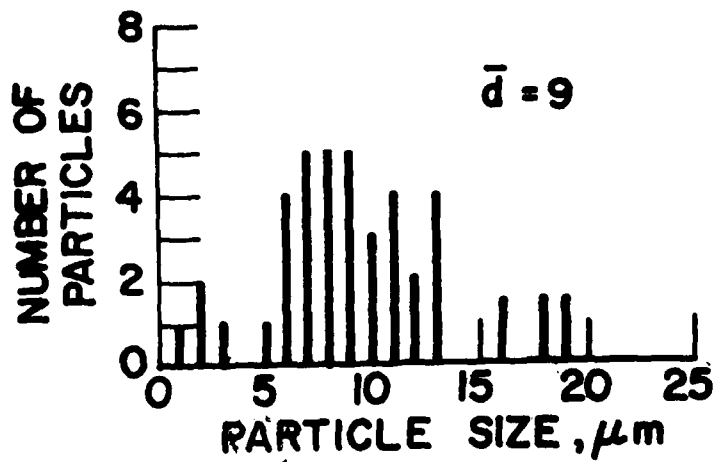
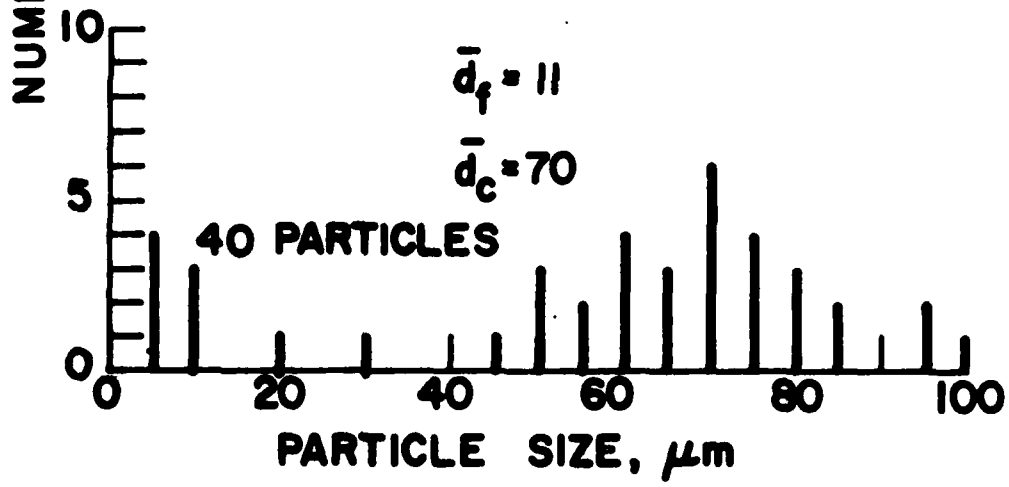
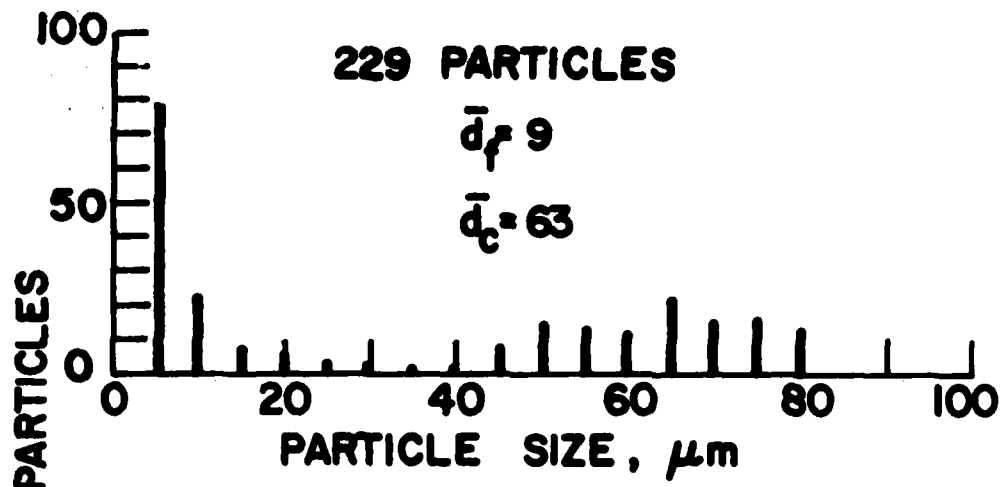


FIGURE 46. Particle Size Distribution  
(1615100580, NWC-2,  $P_c = 68$  atm.)



**FIGURE 47. Comparison of 40 and 220 Particle Sample Distributions (14452400480, WGS-5A,  $P_c = 34$  atm.)**

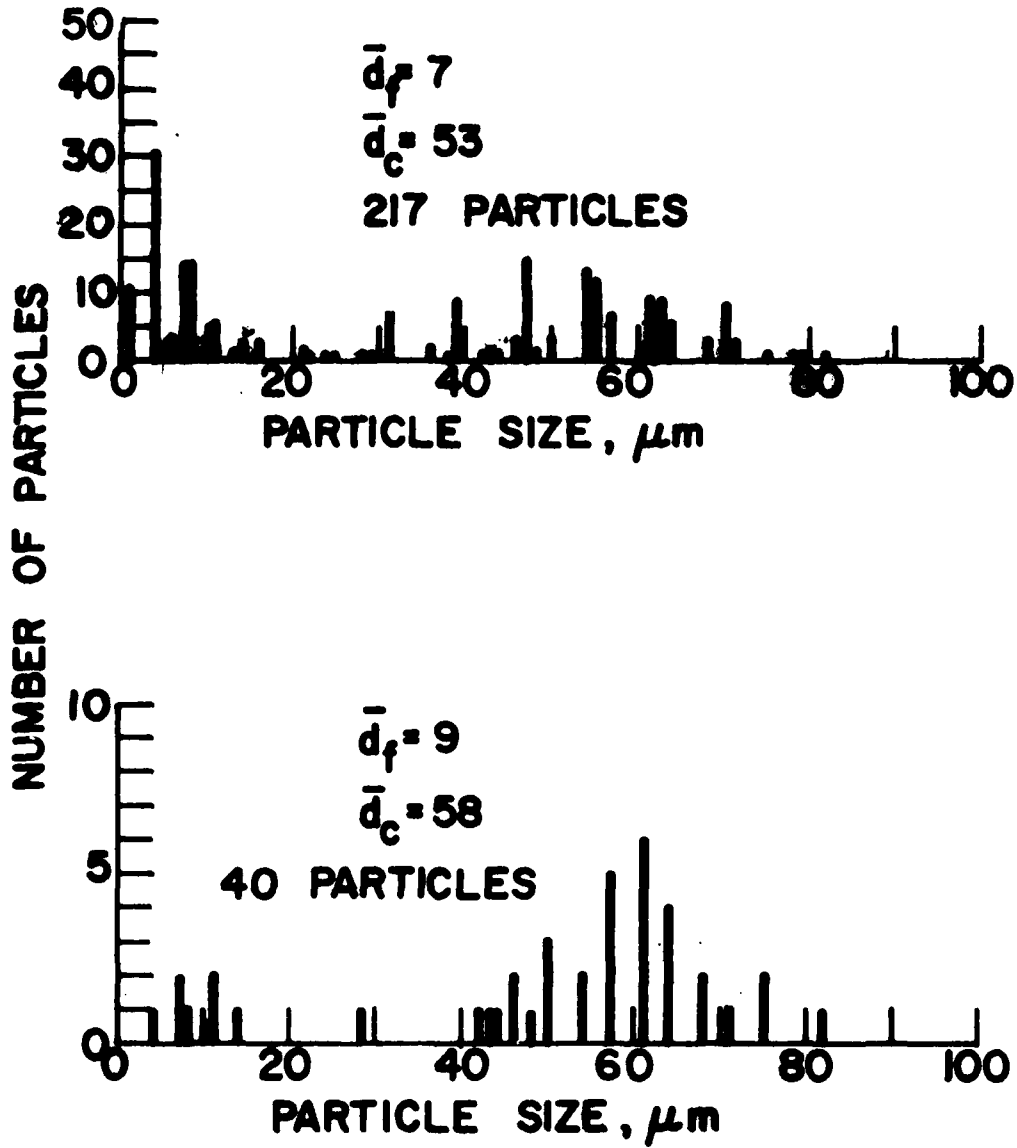


FIGURE 48. Comparison of 40 and 220 Particle Sample Distributions (1030030580, WGS-6A,  $P_c = 34$  atm.)

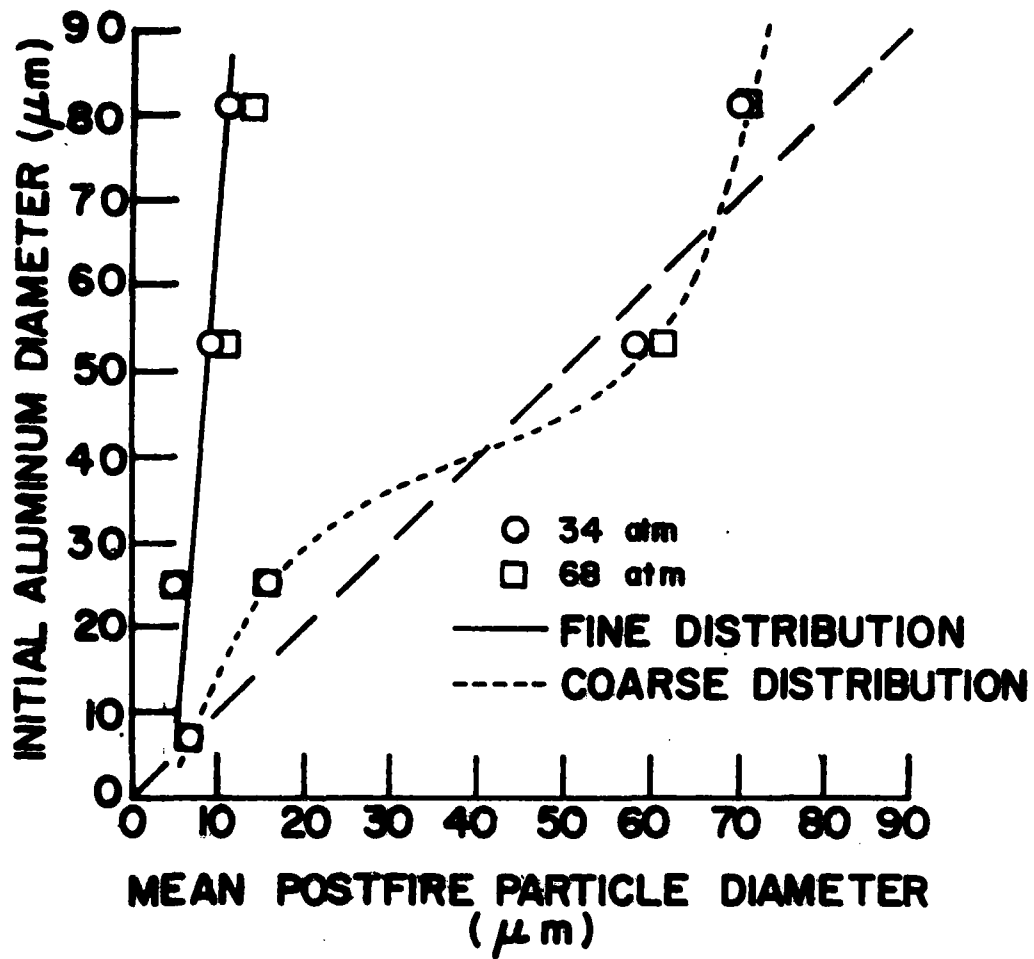


FIGURE 49 Initial Aluminum Particle Diameter Versus Mean Postfire Particle Diameter

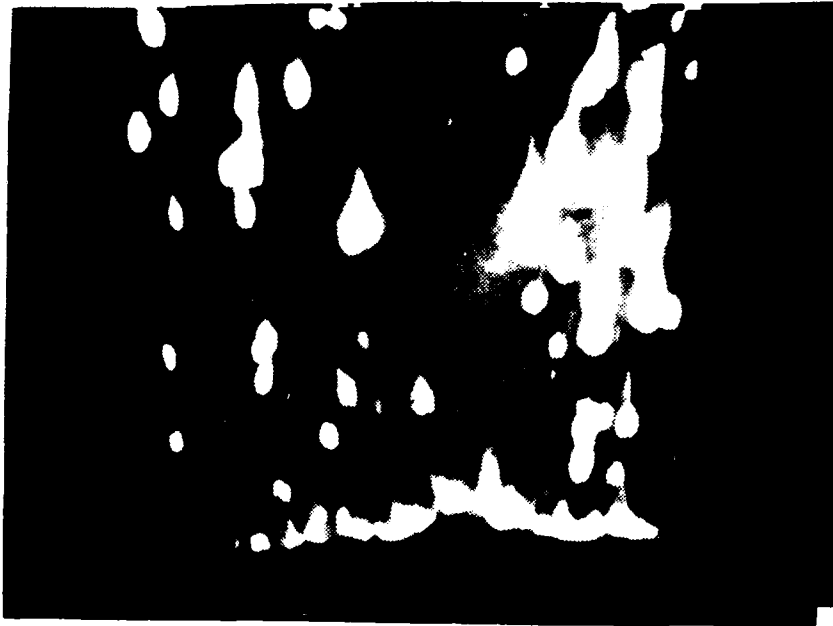


FIGURE 50 High Speed Motion Picture Frame  
(1415250580, WGS-5A, 34 atm. )



FIGURE 51 High Speed Motion Picture Frame  
(1100250580, WGS-5a, 68 atm. )

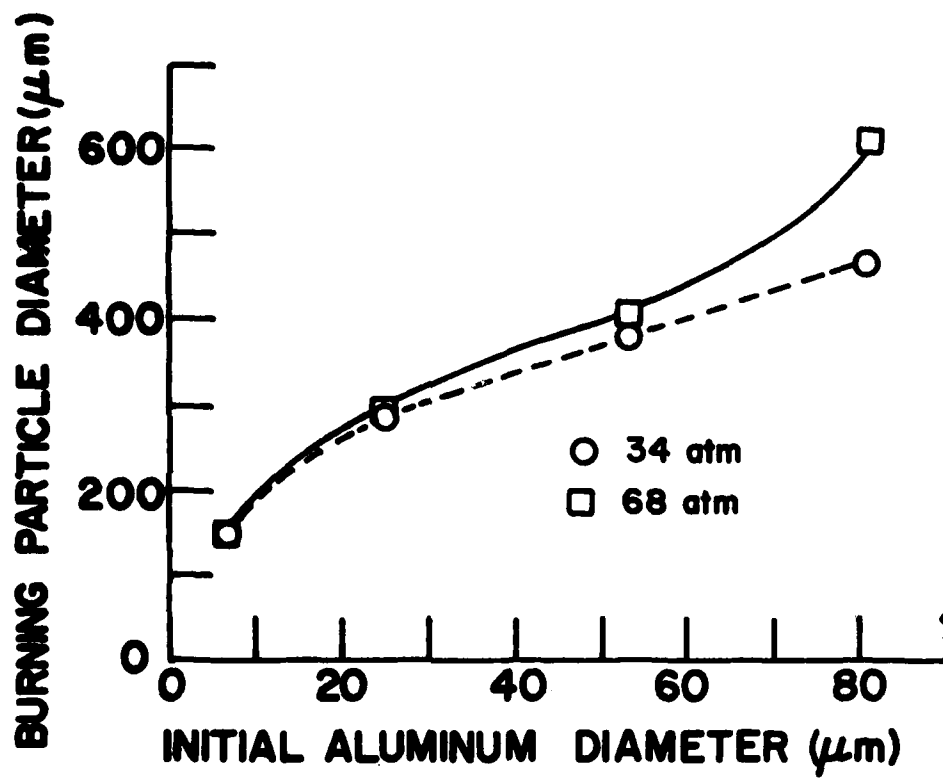


FIGURE 52 Burning Particle Diameter Versus Initial Aluminum Particle Diameter

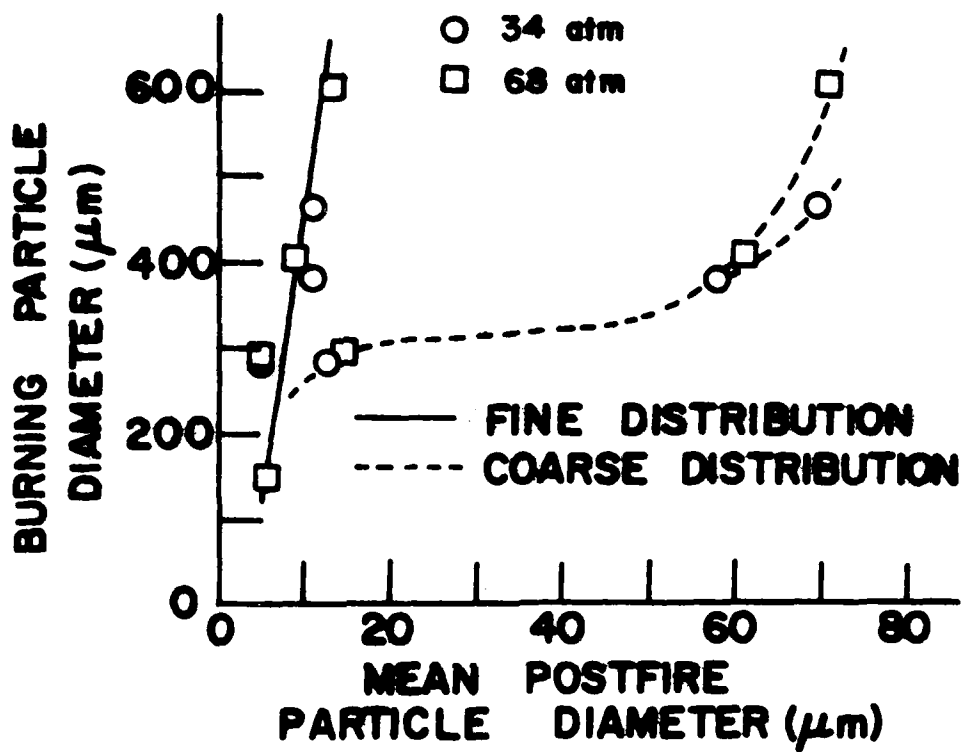


FIGURE 53 Burning Particle Diameter Versus Mean Postfire Particle Diameter

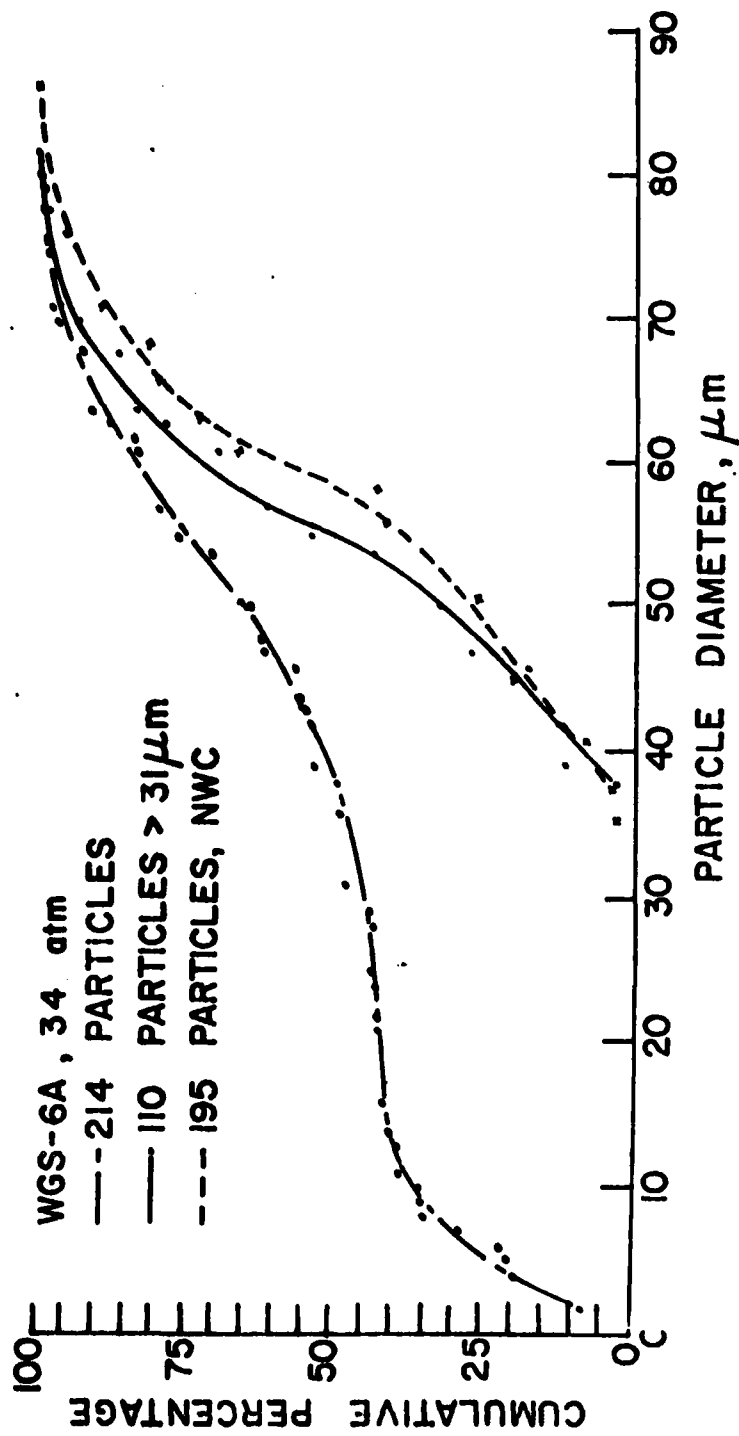


FIGURE 54 POSTFIRE PARTICLE SIZE DISTRIBUTION, WGS-6A Propellant

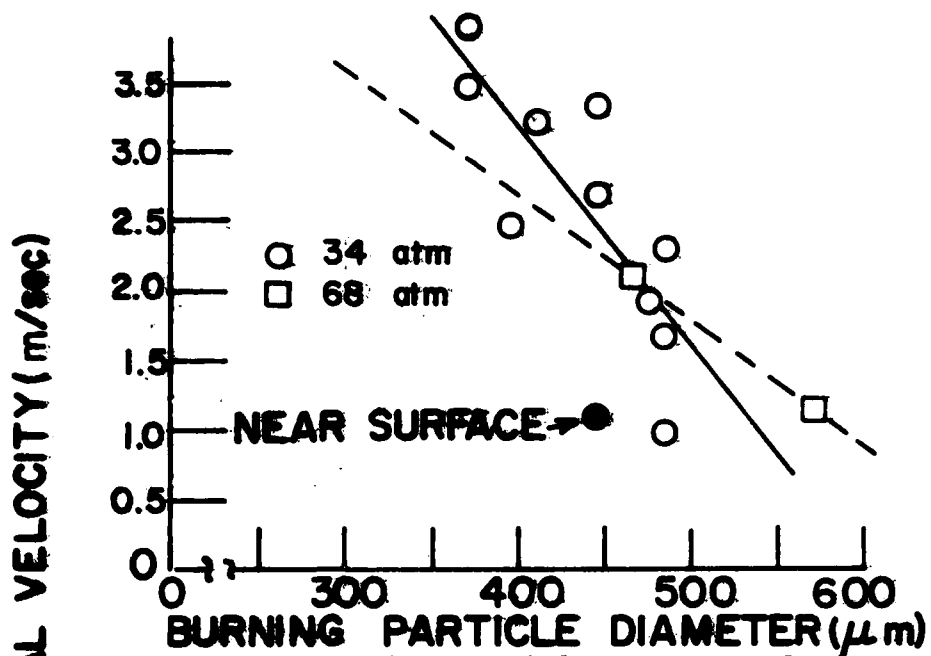


FIGURE 55 Burning Particle Average Velocity Versus Burning Particle Diameter for Propellant WGS-5A

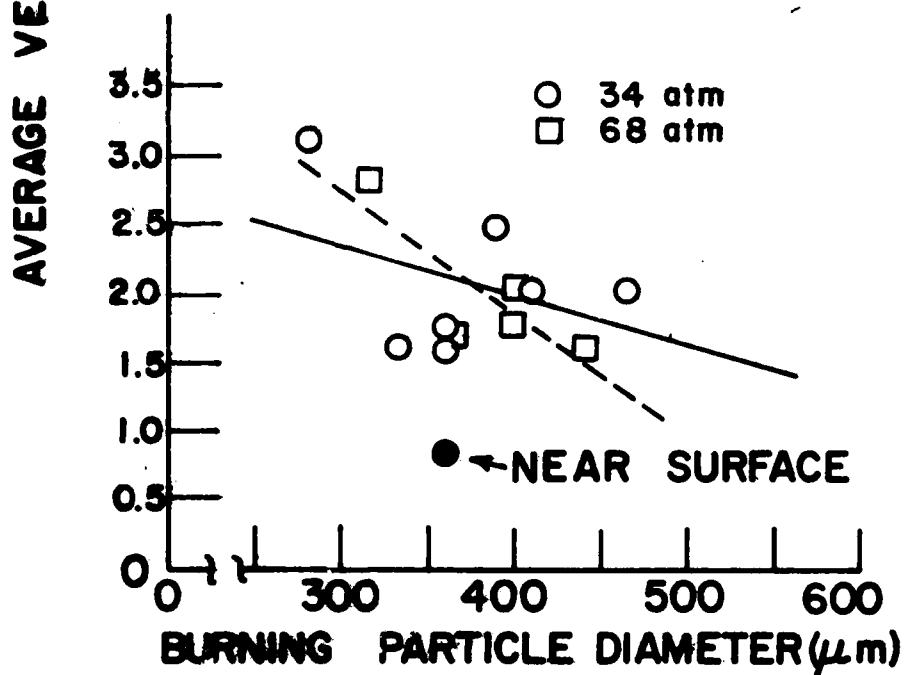


FIGURE 56 Burning Particle Average Velocity Versus Burning Particle Diameter for Propellant WGS-6A

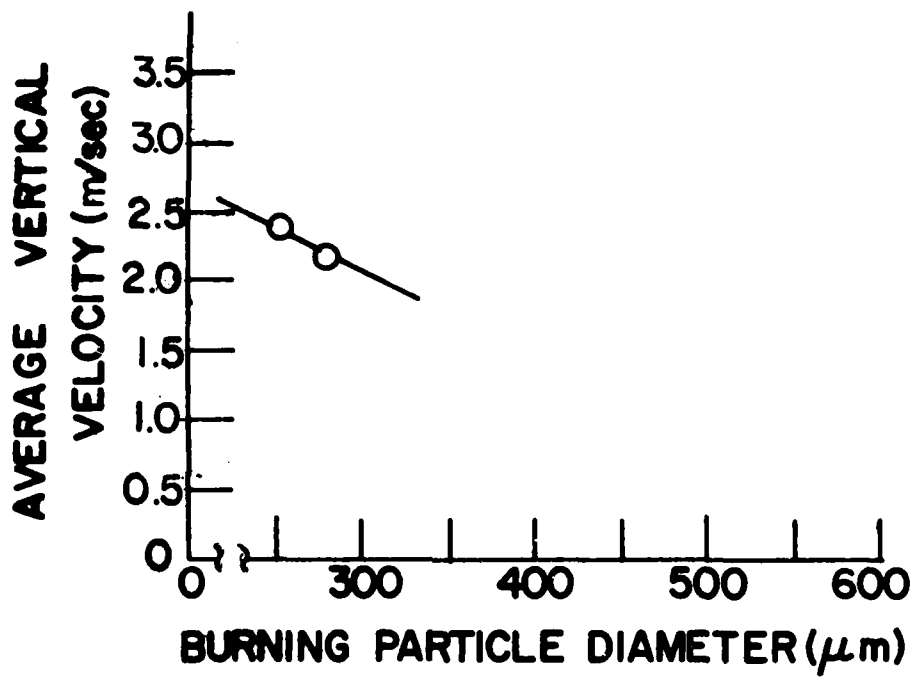


FIGURE 57 Burning Particle Average Velocity Versus Burning Particle Diameter for Propellant WGS 7-A

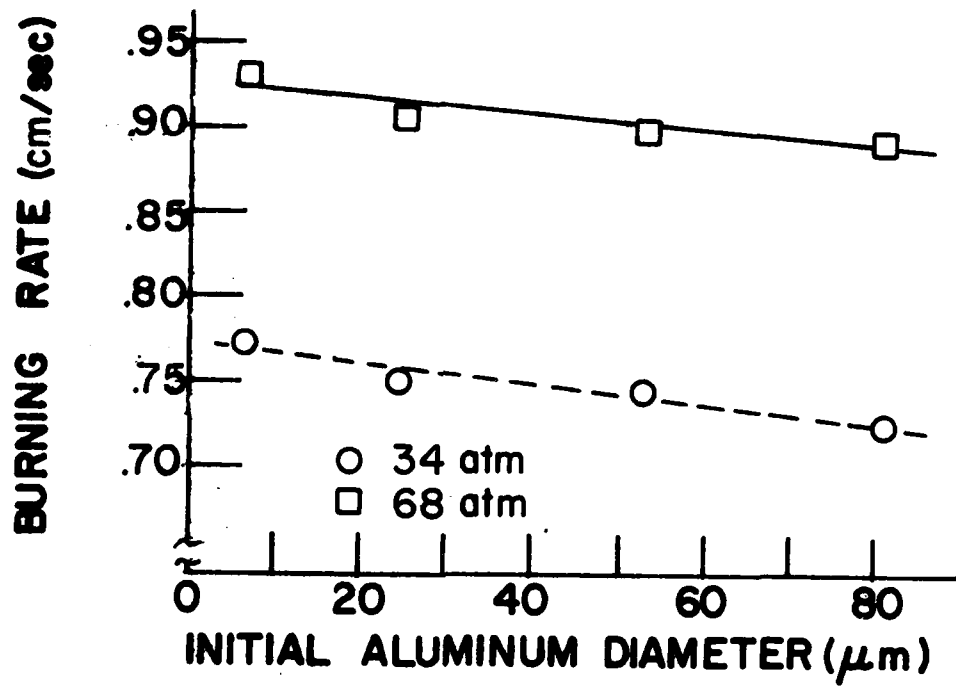


FIGURE 58 Burning Rate Versus Initial Aluminum Diameter

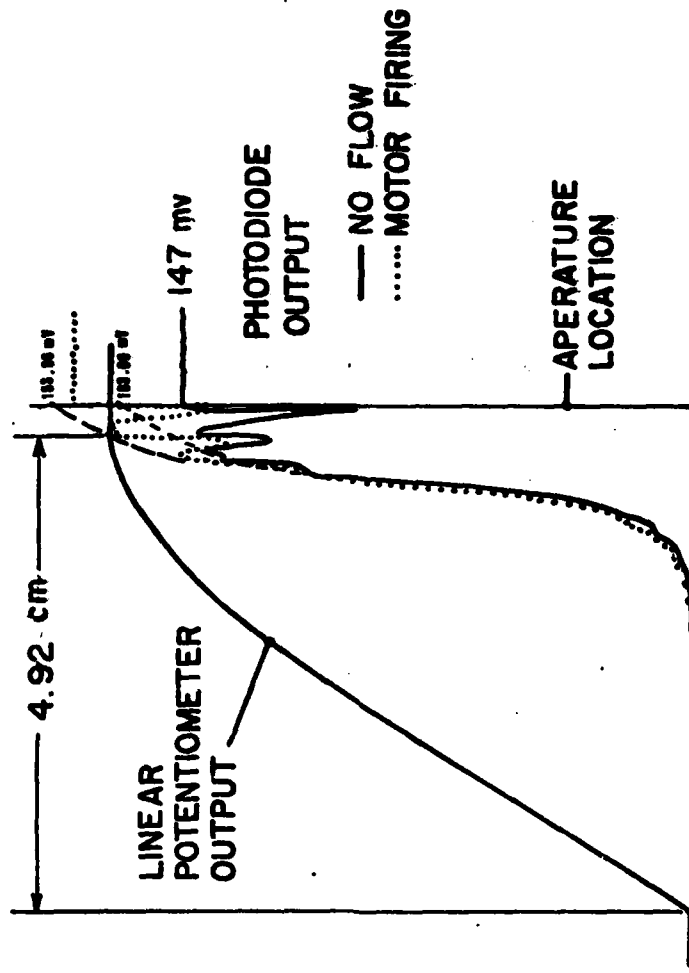


Fig. 59. Photodiode Output-Voltage Profiles versus Distance from Optical Centerline (actual runs)

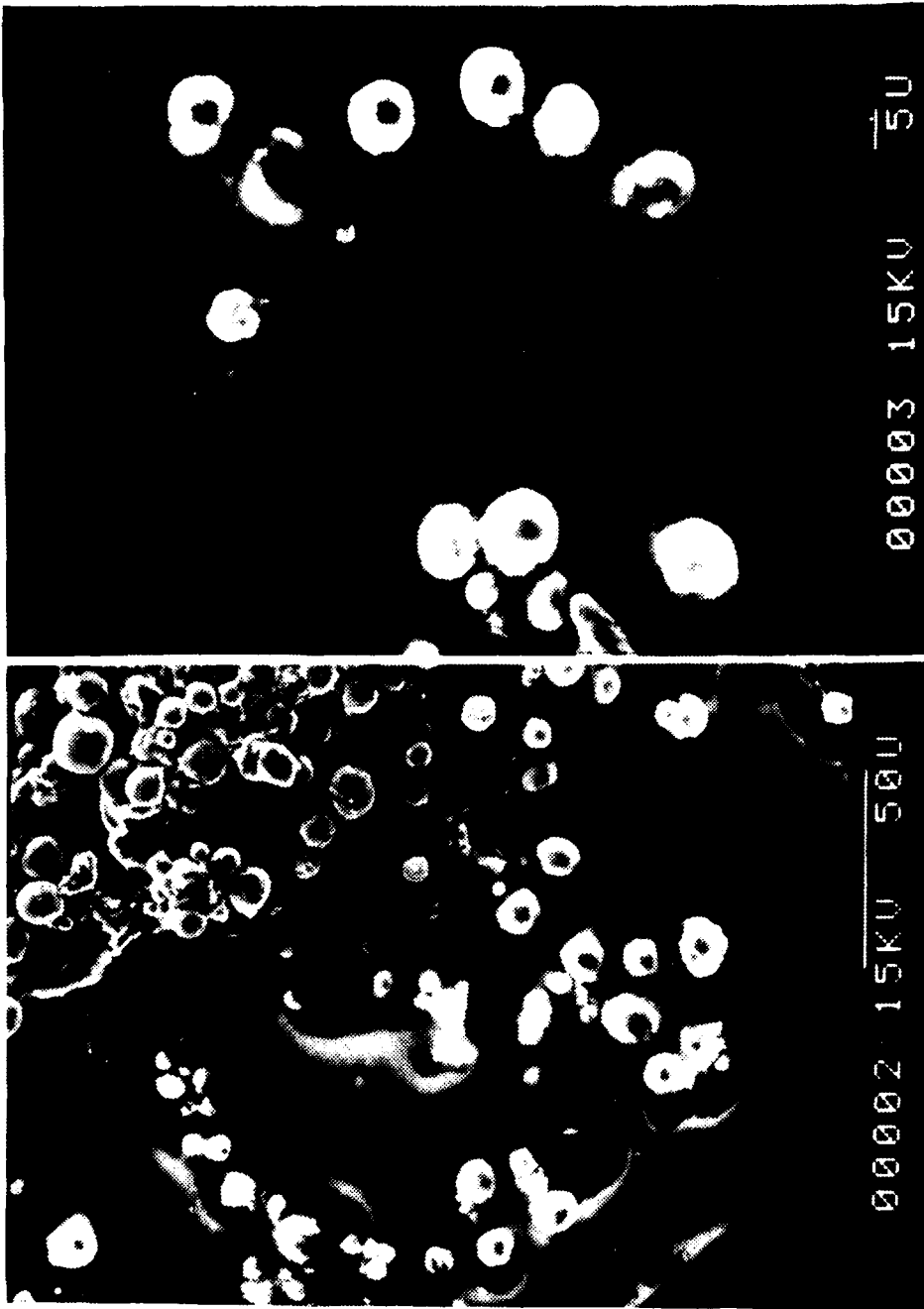


Fig. 60. SEM Photomicrographs of Rocket Exhaust Particles (clean)

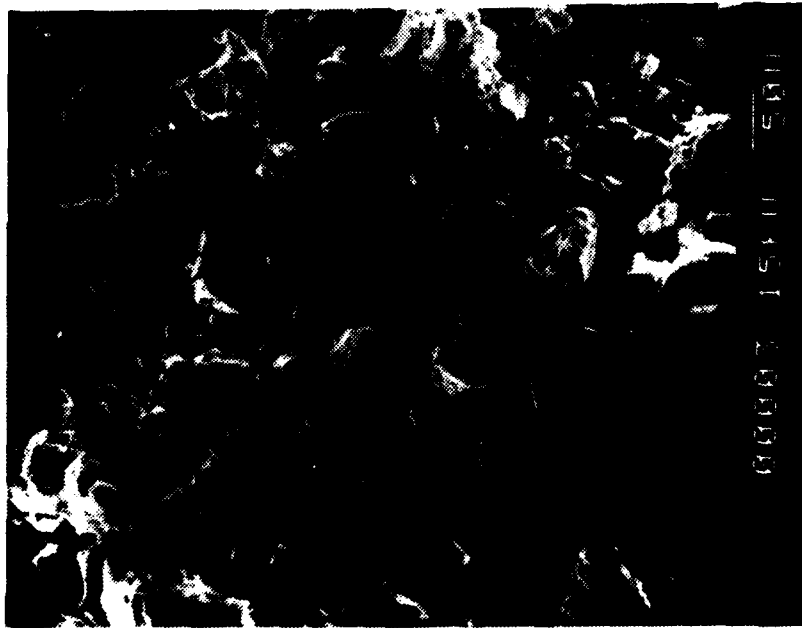


Fig. 61. SEM Photomicrographs of Rocket Exhaust Particles (as-collected)

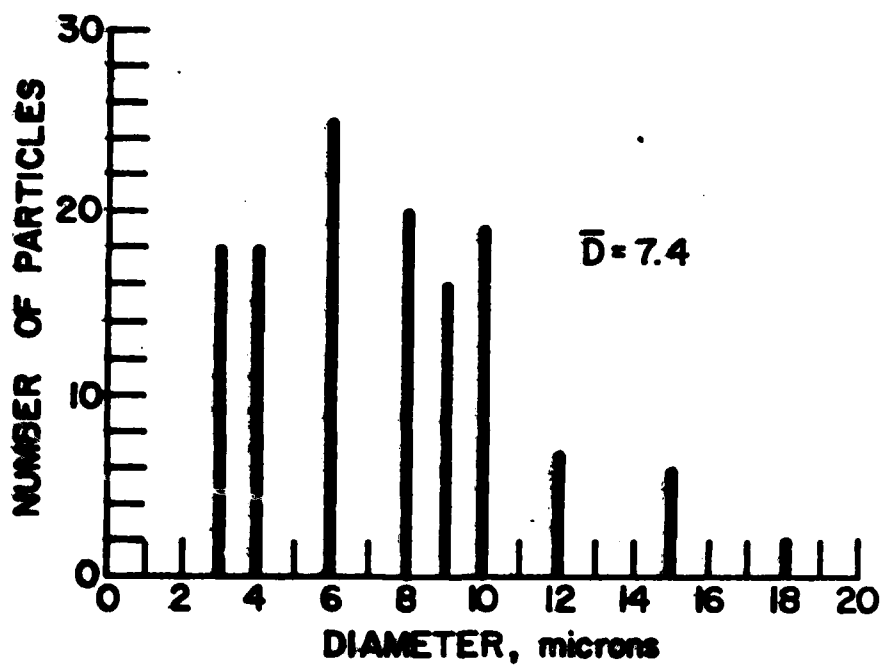


Fig. 62. Size Distribution of Clean Exhaust Particles from Propellant NWC-1, Burned at 13 atm.

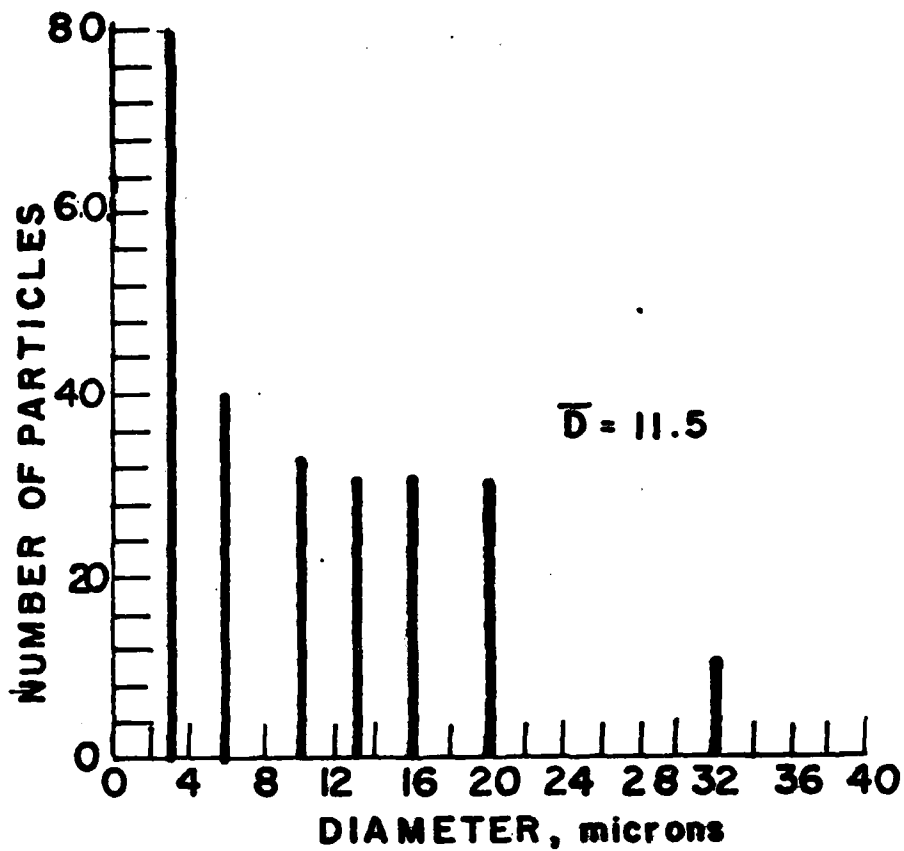


Fig. 63. Size Distribution of (As-Collected Exhaust Particles) from Propellant NWC-1, Burned at 13 atm.



Motion Picture; Scale 1102  $\mu\text{m}/\text{cm}$



Hologram, 50  $\mu\text{sec}$  pulse, 28 ND filter;  
Scale 568  $\mu\text{m}/\text{cm}$

Fig. 64. WGS-5A Propellant Burned at 34 atm.



(a) Hologram without  
mylar disc;  
scale 568  $\mu\text{m}/\text{cm}$



50  $\mu\text{sec}$  pulse , .28 ND filter

(b) Hologram with  
mylar disc;  
scale 427  $\mu\text{m}/\text{cm}$



(c) motion picture; scale 1102  $\mu\text{m}/\text{cm}$

Fig. 65. WGS-5A Propellant Burned at 68 atm.

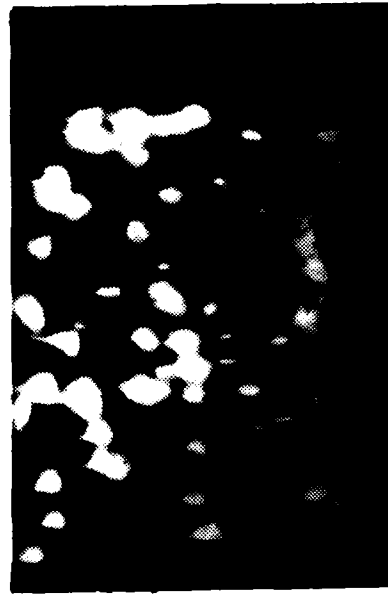


(b) Hologram  
with mylar disc;  
scale 477  $\mu\text{m}/\text{cm}$



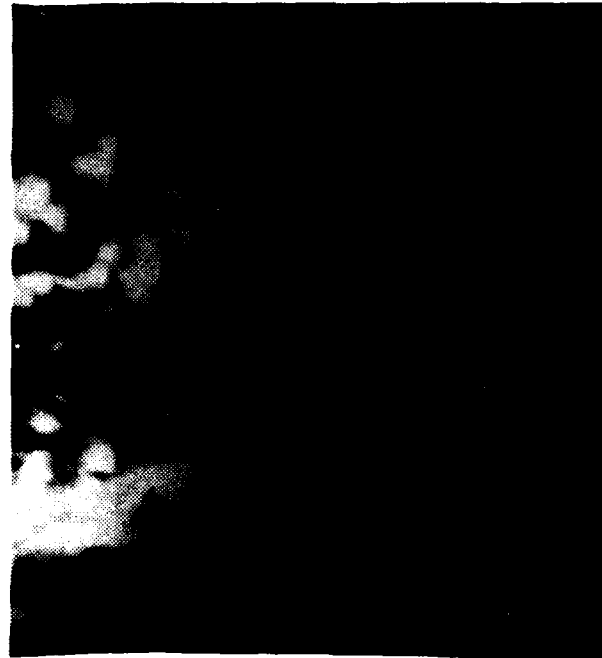
(a) Hologram  
without mylar disc;  
scale 568  $\mu\text{m}/\text{cm}$

50  $\mu\text{sec}$  pulse , .28 ND filter



(c) motion picture; scale 1102  $\mu\text{m}/\text{cm}$

Fig. 66. WGS-6A Propellant Burned at 34 atm.



(a) Motion Picture, scale 1102  $\mu\text{m}/\text{cm}$ .



(b) Hologram, 50  $\mu\text{sec}$  pulse, .35 ND filter;  
scale 568  $\mu\text{m}/\text{cm}$ .

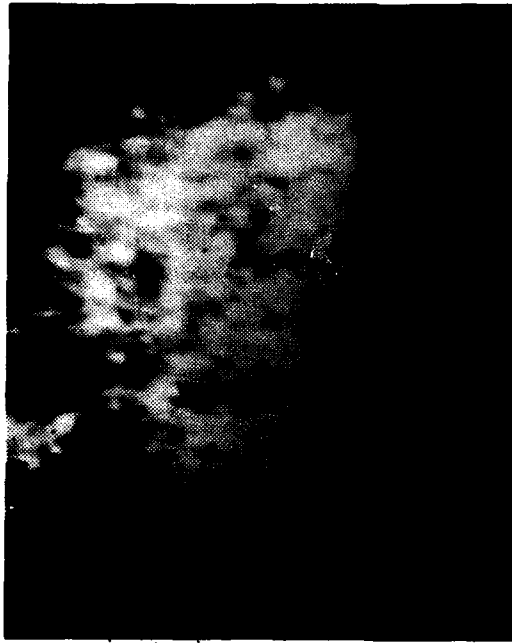


(a) Motion Picture; Scale 1102  $\mu\text{m}/\text{cm}$ .

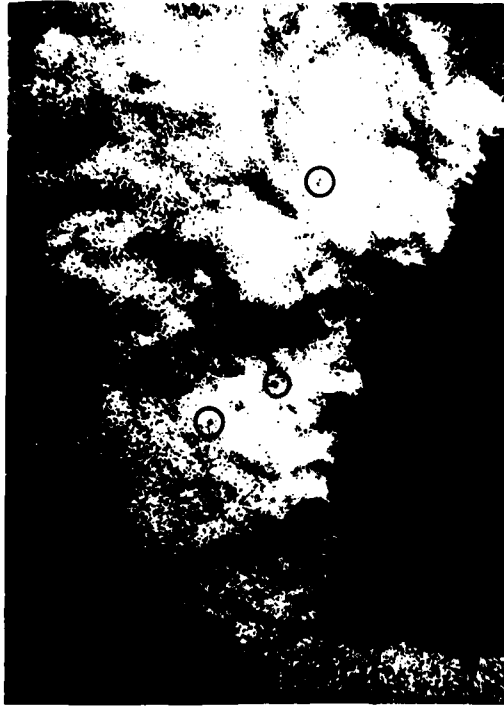


(b) Hologram, 50  $\mu\text{sec}$  pulse, .28 ND filter;  
Scale 568  $\mu\text{m}/\text{cm}$ .

Fig. 68. WGS-7A Propellant Burned at 34 atm.

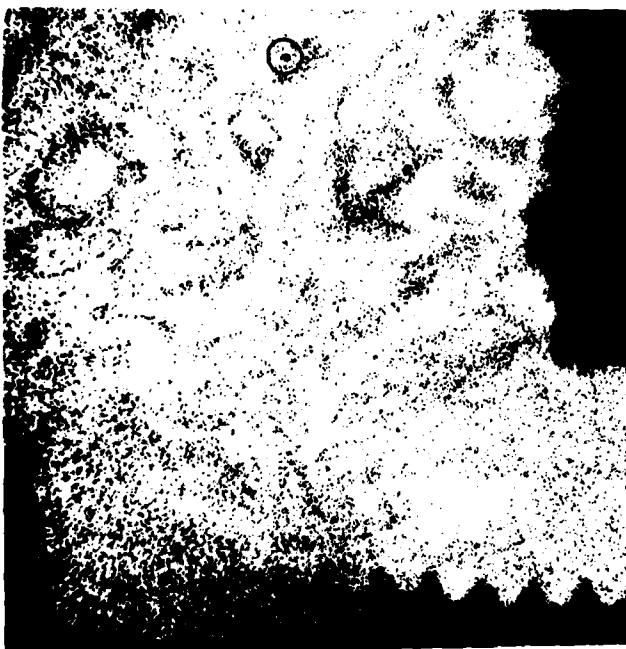


(a) Motion Picture; Scale 1102  $\mu\text{m}/\text{cm}$ .



(b) Hologram; 50  $\mu\text{sec}$  pulse.  
.35 ND filter; Scale 568  $\mu\text{m}/\text{cm}$ .

Fig. 69 WGS-7A Propellant Burned at 68 atm.

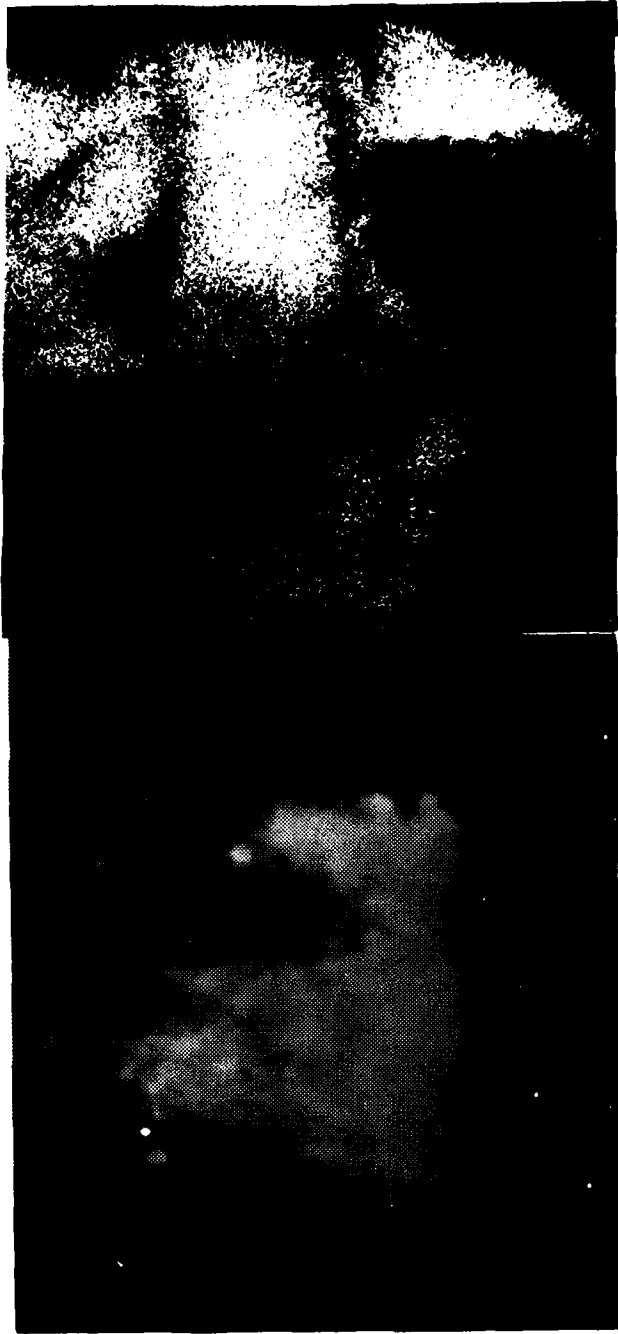


(a) 34 atm ; .28 ND filter;  
Scale 427  $\mu\text{m}/\text{cm}$ .



(b) 68 atm ; .35 ND filter;  
Scale 568  $\mu\text{m}/\text{cm}$ .

Fig. 70 N-7 Propellant Holograms  
50  $\mu\text{sec}$  Pulse



(a) Motion Picture; Scale 1102  $\mu\text{m}/\text{cm}$ . (b) Hologram; 50  $\mu\text{sec}$  pulse, .35 ND filter; Scale 427  $\mu\text{m}/\text{cm}$ .

Fig. 71. WGS-7 Propellant Burned at 68 atm.

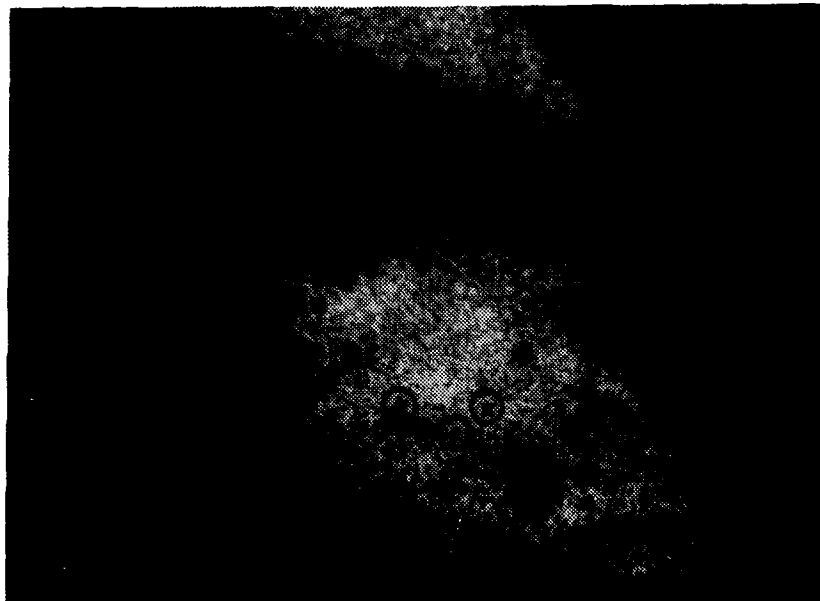


Figure 72. Photograph of Reconstructed Hologram of WGS-6A  
Propellant in 2-D Slab Motor

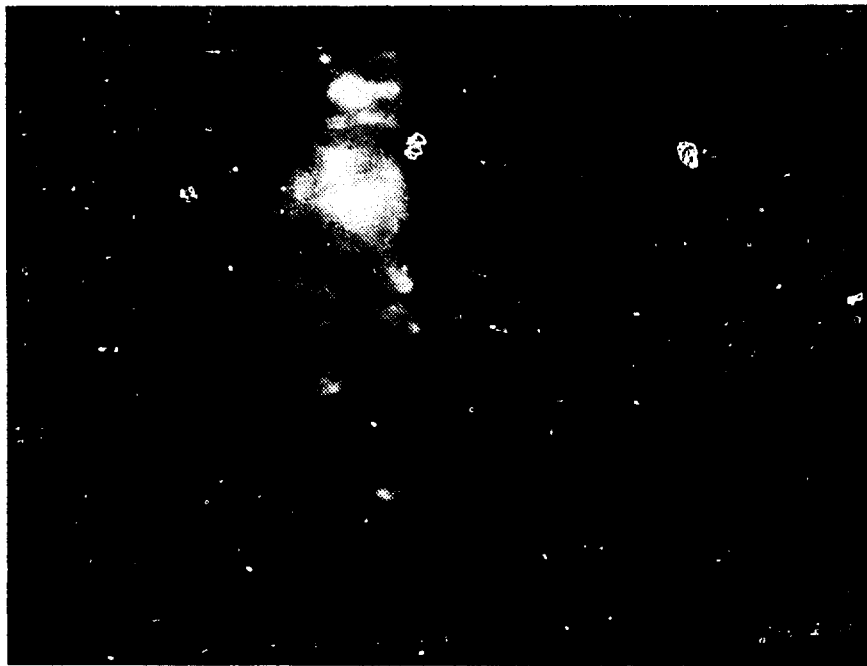


Figure 73. Motion Picture Frame of WGS-7A  
Propellant in 2-D Slab Motor